Illuminating Photocatalytic and Charge Transfer Mechanisms in Plasmonic Nanoparticle Systems

by

Calvin James Boerigter

A dissertation submitted in partial fulfillment
of the requirements for the degree of
Doctor of Philosophy
(Chemical Engineering)
in the University of Michigan
2016

Doctoral Committee:

Professor Suljo Linic, Chair
Professor Mark A Barteau
Associate Professor Jennifer Ogilvie
Professor Levi Theodore Thompson

2016

For JP, whose tragic passing led to my return home to the University of Michigan.
I know you're watching from above JP, we miss you today and every day.

Acknowledgements

There are so many people acknowledge and thank for playing a role, directly or indirectly, in completing this dissertation and graduate school as whole. First among them is my advisor, Prof. Suljo Linic. His ideas and guidance have been pivotal from the very beginning. The rest of my dissertation committee, Prof. Mark Barteau, Prof. Levi Thompson, and Prof. Jennifer Ogilvie, also deserves acknowledgement. No matter whether we've been in contact for years or only a few months, the thought provoking questions and comments on my work are much appreciated.

I'd also like to thank every member of the Linic Lab (double L) past and present for their scientific help and knowledge, and general friendship and fun office hijinks over the years. Particular thanks go out to my co-authors, Robert Campana, Matt Morabito, and Umar Aslam for integral help in putting together my publications. Anh Ta, Marimuthu Andiappan, and Tim Van Cleve, deserve special thanks for helping me get started in the lab and with my project. All other members, Adam Holewinski, Michelle Przybylek, Brittany Farrell, Thomas Yeh (always good for a joke), Paul Hernley, Valentina Igenegbai, Saman Moniri, Joe Quinn (hope you don't have to drink too many more venti iced coffee before it's your turn to graduate), and Steven Chavez, deserve more thanks than I have room or time to write about.

A special thanks also must go Dr. Susan Montgomery, who has been advising me on my academic and professional career since the first day I decided Chemical Engineering was interesting back in 2008. Thanks so much for going above and beyond anything an advisor with hundreds of ever-changing students could ever be asked to do, and doing it with a reassuring smile on your face.

Thanks to the staff of the ChE department, especially Susan, Kelly, Shelley, Barbara, Pam, Connie, for everything you've done and for being there with the free food at every opportunity.

Outside of the group, my first and biggest thanks has to go to Ryan Daly, whose been by my side, keeping me sane, every day for the majority of this PhD. Your almost total lack of interest in my work beyond the absolute basics was, surprisingly, unbelievably refreshing. Importantly, you knew never to ask "So when are you going to graduate?".

My family, nuclear and extended, is another group of people for whom there is not enough room or time to acknowledge adequately here. You all simultaneously reminded me how I'd make it because I'm so smart, and kept me grounded. Special mention goes to my mom Tish and dad Jim, for always being supportive in every way, and for spreading the word to rest of the family to stop asking me when I'm going to graduate.

And last but not least, a huge thanks has to go to all of my friends inside and outside the ChE department who've been there for me throughout grad school, from Minnesota and Michigan. You all know who you are, thank you. I can't wait to see what we all achieve. Go Blue!

Table of Contents

List of Tables

List of Figures

List of Equations

Abstract

Plasmonic metal nanoparticles can be tuned to very efficiently convert incoming visible (solar spectrum) photons into hot charge carriers within the nanoparticles. When a material, either a molecule or semiconductor, is chemically attached to the nanoparticle, the energetic carriers can transfer into the material. Once in the attached material, the energetic charge can provide current for a device, or induce a photochemical reaction. Classical models of photo-induced charge transfer in plasmonic metals suggest that the efficiency of this process is extremely low. The vast majority of the energetic charge carriers rapidly decay within the metal and are never transferred into the neighboring molecule or semiconductor. The studies in this dissertation demonstrate a system that effectively bypasses this inefficient conventional mechanism of charge transfer. They show that a system made up of silver nanocubes and an adsorbed dye molecule (methylene blue) experiences high rates of direct metal-to-molecule charge transfer, bypassing the decay and thermalization process normally taking place in the nanoparticle. In this direct charge transfer mechanism, the yield of extracted hot carriers from plasmonic nanoparticles can be significantly higher than in conventional systems. Analysis of the results within the framework of this direct mechanism points toward a method of engineering numerous systems for efficient charge generation and extraction from plasmonic nanoparticles, with many potential applications.

Chapter 1

Introduction

1.1 Summary

This chapter provides an introduction to the class of materials known as plasmonic metal nanoparticles and outlines the many ways in which they have potential as solar energy converters. The strong interaction of electromagnetic fields, especially visible light, with plasmonic nanomaterials offers opportunities in various technologies that take advantage of the photophysical processes amplified by this light-matter interaction. This chapter begins with a brief discussion the fundamentals of surface plasmon resonance in nanoparticles on noble metals. It then moves to a discussion of some of the recent studies showing plasmonic nanoparticles, as a result of the photophysical interaction with light, activate and enhance chemical transformations directly on their surfaces. Special attention is paid to the mechanistic aspects of these transformations and remaining questions about the physical processes driving them. Raman spectroscopy, and more specifically surface-enhanced Raman spectroscopy (SERS), which also takes advantage of the photophysical interactions of plasmonic particles with visible light, is introduced. After a brief

introduction to the fundamentals of SERS, its potential for studying the microscopic mechanisms of light-plasmonic particle-adsorbate that are still not well understood is discussed. The chapter concludes with an outline of the studies presented in the rest of this dissertation.

1.2 Fundamentals of localized surface plasmon resonance

Plasmonic metallic nanostructures are defined by their interaction with photons (*i.e.*, light) through what is known as localized surface plasmon resonance (LSPR). LSPR is the collective resonant oscillation of the free (valence) electrons near the surface of a nanostructure in response to an outside incident electromagnetic field. When a photon passes near a plasmonic nanostructure, its oscillating field can pull free electrons away from stationary nuclei, inducing a dipole within the particle. LSPR is established when the frequency of an incident oscillating electromagnetic field (e.g. from a photon or electron[1]) matches the natural restoring frequency of the oscillating surface electrons toward the positively charged nuclei.

LSPR is typically limited to metal particles and features which are much smaller than the wavelength of light. Within these particles when there is LSPR, the particle-light interaction can be described using a dipole approximation. In this picture, the electron oscillation as a result of the incident photons generates an oscillating dipole within the particle. This oscillating dipole generates a radiating electromagnetic field.[2] This field modifies the electric field surrounding the particle, especially near the surface (*i.e.*, the metal-dielectric interface). As shown in the data in Figure 1-1, at the resonance condition, enhancements in the intensity of the electric field ($|E|^2$) compared with that of the

incoming photon flux can approach 10^2 around the surface of a single isolated nanoparticle.[3] Additionally in the figure, it is shown that when two nanoparticles are brought to a separation on the order of ~ 1 nm, the fields confined within the small space between the particles can be enhanced even further, to almost 10^5 compared to the incident photon field.[4,5] These locations of extremely intense and confined electromagnetic field occurring in plasmonic systems are called hot spots. Hot spots exhibit multiple resonances, with a characteristic dipole resonance at a longer wavelength than the resonance of either of its isolated component nanoparticles.[6,7]

The existence and nature of plasmon resonance within a nanoparticle is not only dependent on the size of the nanoparticle but also its dielectric properties. The dielectric properties of the nanoparticle are determined by its composition, and the dielectric properties that lead to an interaction with visible light are found in nanoparticles of Ag, Au, and Cu[8,9]. This is due to the strong coupling in these particular noble metals of the plasmon transition (occurring in the s-band) and the interband transition (occurring between d-band and s-band). The conduction (s-band) electrons can move freely in these metal nanoparticles, giving them high polarizability and shifting plasmon resonances to the visible spectrum. For this reason the major focus in plasmonics is typically on Ag, Au, and Cu nanostructures, while other transition metals exhibit plasmon resonance only in the deeper UV ranges. By manipulating the composition (Figure 1-1a), shape (Figure 1-1b), and size (Figure 1-1c) of plasmonic nanoparticles, it is possible to design nanostructures that interact with the entire solar spectrum.[10,11]

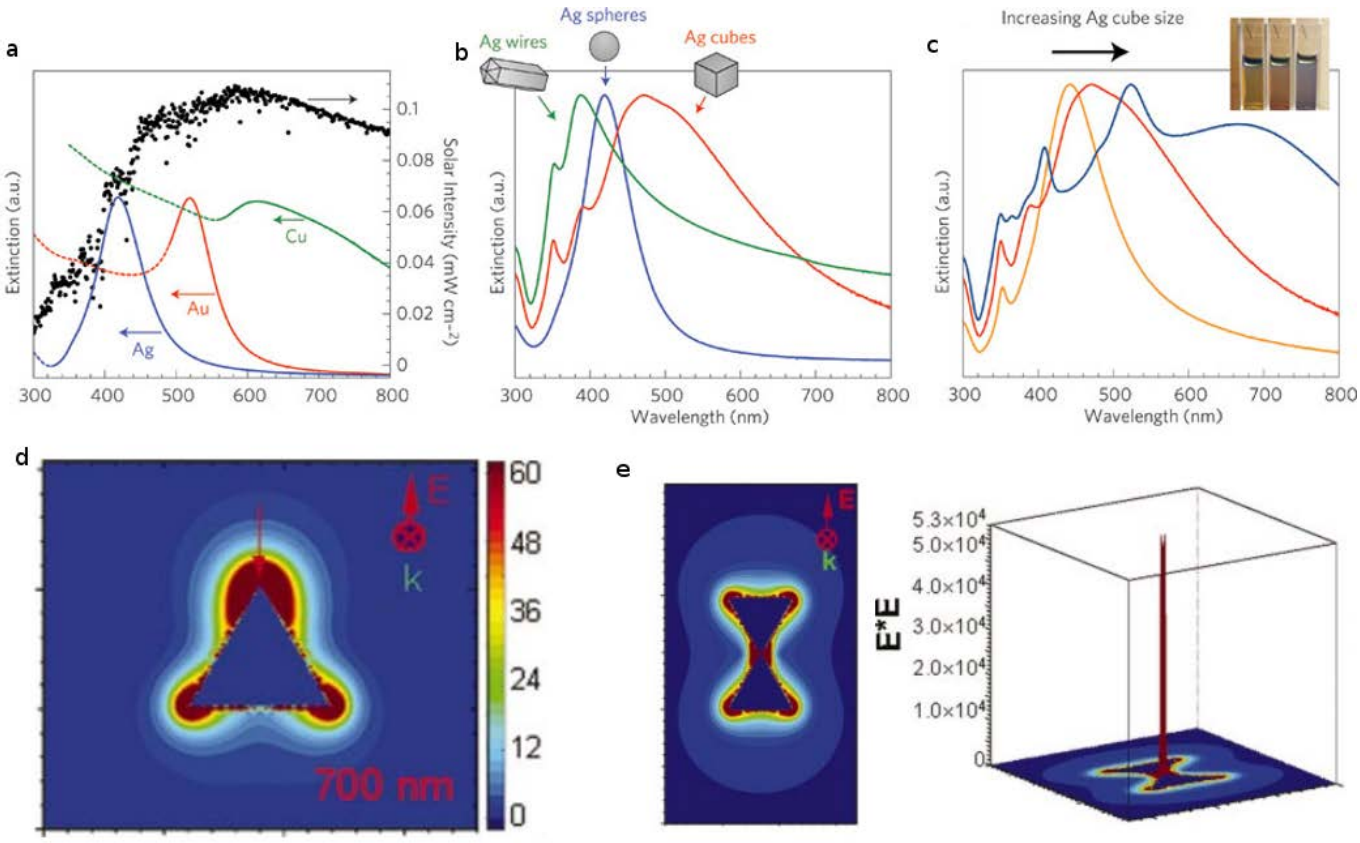

Figure 1-1: Characteristics of plasmonic metallic nanoparticles. (a) Extinction *spectra* of sub-100 nm silver, gold, and copper nanoparticles showing their respective plasmonic resonance peaks and plotted with the solar spectrum. (b,c) Extinction properties can be tuned by changing the shape and size of nanoparticles. (d) Simulated spatial distribution of the LSPR-induced electric field enhancement around a single isolated Ag nanoprism and (e) two Ag nanosprisms arranged point-to-point at a separation of 2nm, with a 3D contour showing greater than 4 orders of magnitude field enhancement occurring in the "hot spot" in between the particles. a, b, c from ref [37] and d, e from ref 4.

1.2.1 Mechanisms of plasmon decay

Of particular interest to the topics of this dissertation are the mechanisms by which LSPR decays, *i.e.*, how the energy, initially of the photon and transferred to the oscillating free electrons, is further dissipated into the system. Upon resonant excitation, plasmons relax within tens of femtoseconds (10^{-14} sec). Relaxation (decay) is known to take place

thorough one of two pathways: radiative photon re-emission (scattering) or non-radiative excitation of energetic charge-carriers (absorption). In the radiative case, the re-emitted photon is of the same energy/wavelength as the incident. In the non-radiative case, the absorption results in the formation of energetic electron-hole pairs near the surface of the nanoparticle, with their energy matching the resonant photon energy.[12]

In unreactive environments, without any molecular adsorbates on the surface of the nanoparticle interacting electronically, radiative photon emission is the dominant mode of plasmon decay for larger nanoparticles (in Ag, characteristic length > 50 nm).[13] For isolated small nanoparticles (in Ag, characteristic length < 30 nm) in similar environments, the dominant mode of plasmon relaxation is non-radiative, leading to the formation of energetic charge carriers.[14] Plasmon resonance within the previously defined hot spots confined between two plasmonic nanoparticles can decay differently still. In these areas, the capacitive coupling between the oscillating electron clouds of the two neighboring particles can allow for free charge carriers to move efficiently between the particles in a tunneling process.[15,16]

1.3 Photochemical transformations directly on plasmonic particles

Energetic charge carriers, formed on the surface of a plasmonic nanoparticle or within a hot spot through a non-radiative plasmon decay pathway can potentially induce photochemical transformations of surface adsorbates. This has recently provided a huge number of studies into plasmon-driven reactions as they present a promising avenue toward simple solar-to-chemical energy transfer.[17] In the simplest form of plasmon-driven photocatalysis, energetic charge-carriers formed within the nanoparticle collide with other

charge carriers and the phonon modes of the nanoparticle, causing a heating of the nanoparticle above the ambient temperature.[18] The higher temperatures now present can speed up reactions through a mechanism identical to what would take place through conventional heating of the nanoparticles, where the energy of nanoparticle phonon vibrations is transferred to phonon modes of adsorbates until a reaction barrier is overcome. This conventional thermal mechanism is depicted in Figure 1-2a.

1.3.1 Charge carrier driven reaction on plasmonic nanoparticles

Of more interest to the studies present in this dissertation are reactions driven by plasmonic enhancement that proceed via less conventional, fully electron-driven mechanisms. The photothermal mechanism described above assumes that the energy of a photon is distributed into the phonon modes of a nanoparticle, which then drive chemical transformations. The excited electron distribution serves as a vehicle for the (phonon) heating of nanoparticles. An alternative mechanism assumes that energetic charge-carriers (electrons or holes), formed on the surface of nanoparticles, transiently occupy energetically accessible orbitals of the adsorbed molecule before their energy is dissipated.

In this mechanism, the energized charge-carriers (electrons or holes) transiently populate otherwise unpopulated electronic states (orbitals), centered on the adsorbate molecule, thereby forming transient ions (if viewed from the perspective of the adsorbate) or excited states (if viewed from the perspective of the entire adsorbate–nanoparticle system). In this process, the adsorbate (more specifically, the entire adsorbate-nanoparticle system) is moved to a different potential energy surface (PES) and forces are induced on atoms in the adsorbate, as depicted in Fig. 1-2b. These forces lead to the nuclear motion of

atoms in the adsorbate, which can result in the activation of chemical bonds and chemical transformations.[19]

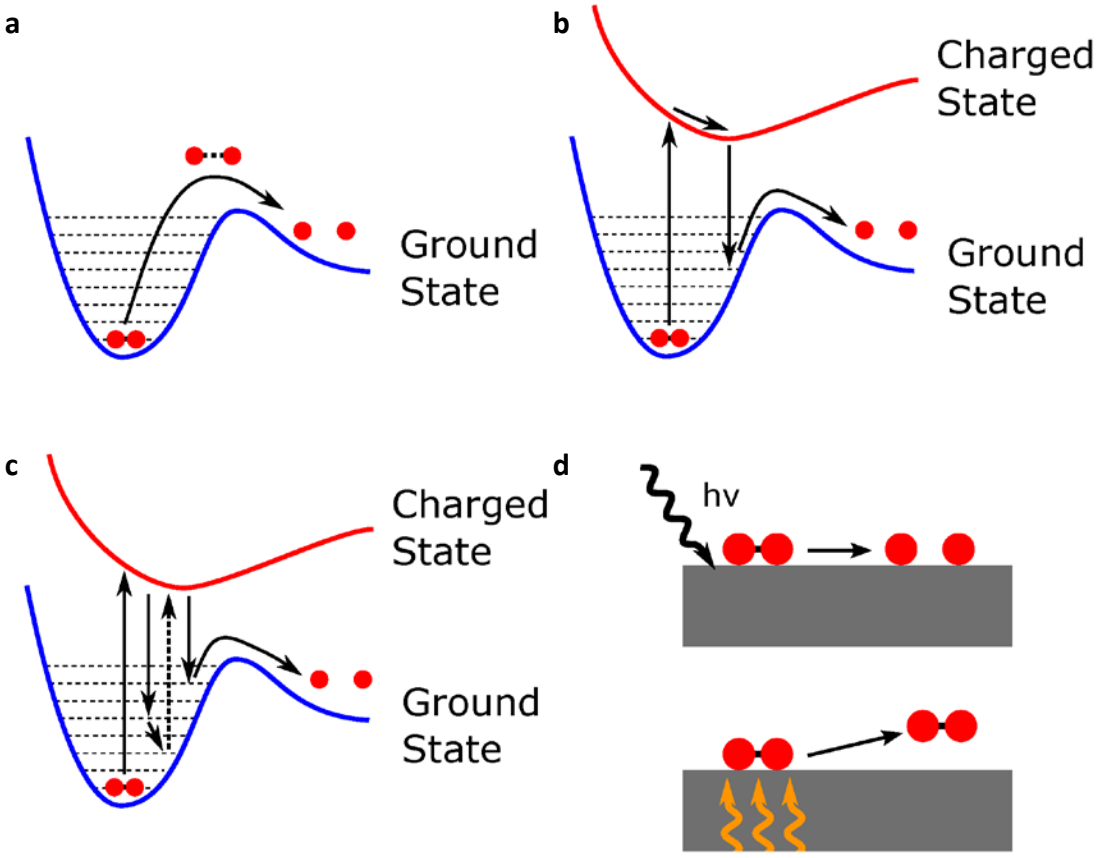

Figure 1-2: Mechanisms of phonon- and electron-driven reactions on metals. (a) Thermal activation for the dissociation of a diatomic molecule. The diatomic molecule remains on the ground-state PES for all points along the reaction coordinate. (b) Electron-driven dissociation of a diatomic molecule. Injection of an excited electron promotes the molecule to a new PES, thereby inducing nuclear motion. This charged state then decays, which drops the molecule back down to the ground state while populating a higher vibrational mode. (c) At high photon flux, subsequent electron injections can occur before the molecular vibration has fully dissipated, thus leading to additional vibrational excitation and a superlinear dependence of the rate of reaction on light intensity. (d) Electron-driven reactions (top), for example on plasmonic metal nanoparticles, can potentially target certain chemical reaction pathways that are otherwise unselective in purely thermal reactions (bottom). Figure adapted from ref [38].

At the heart of this mechanism is a coupling between excited electronic and vibrational states of the adsorbate-nanoparticle complex. Essentially, the energy of the charge carrier is converted into kinetic energy of the complex along the reaction coordinate (for example, vibrational energy of the activated chemical bond; Fig. 1b). This charge-carrier-mediated mechanism of bond activation has been studied in a number of experiments involving single-crystal surfaces of bulk metals illuminated with short pulses of high-intensity light (10^6-10^9 times higher than solar flux).[20] In the surface science community, this mechanism is known by its original name: desorption (reaction) induced by electronic transitions (DIET).[21,22]

There have been a number of studies published showing examples of charge-carrier-mediated photochemistry driven by LSPR at light intensities similar to solar. One of the first studies suggested this charge-carrier-mediated in enhancement of ethylene epoxidation reactions on Ag nanosphere and nanocube catalysts.[23] These reactions exhibited nearly instantaneous, reversible increases in the rate of ethylene epoxidation (while maintaining selectivity to the desired product) under normal reaction conditions upon illumination with broadband light at intensities of a few hundred milliwatts per square centimeter. These reactions were further found to exhibit the experimental signatures of reactions on metals driven by energetic charge-carriers, including a linear-to-superlinear transition in the rate dependence on photon flux and an unusually large kinetic isotope effect.[24] Similar studies were performed investigating LSPR-induced room temperature dissociation of H_2 on Au nanostructures with the same result of reversible

reaction enhancement and same conclusion of a charge-carrier-mediated enhancement mechanism.[25]

It was additionally demonstrated that LSPR-induced charge-carrier-mediated reactions could alter the selectivity to desired products within a reaction system. One example study accomplished this by taking advantage of generated charge carriers within a Cu nanoparticle catalyst to change the oxidation state of atoms on the surface. In this particular case, the light-induced reduction of copper oxide to copper metal changed the dominant chemical pathway from one leading to the complete combustion of the propylene, to one resulting instead in the desired partial oxidation product, propylene oxide.[26]

Although there is a conceptual understanding of the dynamics of these reaction mechanisms in terms of DIET model, there are still some critical unanswered questions about the movement of energetic charge carriers (or energy) after the decay of a plasmon from the particle to the adsorbate. There are two distinct possibilities through which this charge transfer can take place, and they will be referred to in this dissertation as the indirect and direct charge transfer mechanisms. The indirect charge transfer mechanism assumes that energetic charge-carriers first form on the surface of optically excited plasmonic nanoparticles under the influence of large electric fields, and subsequently transfer to adsorbate acceptor states. The direct charge transfer mechanism proposes that charge transfer to a surface adsorbate occurs without the energetic charge carrier first existing entirely within the nanoparticle; the charge carrier excites directly from near the Fermi level of the metal to the higher energy unoccupied orbital within the adsorbate.[27]

The indirect and direct mechanisms are discussed in much more detail in Chapters 4 and 5 of this dissertation.

1.4 Raman spectroscopy: Fundamentals, SERS, and studying charge transfer

One of the main experimental tools used within the studies of this dissertation to gain insights into plasmonic charge transfer mechanisms is Raman spectroscopy. Raman spectroscopy has been used for nearly a century to gain information about the vibrational dynamics of systems of molecules. Raman scattering is an inelastic photon scattering process resulting from electronic excitation and subsequent relaxation of a molecule in response to an incident photon. During the Raman scattering process, there is an exchange of energy between the photon and the molecule. In the photon, this is manifested as a change in its wavelength. In the molecule, the exchange of energy results in a change in energetic state of a vibrational mode. Vibrational modes are considered "low frequency" modes in a system because their energy is much less than the photon itself. As a result, the change in energy of a photon as result of a Raman scattering process is typically on the order of hundreds to a few thousand cm^{-1}, equivalent to tenths of electron volts and tens of nanometers in the photon wavelength.[28]

1.4.1 Anti-Stokes and Stokes Raman scattering

It is possible for the photon in a Raman scattering event, upon interacting with a molecule, to either lose or gain energy and for the molecule to subsequently gain or lose energy, respectively, due to conservation of energy. These two occurrences are referred to as Stokes (photon energy loss) and anti-Stokes (photon energy gain) Raman scattering. Figure 1-3 shows a depiction of the molecular energy landscape of these two opposite

events, illustrating how the molecule first gains the energy of the entire photon and passes through a virtual or electronic energy state before relaxing back to a different vibrational energy state than in began, with the change in wavelength of the exiting photon being equal to vibrational energy change of the molecule.

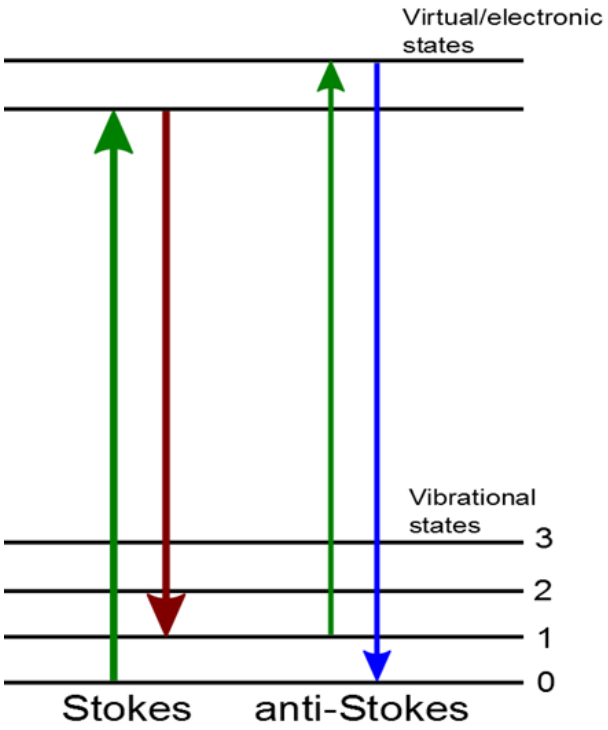

Figure 1-3: Schematic of Stokes and anti-Stokes Raman scattering. In Raman scattering, the molecule and photon exchange energy in the form of changes in wavelength for the photon and vibrational state for the molecule. In Stokes scattering, the molecule, the molecule gains a vibrational quantum of energy and so the photon loses the same amount of energy (it is red-shifted). Anti-Stokes scattering is the exact opposite process, with the photon gaining energy while the molecule loses it.

Because the potential vibrational energies of a particular mode are quantized, Raman scattering processes are quantized as well in the amount of energy a photon can gain or lose. This results in the Raman spectrum of a molecule, where peaks in the spectrum correspond to the energy of various bending, stretching, deformation, and other vibrational modes of a molecule. It should be noted that most vibrational transitions in

Raman scattering occur between vibrational energy states 0 and 1 of a particular mode, due to the fast decay of higher energy vibrations.[29] The many peaks of a Raman spectrum for a particular molecule correspond to the many independent vibrational modes of the molecule, roughly equivalent to the vibration of the many different individual bonds of the molecule.

Another result of quantized vibrational mode energies in molecules is seen when comparing the anti-Stokes and Stokes portions of the Raman spectrum for a molecule. The two halves of the spectrum exhibit peaks at equal but opposite Raman shifts (measured in cm^{-1}) representing opposite vibrational transitions of the same mode (*i.e.,* $0 \rightarrow 1$ vs $1 \rightarrow 0$). The strength of the anti-Stokes and Stokes signals (*i.e.,* the height of the peaks) is however not equal, as it is dependent on the population of molecules occupying the various energetic states of the vibrational mode.[30] It is this relation of the anti-Stokes and Stokes signals to the vibrational energy of a molecule that allows Raman spectroscopy to give information about charge transfer processes that are taking place. In depth discussion of the relationship between the vibrational energy population distribution within a system of molecules, how this relates to charge transfer, and how Raman spectroscopy is used to study this in particular, is given in Chapters 3, 4, and 5 of this dissertation.

1.4.2 Surface-enhanced Raman spectroscopy (SERS)

One of the consistent issues with Raman spectroscopy that limits its use as a characterization tool is the extremely low probability of photon interaction with a molecule resulting in Raman scattering. Cross-sections for Raman scattering processes of isolated free molecules are typically on the order of $\sim 10^{-24}$, precluding Raman spectroscopy from use without high molecular concentrations or extremely powerful light

sources.[31] Surface-enhanced Raman spectroscopy takes advantage of LSPR, specifically the phenomenon of high electric fields (discussed in Section 1.2) present at the surface of plasmonic nanoparticles in response to light, to increase Raman cross sections by up to ten orders of magnitude, making the detection of low concentrations of surface-bound molecules possible even with relatively low power Raman lasers.[32]

There are two established potential mechanisms by which LSPR can enhance Raman scattering. One mechanism involves the LSPR-induced enhancement of the local electric field intensity at the adsorbate (electromagnetic mechanism) leading to the enhancement of the Raman signal. The electromagnetic enhancement factor (Σ) of the Raman signal depends on electromagnetic field enhancement at the location occupied by a probe molecule. It can be closely approximated by:

$$\Sigma = (|\boldsymbol{E}(\nu_i)|^2 * |\boldsymbol{E}(\nu_i \pm \nu_m)|^2) \qquad (1\text{-}1)$$

where $\mathbf{E}(\nu)$ is the local electromagnetic field enhancement at a photon frequency ν, ν_i and $(\nu_i+\nu_m)$ are the frequencies of the incident (*i.e.,* laser) photon and scattered (*i.e.,* Raman shifted) photon respectively.[33,34] Equation 1-1 shows that the extent of electromagnetic enhancement in SERS is dependent on both the frequencies of the incident and scattered photon, *i.e.,* the signal from scattered photons of different wavelengths corresponding to different Raman shifts may be enhanced to different extents.[35] This is a very important property of SERS to note and the effect of it on the key findings in this dissertation is discussed in Chapter 3.

The other mechanism of enhancement in SERS involves the LSPR-induced charge-excitation (or charge-exchange) mechanism.[34] Charge-excitation SERS occurs as a result of the LSPR-mediated charge excitation from filled to unfilled electronic states of

the nanoparticle-adsorbate complex (one or both of these electronic states are localized on the adsorbate). The propensity to undergo charge excitation is, among other things, determined by the local electronic structure of the adsorbate-metal complex.[36]

The similarities between the charge excitation mechanism of Raman enhancement and charge transfer as a result of plasmon relaxation that is key in the DIET mechanism should be noted, as the processes are very similar. It is this very similarity that makes SERS an ideal characterization tool from studying the mechanisms of charge transfer in plasmonic nanoparticle-adsorbate systems. The studies, analysis, and conclusions presented in the remainder of this dissertation focus on what can be learned about these mechanisms from SERS experiments on carefully designed plasmonic nanoparticle-adsorbate systems and how such charge transfer can be controlled and tuned for use in efficient solar energy conversion.

1.5 Dissertation summary

The goals of this dissertation are to take advantage of the capabilities of SERS to probe the molecular vibrational energy landscape on plasmonic nanoparticles, and to use these capabilities to develop a fundamental, microscopic understanding of charge transfer processes occurring in plasmonic nanoparticle-adsorbate systems. This more thorough understanding of the mechanisms involved in these systems will serve as a guide to the design of more useful and efficient plasmonic systems and devices with potential uses in photocatalysis, photoelectrochemical processes, and photovoltaics. This dissertation shows that SERS can distinguish between systems in which there is resonant charge transfer caused by plasmon relaxation and those systems and conditions where it is not

occurring. In addition it points toward the existence of a direct charge transfer mechanism in specially designed systems. This direct mechanism bypasses many conventional plasmon relaxation processes that usually result in inefficient energy dissipation within plasmonic nanoparticles. Instead, it allows for the conversion of incident photon energy directly to molecular vibrational energy, which indicates charge transfer into the adsorbate, and can be utilized to drive photocatalytic chemical transformations on plasmonic surfaces or serve as the basis for a more complex solar-to-electrical energy conversion system.

In Chapter 2, the experimental methods and theoretical calculations used in the studies of this dissertation are laid out. The procedures for correct quantitative analysis of the experimental data are also described in detail. Specific attention is given to the preparation of samples for and performing of Raman spectroscopy studies that form the backbone for the findings presented herein. Additional characterization and computational methods, including spectroscopy, microscopy, and optical simulations, that supplement the Raman results and analysis are also described.

In Chapter 3, the most important and complicated step in properly analyzing and comparing anti-Stokes and Stokes Raman data is described in detail. It begins with a thorough explanation of the physical and instrumental causes of deviations of the anti-Stokes to Stokes peak ratio from the Boltzmann distribution. Methods for correcting raw experimental Raman data in any system for both major causes are then given. Finally, data is presented and the experimental anti-Stokes correction factor calculated specifically for the Ag nanocube systems used in later experiments in this dissertation.

Chapter 4 presents the first evidence that the Ag-methylene blue (MB) system exhibits the signatures of charge transfer. A thorough experimental and computational study of the optical properties of the plasmonic Ag-MB system is performed to confirm the abnormal anti-Stokes results obtained are indeed due to charge transfer at a specific incident photon wavelength (785 nm). The wavelength specific results, where higher energy photons do not similarly induce charge transfer, indicate the mechanism of charge transfer in this plasmonic system under resonant conditions is direct. The further implications of the direct transfer mechanism and some potential methods to take advantage of it for selective photocatalysis are discussed.

In Chapter 5, the Ag-MB system is again used in Raman studies, this time to provide evidence that the direct mechanism shown in Chapter 4 leads to an efficient transfer of energy from incident photon to adsorbate (*i.e.*, out of the plasmonic particle). The key result in this chapter is the simultaneous measurement of nanoparticle electronic and adsorbate vibrational temperatures using the same anti-Stokes and Raman spectrum under direct charge transfer conditions. The highly elevated adsorbate temperatures, evidenced by high anti-Stokes peak signals, in comparison to the nanoparticle temperatures, measured using the anti-Stokes background decay, indicate that plasmon decay leading to direct charge transfer bypasses many of the inefficient energy dissipation pathways within a plasmonic nanoparticle. The potential to design plasmonic systems to take advantage of direct charge transfer for efficient solar-to-chemical and solar-to-electrical energy conversion is explained.

Chapter 6 concludes this dissertation. The major conclusions regarding SERS measurements and charge transfer processes are highlighted in the context of how they

may be used in the broader field of plasmonics and photocatalysis. The application of the key discoveries of this dissertation in more industrially useful systems is also discussed.

1.6 References

(1) Scholl, J. A.; Koh, A. L.; Dionne, J. A. Quantum Plasmon Resonances of Individual Metallic Nanoparticles. *Nature* **2012**, *483*, 421–427.

(2) Bohren, C. F.; Huffman, D. R. *Absorption and Scattering of Light by Small Particles*; John Wiley & Sons, Ltd., 1983.

(3) Kelly, K. L.; Coronado, E.; Zhao, L. L.; Schatz, G. C. The Optical Properties of Metal Nanoparticles: The Influence of Size, Shape, and Dielectric Environment. *J. Phys. Chem. B* **2003**, *107*, 668–677.

(4) Hao, E.; Schatz, G. C. Electromagnetic Fields around Silver Nanoparticles and Dimers. *J. Chem. Phys.* **2004**, *120*, 357–366.

(5) El-sayed, M. A. Some Interesting Properties of Metals Confined in Time and Nanometer Space of Different Shapes. *Acc. Chem. Res.* **2001**, *34*, 257–264.

(6) Gao, B.; Arya, G.; Tao, A. R. Self-Orienting Nanocubes for the Assembly of Plasmonic Nanojunctions. *Nat. Nanotechnol.* **2012**, *7*, 433–437.

(7) Oubre, C.; Nordlander, P. Finite-Difference Time-Domain Studies of the Optical Properties of Nanoshell Dimers. *J. Phys. Chem. B* **2005**, *109*, 10042–10051.

(8) Burda, C.; Chen, X.; Narayanan, R.; El-Sayed, M. a. Chemistry and Properties of Nanocrystals of Different Shapes. *Chem. Rev.* **2005**, *105*, 1025–1102.

(9) Mallin, M. P.; Murphy, C. J. Solution-Phase Synthesis of Sub-10 Nm Au−Ag Alloy Nanoparticles. *Nano Lett.* **2002**, *2*, 1235–1237.

(10) Rycenga, M.; Cobley, C. M.; Zeng, J.; Li, W.; Moran, C. H.; Zhang, Q.; Qin, D.; Xia, Y. Controlling the Synthesis and Assembly of Silver Nanostructures for Plasmonic Applications. *Chem. Rev.* **2011**, *111*, 3669–3712.

(11) Xia, Y.; Xiong, Y.; Lim, B.; Skrabalak, S. E. Shape-Controlled Synthesis of Metal Nanocrystals: Simple Chemistry Meets Complex Physics? *Angew. Chem. Int. Ed.*

Engl. **2009**, *48*, 60–103.

(12) Link, S.; El-Sayed, M. A. Size and Temperature Dependence of the Plasmon Absorption of Colloidal Gold Nanoparticles. *J. Phys. Chem. B* **1999**, *103*, 4212–4217.

(13) Evanoff, D. D.; Chumanov, G. Size-Controlled Synthesis of Nanoparticles. 2. Measurement of Extinction, Scattering, and Absorption Cross Sections. *J. Phys. Chem. B* **2004**, *108*, 13957–13962.

(14) Evanoff, D. D.; Chumanov, G. Synthesis and Optical Properties of Silver Nanoparticles and Arrays. *Chemphyschem* **2005**, *6*, 1221–1231.

(15) Zuloaga, J.; Prodan, E.; Nordlander, P. Quantum Description of the Plasmon Resonances of a Nanoparticle Dimer. *Nano Lett.* **2009**, *9*, 887–891.

(16) Tan, S. F.; Wu, L.; Yang, J. K. W.; Bai, P.; Bosman, M.; Nijhuis, C. a. Quantum Plasmon Resonances Controlled by Molecular Tunnel Junctions. *Science.* **2014**, *343*, 1496–1499.

(17) Zhou, X.; Liu, G.; Yu, J.; Fan, W. Surface Plasmon Resonance-Mediated Photocatalysis by Noble Metal-Based Composites under Visible Light. *J. Mater. Chem.* **2012**, *22*, 21337–21354.

(18) Baffou, G.; Quidant, R. Thermo-Plasmonics: Using Metallic Nanostructures as Nano-Sources of Heat. *Laser Photon. Rev.* **2013**, *7*, 171–187.

(19) Gadzuk, J. W. Hot-Electron Femtochemistry at Surfaces: On the Role of Multiple Electron Processes in Desorption. *Chem. Phys.* **2000**, *251*, 87–97.

(20) Bartels, L.; Meyer, G.; Rieder, K.-H.; Velic, D.; Knoesel, E.; Hotzel, A.; Wolf, M.; Ertl, G. Dynamics of Electron-Induced Manipulation of Individual CO Molecules on Cu(111). *Phys. Rev. Lett.* **1998**, *80*, 2004–2007.

(21) Denzler, D.; Frischkorn, C.; Hess, C.; Wolf, M.; Ertl, G. Electronic Excitation and Dynamic Promotion of a Surface Reaction. *Phys. Rev. Lett.* **2003**, *91*, 226102.

(22) Prybyla, J. A.; Heinz, T. F.; Misewich, J. A.; Loy, M. M. T.; Glownia, J. H. Desorption Induced by Femtosecond Laser Pulses. *Phys. Rev. Lett.* **1990**, *64*, 1537–1540.

(23) Christopher, P.; Xin, H.; Linic, S. Visible-Light-Enhanced Catalytic Oxidation Reactions on Plasmonic Silver Nanostructures. *Nat. Chem.* **2011**, *3*, 467–472.

(24) Christopher, P.; Xin, H.; Marimuthu, A.; Linic, S. Singular Characteristics and Unique Chemical Bond Activation Mechanisms of Photocatalytic Reactions on Plasmonic Nanostructures. *Nat. Mater.* **2012**, *11*, 1044–1050.

(25) Mukherjee, S.; Libisch, F.; Large, N.; Neumann, O.; Brown, L. V; Cheng, J.; Lassiter, J. B.; Carter, E. A.; Nordlander, P.; Halas, N. J. Hot Electrons Do the Impossible: Plasmon-Induced Dissociation of H_2 on Au. *Nano Lett.* **2013**, *13*, 240–247.

(26) Marimuthu, A.; Zhang, J.; Linic, S. Tuning Selectivity in Propylene Epoxidation by Plasmon Mediated Photo-Switching of Cu Oxidation State. *Science* **2013**, *339*, 1590–1593.

(27) Petek, H.; Ogawa, S. Surface Femtochemistry: Observation and Quantum Control of Frustrated Desorption of Alkali Atoms from Noble Metals. *Annu. Rev. Phys. Chem.* **2002**, *53*, 507–531.

(28) Gardiner, D. J.; Graves, P. R. *Practical Raman Spectroscopy*; Springer-Verlag: Berlin, 1989.

(29) Kneipp, K.; Wang, Y.; Kneipp, H.; Itzkan, I.; Dasari, R.; Feld, M. Population Pumping of Excited Vibrational States by Spontaneous Surface-Enhanced Raman Scattering. *Phys. Rev. Lett.* **1996**, *76*, 2444–2447.

(30) Maher, R. C.; Galloway, C. M.; Le Ru, E. C.; Cohen, L. F.; Etchegoin, P. G. Vibrational Pumping in Surface Enhanced Raman Scattering (SERS). *Chem. Soc. Rev.* **2008**, *37*, 965–979.

(31) Jensen, L.; Schatz, G. C. Resonance Raman Scattering of Rhodamine 6G as Calculated Using Time-Dependent Density Functional Theory. *J. Phys. Chem. A* **2006**, *110*, 5973–5977.

(32) Moskovits, M. Surface-Enhanced Spectroscopy. *Rev. Mod. Phys.* **1985**, *57*, 783–826.

(33) García-Vidal, F.; Pendry, J. Collective Theory for Surface Enhanced Raman Scattering. *Phys. Rev. Lett.* **1996**, *77*, 1163–1166.

(34) Schatz, G. C.; Young, M. A.; Van Duyne, R. P. *Surface-Enhanced Raman Scattering*; Kneipp, K.; Moskovits, M.; Kneipp, H., Eds.; Topics in Applied Physics; Springer Berlin Heidelberg, 2006; Vol. 103.

(35) Itoh, T.; Yoshida, K.; Biju, V.; Kikkawa, Y.; Ishikawa, M.; Ozaki, Y. Second

Enhancement in Surface-Enhanced Resonance Raman Scattering Revealed by an Analysis of Anti-Stokes and Stokes Raman Spectra. *Phys. Rev. B* **2007**, *76*, 85405.

(36) Kambhampati, P.; Child, C. M.; Foster, M. C.; Campion, A. On the Chemical Mechanism of Surface Enhanced Raman Scattering: Experiment and Theory. *J. Chem. Phys.* **1998**, *108*, 5013.

(37) Linic, S.; Christopher, P.; Ingram, D. B. Plasmonic-Metal Nanostructures for Efficient Conversion of Solar to Chemical Energy. *Nat. Mater.* **2011**, *10*, 911–921.

(38) Linic, S.; Aslam, U.; Boerigter, C.; Morabito, M. Photochemical Transformations on Plasmonic Metal Nanoparticles. *Nat. Mater.* **2015**, *14*, 567–576.

Chapter 2

Experimental, Analytical, and Theoretical Methods

2.1 Summary

This chapter will discuss the details of the many experimental procedures used throughout this dissertation. Synthesis of the plasmonic particles used in the studies will be described in detail, as well as the methods used for characterization of the plasmonic nanoparticle systems. The fundamentals of Raman spectroscopy and surface-enhanced Raman scattering (SERS) are discussed, with specific emphasis on the underlying physics that govern and influence the results of some of the more important experiments in this dissertation. Furthermore, detailed descriptions of all Raman spectroscopy experiments, including sample preparation and experimental reactor design, spectrum gathering, and data interpretation are given. Additionally the theoretical tools, finite-difference time-domain (FDTD) and density functional theory (DFT), used to supplement the key experimental results are explained in detail.

2.2 Introduction

In studying the complicated physical mechanisms of charge transfer and energy conversion in plasmonic nanoparticle systems, this dissertation relied on a combined experimental and theoretical approach. The central experimental methods to the studies in this dissertation are the many varied Raman spectroscopy experiments conducted and the nuanced, quantitative analysis of all aspects of each Raman spectra individually and collectively. This chapter begins with the detailed methods by which plasmonic particles, and subsequently samples containing these particles for Raman spectroscopy studies, were synthesized and prepared. A very detailed description of the collection of Raman spectra from the samples, as well as the many ways in which the data were analyzed and useful quantitative values were derived from them, is then given. Specific focus is paid to the physical derivation of the values that were calculated from the Raman data. The supplementary characterization techniques and theoretical calculations and simulations, particularly those used for learning more about the synthesized plasmonic particles, were pivotal in supporting the Raman data and drawing important conclusions. The methods for those experimental techniques and physical simulations are also given in detail in this chapter.

2.3 Controlled synthesis of Ag nanoparticles

The key component of all experiments performed in this dissertation was a plasmonic Ag nanoparticle that could simultaneously serve as an anchor site for a dye molecule, a platform for SERS measurements, a catalyst, and a source of electrons from which to measure charge transfer. In order to ensure high quality and repeatable results it

was imperative to use a reproducible synthesis method for the plasmonic Ag particles used in various experiments.

When used as a catalyst, Ag nanoparticles are typically synthesized “on support”, that is, the nanoparticles are formed from the reduction of Ag^+ cations directly on a ceramic supporting material such as SiO_2 or Al_2O_3.[1] This method works well for large scale syntheses where the support is necessary to achieve proper three dimensional packing of the catalyst particles within a reactor setup. However, greater control over the synthesized shape and size of the Ag nanoparticles can be achieved utilizing solution-phase synthesis. Solution phase synthesis affords control over the four key steps that play a role in determining nanoparticle shape and size: reduction of the metal salt, nucleation of seeds, etching of seed particles and controlled nanocrystal growth.[2]

The precise control over the shape and size of Ag nanoparticles used in this dissertation is paramount to the quality and reproducibility of results presented herein. The optical properties of the nanoparticles are highly dependent on their shape and size. Figure 2-1 shows how the optical extinction spectrum, a combination of light absorption and scattering by the Ag nanoparticle in response to varying wavelengths of light, changes as the shape and/or size of the particles is altered. In this section, the multiple controlled Ag nanoparticle synthesis methods used will be described.

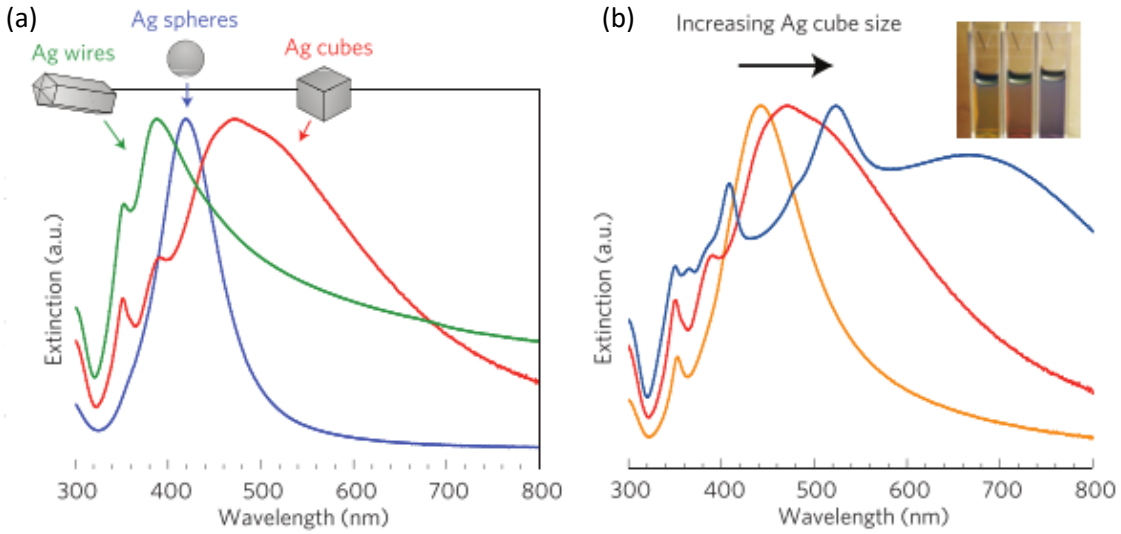

Figure 2-1: Extinction Spectra for Ag nanoparticles. (a) Normalized extinction spectra for a characteristic Ag wire, sphere, and cube. Wire-shaped particles are 90 ±12 nm diameter and >30 aspect ratio, cubic particles are 79 ±12 nm edge length and spherical particles are 38 ±12 nm diameter. (b) Normalized extinction spectra for Ag nanocubes as a function of size (56 ±8 nm, 79 ±13 nm and 129 ±7 nm edge lengths correspond to orange, red and blue spectra respectively). The inset shows a photograph of the three nanocube samples suspended in ethanol. Figure adapted from Linic *et al.* [22]

2.3.1 Ag nanocube synthesis

The majority of studies carried out for this dissertation used Ag nanocubes synthesized in the solution phase via the modified polyol process.[3] Nanocubes are characterized by being terminated on all sides with (100) facets of the Ag face-centered cubic (FCC) lattice. In comparison to similar-sized Ag nanospheres and nanowires, nanocubes have a higher characteristic extinction cross-section, *i.e.*, they interact more strongly with incoming light at resonant wavelengths. [4] This leads to stronger electromagnetic field enhancement at the surface of Ag nanocubes relative to other nanostructures. This increases the Ag nanocube's efficiency as a SERS platform, as the

enhancement in Raman signal is directly related to the electromagnetic field enhancement at the particle surface.[5]

The polyol synthesis is a relatively simple and highly useful method for synthesizing Ag nanostructures of many controlled shapes and sizes including spheres, rods, octahedra, and cubes.[6] In the process, ethylene glycol (EG) acts as both the solvent for all reagents and precursors as well as the reducing agent for the Ag^{+} ions. Figure 2-2 shows a depiction of the synthesis apparatus.

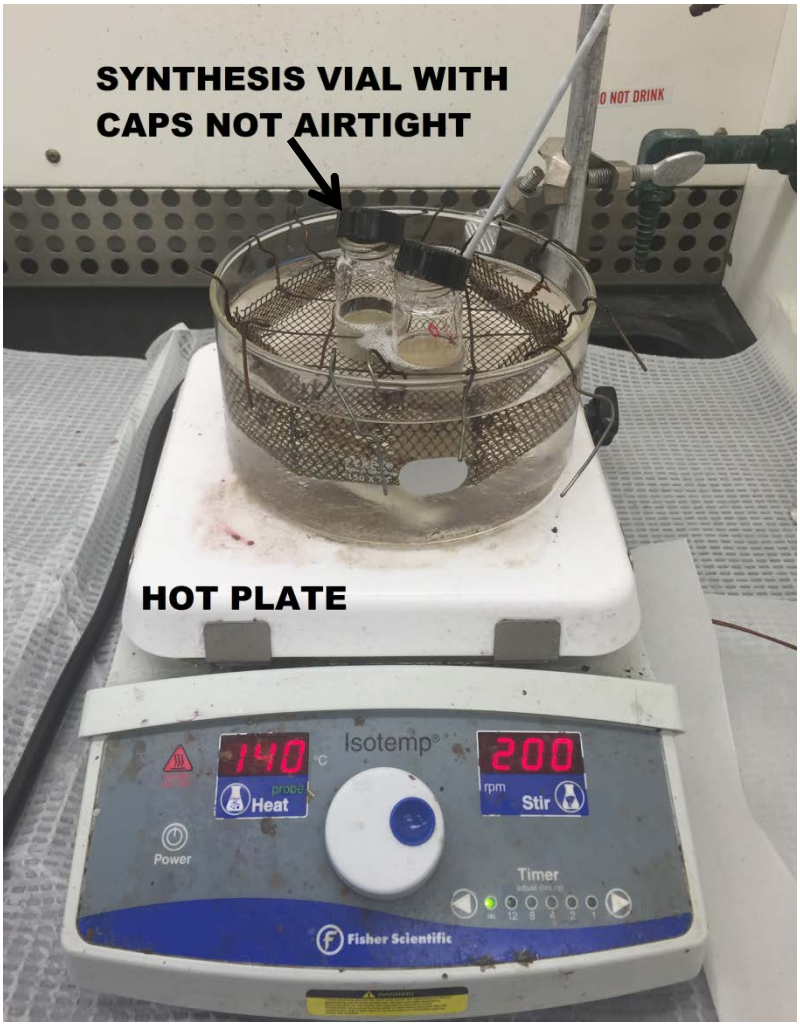

Figure 2-2: Solution phase synthesis setup. The figure above shows the Ag nanocube synthesis setup during the seed-growth stage, the 18-24 hour period immediately following reagent addition. The vials are partially submerged in the 140^{0} C oil bath with the caps positioned to allow airflow and O_2 supply to the solution.

Synthesis is carried out in 20 mL glass vials, which are partially submerged in a silicone oil heating bath, pre-heated to 140^{o} C. Each vial utilizes a magnetic stir bar (cleaned with piranha solution and/or aqua regia) to ensure equal mixing and a lack of thermal or concentration gradients in the vials which can lead to a loss of nanoparticle size and shape control. Initially the vials are filled with 10 mL of EG and allowed to pre-heat for at least one hour. The pre-heating step is necessary to allow for the formation of glycolaldehyde, which spontaneously forms as a result of EG oxidation at the elevated temperatures present. To the 10 mL of pre-heated EG solution, a 100 μL of prepared 30 mM HCl in EG in is added, which acts as an etchant during the seed growth step of the synthesis.

Once the HCl has been added and sufficiently mixed for approximately 5 minutes, the metal precursor and capping agent are added. The metal precursor for Ag nanocubes is silver nitrate ($AgNO_3$), which when dissolved yield Ag^+ ions in EG for reduction. The capping agent is polyvinylpyrrolidone (PVP) and controls growth and aggregation of correctly-shaped particles by binding selectively to certain facets of Ag nanocrystals. 3 mL each of prepared $AgNO_3$ (50 mg per 3 mL EG, 0.1M, 99% purity, Sigma Aldrich cat. No. 209139) and PVP (50 mg per 3 mL EG, 0.15 M by repeat unit, 55,000 M.W. Sigma Aldrich cat. No. 856568) are added simultaneously dropwise to the vials. The slow addition is necessary to prevent concentration gradients within the vial and prevent large changes in temperature upon addition, both of which can cause a loss of size and shape control of the nanoparticles.

Once the reagents have been all been added, the caps are lightly placed on the vials (so as to prevent any dust or objects from entering and allow gentle reflux but not to

be airtight) and allowed to sit in the heated oil bath for 18-24 hrs. This period is known as the seed-growth period of synthesis. Initially, the solution appears a milky white color as the result of AgCl initially precipitating after addition of $AgNO_3$. After about an hour, the milky white color gives way to a clear solution as the AgCl re-dissolves. During seed growth, the glycolaldehyde formed during the pre-heating of the EG first reduces Ag^+ ions in solution to form Ag^0 atoms, which begin to form small nanocrystals.[7] While the contents of the vial are kept exposed to air, the combination of HCl and O_2 prevents growth of the seeds beyond ~2 nm.[8] On the surface of these nanocrystals, the competitive processes of PVP binding and HCl-mediated etching help to determine the final shape of the nanocrystals. Because PVP binds more strongly to the (100) facet of Ag, (111) facets of the seeds are selectively etched away during seed growth. After the incubation period of 18-24 hrs, the result of this competitive process is the vast majority of seeds remaining are cubeoctahedral single crystal particles.

After 18-24 hrs incubation, the caps are tightly sealed onto the vials, effectively cutting the supply of fresh O_2 to the solution. This lack of O_2 ends the etching process that has until this point kept the Ag single crystal seeds at their very small size. With the etching process halted, free Ag^0 species in the solution can attach to the seeds, causing the nucleation of larger Ag nanocrystals. In this nucleation period, the PVP again plays an important role by binding more strongly to the (100) facets of the growing nanoparticles. This ensures that free Ag^0 species in the solution instead attach to any exposed (111) facets during the growth process. The anisotropic growth of Ag nanocrystals in this manner yields nanocrystals terminated on all sides by (100) facets and having a characteristic cubic shape.

The nucleation step is carried out for up to 8 hrs after closing the vials off from the atmosphere. During this time, the solution starts out clear before developing a transparent light yellow hue, indicating the beginning of nanoparticle growth into sizes that exhibit surface plasmon resonance (> 2 nm diameter). As growth continues, the solution darkens to a transparent yellow-green before turning opaque yellow. Once opaque, the intensity of the now-colloidal solution intensifies until the end of the synthesis. The synthesis is finished when colloidal solution leaves a bright red or purple hue on the sides of the vial when shaken and held up to light (See Figure 2-3 for an example). Synthesis is terminated by bringing the vial to room temperature quickly via immersion in water.

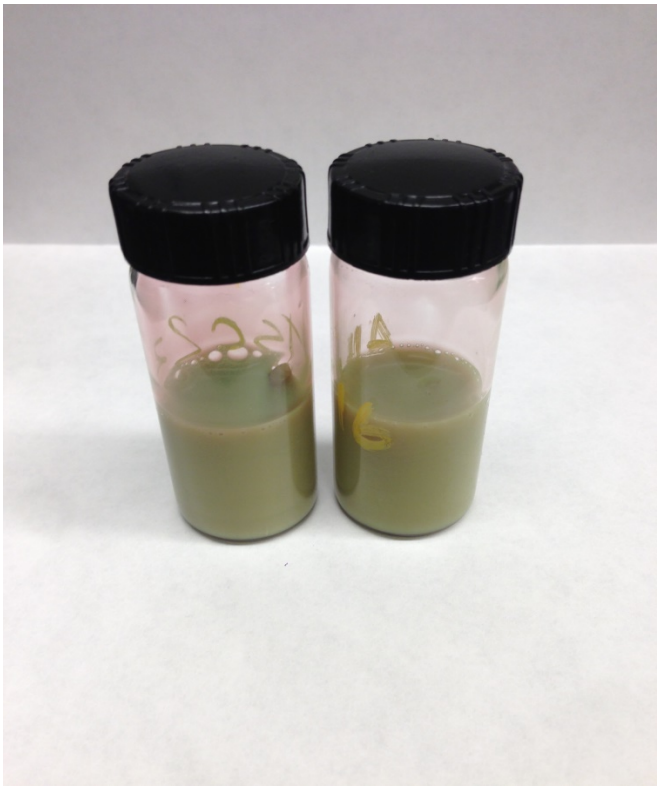

Figure 2-3: Completed Ag nanocube synthesis. When nanocube growth is finished, the colloidal Ag nanocube in EG solution appears a bright opaque yellow. Additionally, light allowed to pass through a thin film of the solution, as occurs when the solution sticks to the sides of the vial after gentle shaking, will appear red or purple.

2.3.2 Ag Nanoparticle-on-chip synthesis

Another set of experiments presented in this dissertation used a Ag nanoparticle-on-chip synthesis method. This synthesis resulted in spherical Ag nanoparticles chemically bound to a clean Si chip, and was both simple to carry out and yielded high quality samples for SERS measurements. This technique combines some of the key desired components of solution phase and "on-support" syntheses. As in the Ag nanocube synthesis of *Section 2.3.1*, in this method the Ag particles are formed from the reduction of $AgNO_3$ in solution. In this case however, the nanoparticles form chemically bound to the surface of a Si chip without the need for a polymeric stabilizer such as PVP. This simplifies the post-synthesis cleaning process, since the chips themselves can be rinsed without washing away the particles, and eliminates the need for post-synthesis deposition of Ag nanoparticles onto a Si chip for Raman measurements (see Section 2.4).

In a plastic centrifuge tube, up to 10 $1cm^2$ Si chips are placed in 10 mL deionized water. 150 μL concentrated ammonium hydroxide is added to the solution, giving a pH of about 12, and allowed to sit for 30 minutes. The basic conditions and preparation time allow for functionalization of the SiO_2 to contain O^- termini on the surface. After this time, 10 mg $AgNO_3$ dissolved in 5 mL deionized water is added to the solution, and the solution is allowed to sit for another 30 minutes allowing dissolved Ag^+ to anchor to the functionalized O^- and serve as points for nanoparticle nucleation. After this time, 5 mg $NaBH_4$ is freshly dissolved in 1 mL DI water and immediately added to the Ag solution. The solution is lightly shaken to ensure fast and equal dispersion of the BH_4, and at this time the solution should be dark yellow-gray. The Si chips, now with anchored Ag NPs on the surface, are removed from the solution and allowed to air dry, after which time

they are rinsed with DI water and allowed to dry again. A SEM image the rinsed and dried on-chip Ag nanoparticles is shown in Figure 2-4.

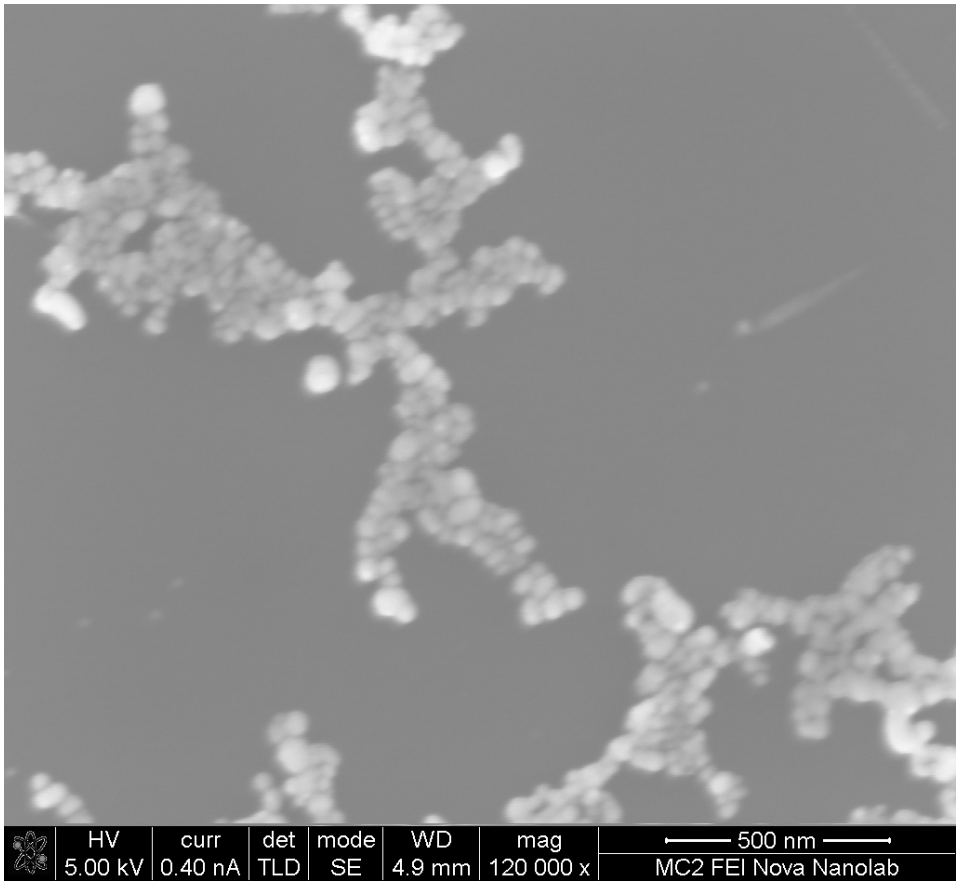

Figure 2-4: SEM image of on-chip Ag nanoparticles. The SEM image shows the on-chip synthesis method yields mostly spherical nanoparticles of relatively monodisperse size (diameter 35 ± 10 nm) in a clustered configuration, naturally maximizing the presence of plasmonic hot spots even at low loadings**.**

There are two main advantages to this synthesis process over fully solution-phase Ag nanoparticle formation. The first is that the anchoring of the particles on the Si chip eliminates the need for post-synthesis deposition steps in preparing for Raman measurements. The second is that the combination of anchored nanoparticles and fast reduction via $NaBH_4$ yields small and relatively monodisperse particle sizes without the

need for a stabilizing or capping agent. The lack of capping agents on the Ag nanoparticles increases the quality of Raman signals obtained, as the surface bound capping agents can often contribute unwanted peaks or noise to a sample Raman spectrum. Figure 2-5 demonstrates this, showing sample Raman spectra of methylene blue (MB) adsorbed on PVP-stabilized solution phase synthesis Ag nanocubes (green) and stabilizer-free on-chip Ag nanoparticles. In the range of Raman shift from 1100-1700 cm^{-1}, a large broad peak occurs in the spectrum using PVP-stabilized nanocubes. This is due to the Raman signal from the PVP itself (specifically the C=O and C-N stretches within the vinylpyrolidone monomers), and obscures the signal from MB in this range.[9] In some studies within this dissertation, where precise measurement of peaks within this range is of high importance, we must use the stabilizer free on-chip Ag nanoparticles for SERS measurements.

2.4 Raman spectroscopy experiments

The focal point of all the gathered data presented in this dissertation is the Raman data collected from many varying SERS platforms and probe molecules. This section describes in detail the key parameters and techniques used in gathering Raman data for this dissertation.

2.4.1 Raman sample preparation

Raman spectroscopy measures the vibrational fingerprint of a target molecule in response to and electronic excitation and relaxation. Surface-enhanced Raman scattering (SERS) takes advantage of the enhanced rates of this electronic excitation at the surface

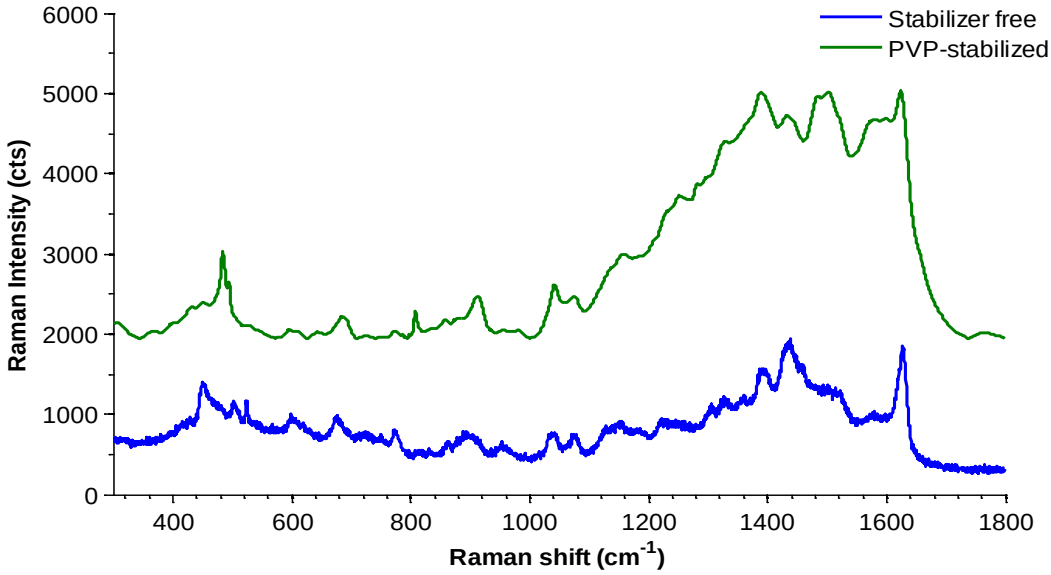

Figure 2-5: Sample Ag-MB Raman spectra using different Ag nanoparticle syntheses. The stacked Raman spectra show the presence of large unwanted peaks in the range of 1100-1700 cm^{-1} when PVP stabilized nanocubes are used in the prepared SERS platform The broad peaks in this range are present even when MB is not, ruling out changes in the orientation, and therefore the relative Raman peak intensities, as the cause of these unwanted peaks.

of plasmonic nanoparticles where electromagnetic fields are intensified by orders of magnitude.[5] In order to measure SERS spectra and gain insights into the mechanisms of charge transfer from plasmonic nanoparticles, a system of a plasmonic particle and a bound probe molecule is required. In these systems the plasmonic particles serve to enhance electromagnetic fields (and thus Raman signal) at their surface as well as provide charge in the form of excited electrons from the decay of surface plasmons. The probe molecule serves as a potential acceptor of charge from the plasmonic particle, as well as providing characteristic Raman signal as a result of undergoing Raman scattering processes.

For the results presented in Chapters 4 and 5, Ag nanocubes, synthesized according the procedure in *Section 2.3.1*, were used as the plasmonic platform while the probe molecule was methylene blue (MB), rhodamine 6G (R6G), or Acridine Orange (AO). After synthesis, the cubes were washed 5x by centrifugation and re-dispersion in a combination of acetone and ethanol. After washing, the cubes were dispersed in ethanol and small amount of NaCl was added to aid aggregation of Ag nanoparticles during the drying process. One of the probe molecules was added to the liquid solution at a concentration of 40μM and allowed to incubate for several hours to ensure full equilibrium adsorption of the dye onto the silver surface.[10] Adding the dyes while the particles are still in liquid solution allows the molecules to access all available adsorption sites on the Ag particles. Solid samples for spectroscopic studies were prepared by drop coating the solution onto a glass or silicon chip and allowing the ethanol solvent to evaporate, leaving behind a thin layer of silver-dye aggregates.

Figure 2-6 shows an optical micrograph of the as-prepared silver-dye aggregates on a Si chip. The samples are characterized by densely concentrated, disordered aggregates of nanoparticles dispersed relatively evenly across the chip surface. The aggregates provide optimal environments for SERS measurements as they contain many hot spots, points of close contact between plasmonic particles where electromagnetic field enhancement due to LSPR is highest.

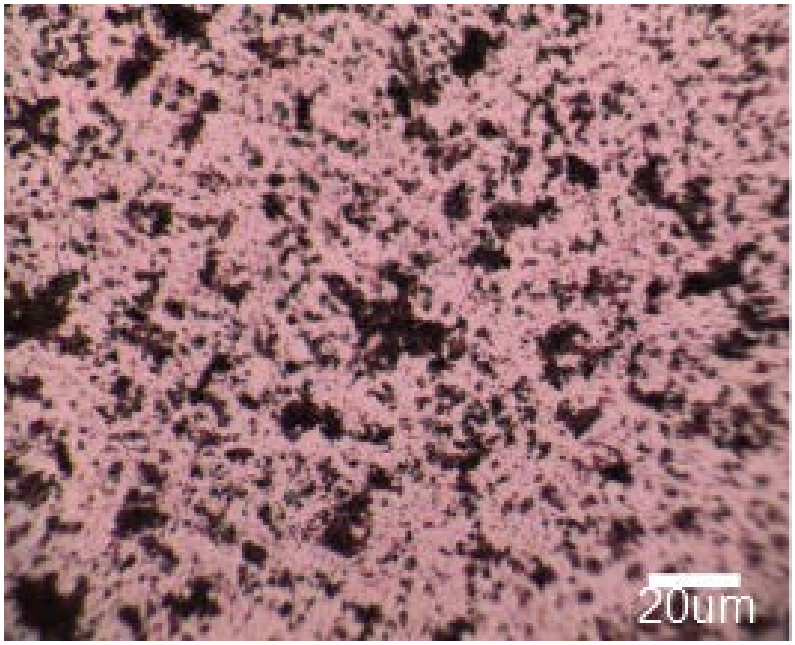

Figure 2-6: Optical micrograph of prepared SERS sample. The prepared Ag nanoparticle-dye samples deposited on a Si chip are characterized by their dense, disordered collection of aggregated nanoparticles, providing an optimal environment for SERS measurements.

In other experiments, for example those involving para-aminothiophenol (PATP) and its derivatives as the probe Raman molecule, the system used in the SERS experiments utilized the Ag nanoparticle-on-chip platform. The samples start with the rinsed and dried Ag nanoparticles on Si chips, synthesized according to the methods in *Section 2.3.2.* Para-aminothiophenol (PATP) is attached the nanoparticles by placing the Ag-on-Si chips in a solution of ~ 1 mM PATP dissolved in either H_2O or acetone. The chips are submerged in the PATP solution for 30 minutes before being removed, allowed to dry, sequentially rinsed with H_2O and acetone, and allowed to dry again. The PATP-on-Ag-on-Si chips are now ready for Raman measurements.

2.4.2 Collection of anti-Stokes and Stokes Raman spectra

The main purpose of the samples prepared as described in the above sections is for collecting Raman spectra and using that data to gain insight into the mechanisms of charge transfer in these plasmonic nanoparticle systems. As described in Chapter 1, Raman spectroscopy is the study of inelastic photon scattering by a molecule as a result of polarization (excitation) by an incoming photon and subsequent relaxation of the molecule within its vibrational energy landscape. Changes in the energy of scattered photons are measured as Stokes (photon energy loss) or anti-Stokes (photon energy gain). The change in the energy of the photon upon Raman scattering is referred to as the Raman shift and is measured in inverse centimeters (cm^{-1}), with Stokes shifts conventionally given positive values and anti-Stokes shifts given negative values.

Raman spectroscopy utilizes a monochromatic laser source to polarize molecules for measurement. After interaction with the sample, Raman scattered photons are collected by a lens and funneled to the detector, usually a charge-coupled device (CCD), where the wavelength/energy of the photons is measured. Stokes and anti-Stokes Raman spectra presented in this dissertation were gathered using a Horiba LabRAM HR system under excitation from either a 532-nm diode-pumped solid state laser or a 785-nm diode laser.

In addition to the two lasers, there are a number of adjustable parameters in the Raman system used that can affect the molecule's response to the laser and the signal measured. They are given in the list below with their description and ranges used in the studies in this dissertation:

i. Laser Intensity: The power, or intensity of the laser used in Raman spectroscopy is a measure of the number of monochromated laser photons impinging on the sample spot, given in this dissertation in terms of photons/cm^2/sec. A higher intensity, *i.e.*, more photons impinging on the sample, will lead to a higher rate of Raman scattering within the material. The ratio of anti-Stokes to Stokes signal for a given Raman shift will vary with laser intensity differently in systems that exhibit charge transfer than in those that do not. It should be noted that high Raman laser intensities, especially for higher energy photons, can cause damage and a loss of Raman signal from the sample. This is particularly true in SERS measurements where the photon energy is confined and amplified at the surface of plasmonic nanoparticles. In the Horiba LabRAM HR system, Raman laser intensity is varied through the use of neutral density (ND) filters that allow only a known percentage photons through. ND filters in this system ranged from 0.1% to 100% intensity. At 100% intensity (*i.e.*, no ND filter) both the 532 nm and 785 nm laser were tuned such that their intensities were an equal $1.2 * 10^{21}$ photons/cm^2/sec.

ii. Acquisition time: The acquisition time in Raman spectroscopy refers to the amount of time the detector collects photons within a given wavenumber range. The longer the acquisition time, the more photons can be collected and the stronger the signal. If the acquisition time for a given sample is too long however, the total signal can be higher than the detector limit, registering an error in the software and possible damaging the detector. Acquisition times in the Raman studies in this dissertation ranged from 1 to 120 seconds.

iii. Objective lens magnification: After passing through the ND filter and system optics, the incident laser is focused onto the sample through an objective lens. The lens is manually adjusted for optimal focus onto the sample. In solid samples, the laser is focused on nanoparticle aggregates. In liquid samples, the laser focus is near the surface of the liquid. In these studies, a 50x objective magnification lens was normally used. However, in cases where it was not possible to bring the lens close to the surface of the sample, such as when the sample is inside the reactor, the long-focal-length 10x objective lens was used.

In a typical Raman measurement the sample, aggregates of plasmonic nanoparticles and a dye on a Si chip, are placed directly under the objective lens. The lens is visually centered and focused on an aggregate. The laser wavelength, ND filter percent, acquisition time, and objective lens magnification are input into the software, and the range of wavenumbers to measure is also chosen. Each measurement yields a single anti-Stokes and Stokes spectrum for analysis.

2.4.3 In-situ reactor Raman measurements

For a number of experiments, it was necessary to control either the temperature or atmosphere surrounding the sample during Raman measurement. For those studies, a temperature-controlled Harrick Praying Mantis reaction chamber, designed specifically for Raman spectroscopy, was used. A schematic of the reactor in the Raman setup is shown in Figure 2-7. The key feature of this reactor is the optically transparent window which allows the Raman laser to impinge upon the sample while it is kept under controlled temperature and atmosphere. The reactor also consists of inlet and outlet connections which during use are fixed to a mass flow controller and compressed gas

tank to allow for controlled rate of flow of a choice gas through the reactor. Temperature is controlled within the reactor via an external controller connected to the reactor thermocouple and heater.

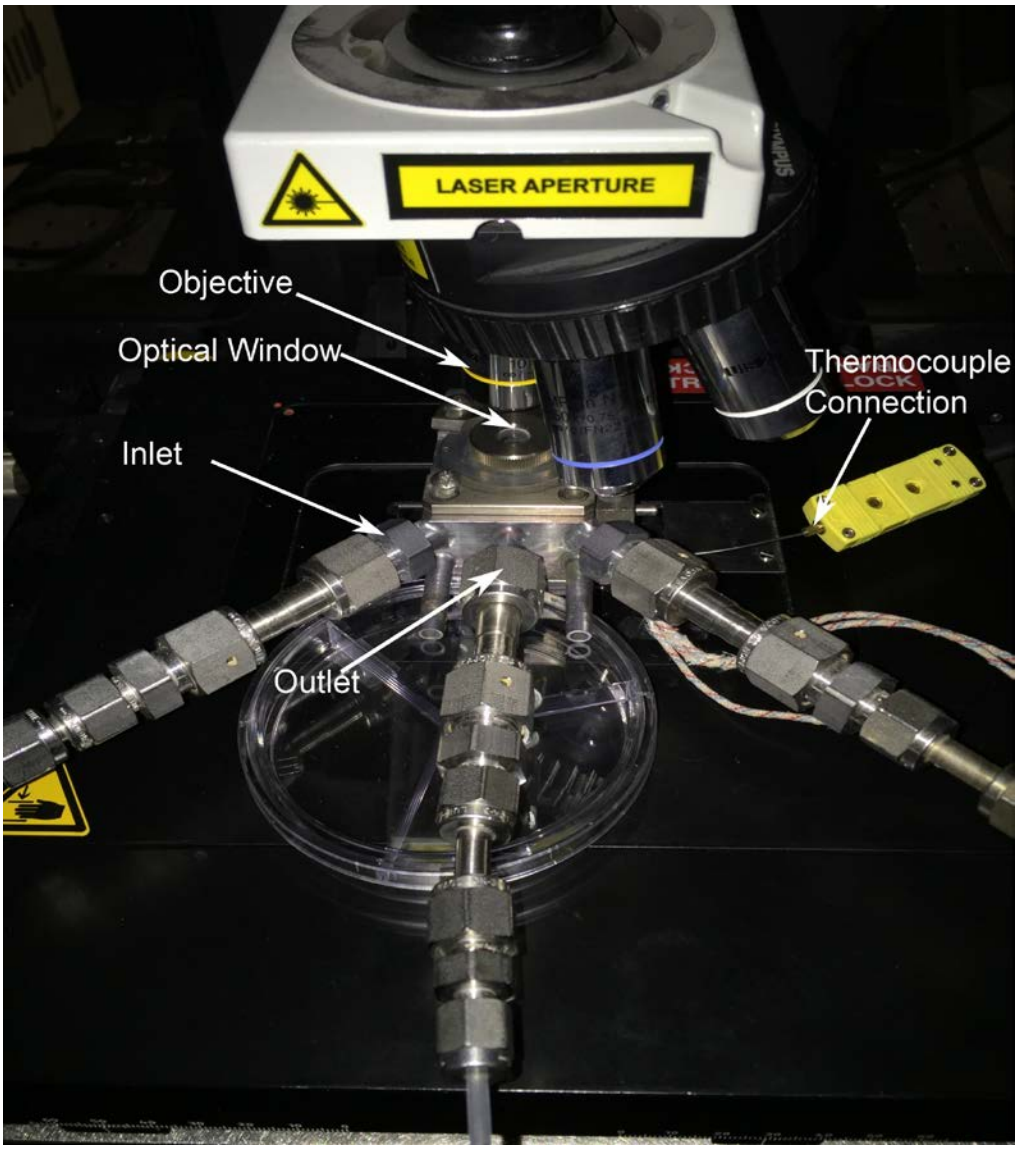

Figure 2-7: Reactor setup for Raman measurement. Depiction of the Harrick Praying Mantis reactor setup under the Raman spectrometer optics for in-situ and controlled environment Raman measurements. The diagram shows the key components of the setup: optical window, gas inlet and outlet, thermocouple, and Raman objective lens.

In reactor studies presented herein, a sample of plasmonic particles and dye on a silicon chip was placed inside the chamber, with the transparent reactor window allowing Raman spectra to continue to be collected. The temperature of the sample within the reactor could then be controlled, and select gas (usually pure nitrogen to provide an inert atmosphere) could be flowed through the reactor. The longer focal length10x objective lens was used to allow focusing on the sample within the reactor through the window. Raman spectra were collected as described in *Section 2.4.2*.

2.5 Raman data analysis

The raw Raman spectra collected via the methods described in Section 2.4 contain a multitude of invaluable data that aided in illuminating the mechanisms of charge transfer in plasmonic systems. Unlike most Raman studies that focus entirely on Stokes scattering, since it is the much stronger of the two in terms of signal strength, the Raman studies in this dissertation analyzed the information contained in simultaneous anti-Stokes and Stokes Raman spectra from the same experimental run. Special attention was paid to the relationship between anti-Stokes and Stokes peaks within a single spectrum, as there is a direct relation between the ratio of a given anti-Stokes and Stokes peak in a spectrum and the apparent vibrational population distribution within molecules on the surface.[11]

The most important single piece of data for the analyses in these studies is the anti-Stokes to Stokes peak ratios from a single spectrum. The first calculation to perform with this data is the deviation of the ratio from what is expected based on an equilibrium vibrational population distribution in the sample. Deviation from the expected anti-Stokes

to Stokes ratio forms the basis for the evidence of charge transfer presented in Chapter 4 of this thesis. Using this information and further calculation, it is possible to derive a "vibrational temperature" of an ensemble of adsorbates on the surface of plasmonic particles. The same anti-Stokes spectrum used in these calculations provides important information about the substrate, *i.e.*, the plasmonic particles themselves, in its background signal. Usnig this background signal, it is possible to calculate an "electronic temperature" of the particles. This gives us the ability to calculate and compare two different temperatures using a single Raman spectrum, and forms the basis for the conclusions to studies in Chapter 5 of this dissertation.

Careful analyses of the data using the methods described in the following sub-sections provide the backbone for the conclusions drawn from the studies in this dissertation. While many general inferences can be made from a qualitative analysis of Stokes and anti-Stokes data, the studies performed focused much more on quantitative analysis of Raman data, as it provides a more robust understanding of the data and can uncover trends in the data that would otherwise go unrecognized.

2.5.1 Calculation of deviation from expected anti-Stokes/Stokes ratios (K)

In Raman scattering processes, energy is conserved in the inelastic photon scattering through the transfer of energy between the photon and the vibrational modes of a molecule. It is through this process that a Raman spectrum can provide valuable information about the vibrational structure and population distribution in a molecule. Of particular importance to the studies in this dissertation is the vibrational mode population distribution within a molecule, which is heavily influenced by occurrences of charge transfer.[12]

In a vibrationally equilibrated molecule, the fraction of molecules that will have a particular vibrational mode excited at any given time can be related to the temperature and the energy of the vibrational mode through the Boltzmann distribution, given in Equation 2-1:

$$\rho = e^{-E_{vibr}/k_{B*T}} \quad (2\text{-}1)$$

where ρ is the fraction of molecules in which a particular mode is excited, E_{vibr} is the energy of the mode, k_B is the Boltzmann constant ($8.617*10^{-5}$ eV/K), and T the temperature. Because Raman scattering probes the vibrational energy landscape of a sample, the ratio of anti-Stokes to Stokes peak heights for a given vibrational mode is determined by population distribution and can, when the molecule is in vibrational equilibrium, be predicted by the Boltzmann distribution ρ.[13]

In some instances, e.g. when the system is undergoing charge transfer from plasmonic particle to attached adsorbate, the vibrational energy distribution deviates from the Boltzmann distribution, and thus the anti-Stokes to Stokes peak ratio is altered. This deviation is a key signature of charge transfer in plasmonic systems, and can be quantified.

To eliminate factors affecting the anti-Stokes to Stokes ratio that are not caused by changes in the vibrational population distribution (which are discussed in detail in Chapter 3), the anti-Stokes to Stokes ratio for a sample molecular vibration is not compared directly to the Boltzmann distribution, but instead to a standard “expected” ratio that is experimentally measured from a molecule on an identical SERS platform and

with a known equilibrium vibrational population distribution. The degree to which the anti-Stokes to Stokes ratio exceeds the expectation of an equilibrium vibrational distribution is described through the quantity, K, and is calculated using the Equation 2-2:

$$K(\nu_m) = \frac{\rho_{sample}}{\rho_{control}}(\nu_m) = \frac{I_{aS}^{sample}(\nu_m)/I_S^{sample}(\nu_m)}{I_{aS}^{control}(\nu_m)/I_S^{control}(\nu_m)} \qquad (2\text{-}2)$$

where I_{aS}^{sample} and I_S^{sample} are the measured anti-Stokes and Stokes intensities, respectively, for the molecule being measured at a given vibrational mode energy (ν_m). $I_{aS}^{control}$ and $I_S^{control}$ are the anti-Stokes and Stokes intensities, for the similar vibrational mode in the control molecule known to have be vibrationally equilibrated. By this calculation, molecules with higher than expected anti-Stokes peak signal will have K value greater than one, while a molecule with vibrational energy distributed according to the Boltzmann distribution will have a K value equal to one. Using Equation 2-2, each individual vibrational mode within a sample Raman spectrum can have a unique K value, provided that the mode exhibits a measureable anti-Stokes peak.

2.5.2 Calculation of adsorbate vibrational mode temperatures

While the K value for a given vibrational mode in a sample can tell us the deviation from the expected value of an anti-Stokes peak, it is often useful to perform a different quantitative calculation to compare the extent of vibrational excitation in a molecule compared to its surroundings. For this purpose, we can calculate, using the same anti-Stokes to Stokes peak ratios in a given spectrum, the *temperature* of the vibrational mode.[14] This temperature is then compared to the actual temperature of the surrounding environment or other temperature values calculated using the Raman data.

The vibrational temperature of a specific mode can be calculated based on the anti-Stokes to Stokes ratio for that mode, similar to K, because it is based on the same Boltzmann distribution (Equation 2-1). In this case, Equation 2-1 is rearranged as shown in Equation 2-3 to calculate temperature as a function of anti-Stokes to Stokes ratio:

$$T_{vibr} = -\frac{E_{vibr}}{k_B * \ln(I_{aS}/I_{St})} \quad (2\text{-}3)$$

where T_{vibr} is the calculated temperature of the mode, E_{vibr} is the energy of the mode, and I_{aS} and I_{St} the anti-Stokes and Stokes intensities (properly calibrated as described in Chapter 3) of that vibrational mode, respectively.

2.5.3 Calculation of Ag nanoparticle electronic temperatures

In addition to the behavior of the probe molecule in instances of Raman scattering, in SERS, where the probe is anchored to a plasmonic metal surface, the Raman spectrum can be used to study the response of the plasmonic substrate to laser illumination. Hugall and Baumberg showed recently that the background SERS signal, present in all SERS measurement and independent of the probe molecule attached, provides important information about the temperature of the plasmonic substrate.[15] This is because the electrons within the plasmonic particle can participate in Raman scattering on their own.

The local nanoparticle temperature can be measured based on the intensity of the SERS anti-Stokes background signal.[16] The central concept is that the anti-Stokes background intensity measures the rate of emission of anti-Stokes shifted photons in

response to the photon-induced relaxation of electrons within the metal nanoparticle from the occupied electronic states just above the Fermi level to the unoccupied states just below the Fermi level. The electrons follow a Fermi-Dirac distribution within the nanoparticle based on their temperature. The local equilibrated electronic temperature of the metal can be derived from a rearrangement of this distribution through the relationship in Equation 2-4:

$$I_{aS,\,background} = I_{aS,0}\left[e^{E_{Raman}/k_B*T} + 1\right]^{-1} \qquad (2\text{-}4)$$

where $I_{aS,background}$ is the intensity of the anti-Stokes SERS background at a given energy of Raman shift, E_{Raman}, and $I_{aS,0}$ is the intensity of the anti-Stokes SERS at $E_{Raman} = 0$. Equation 2-4 can easily be rearranged to a linear form:

$$\ln\left(\frac{I_{aS,0}}{I_{aS}} - 1\right) = \frac{1}{k_B T} * E_{Raman} \qquad (2\text{-}5)$$

We calculate the theoretical $I_{aS,0}$ by looking at the anti-Stokes background signal at high Raman shifts, where:

$$e^{E_{Raman}/k_B T} \gg 1 \qquad (2\text{-}6)$$

and therefore:

$$I_{aS,0}\left[e^{E_{Raman}/k_B T} + 1\right]^{-1} \sim I_{aS,0} * e^{-E_{Raman}/k_B T}$$

$$I_{aS} = I_{aS,0} * e^{-E_{Raman}/k_B T}$$

$$\ln(I_{aS}) = \ln(I_{aS,0}) - \frac{E_{Raman}}{k_B T} \quad (2\text{-}7)$$

Here, the intercept of the best fit line when plotting $\ln(I_{aS})$ *versus* E_{Raman} is equal to $\ln(I_{aS,0})$. Once this is calculated, we can more accurately determine the local metal temperature by now including lower energy Raman shifts and plotting $\ln(I_{aS,0}/I_{aS} - 1)$ *versus* E_{Raman} as Equation 2-4 would suggest. The slope of the best fit line will be equal to $1/k_BT$. In this way, the *electronic temperature* of the plasmonic SERS substrate can be calculated and compared to both the actual ambient temperature and the probe molecule vibrational mode temperatures.

2.6 Plasmonic particle and platform characterization

In addition to Raman spectroscopy, there were secondary characterization techniques used in the studies of this dissertation to learn about the properties of the plasmonic Ag metal nanoparticles being used. The optical response, *i.e.*, the interaction of the plasmonic nanoparticles in response to light, was probed using UV-vis spectroscopy. Additionally, structural information on individual nanoparticles as well as how large numbers of them aggregated in the SERS samples described in *Section 2.4.1* was obtained with SEM and TEM microscopy. A brief description of those techniques as well as the methods by which data were obtained using them is given in the following sub-sections.

2.6.1 UV-vis spectroscopy

UV-vis spectroscopy is a simple yet highly useful technique that can give information on how plasmonic particles are interacting with light across the entire visible spectrum. The key concept is the measurement of the percent transmittance of light from a scanning monochromated source as it passes through a sample to be measured. Because any light that is scattered or light that is absorbed by the sample does not make it to the detector, UV-vis spectroscopy measures extinction due to plasmon resonance where the sample is plasmonic particles. As explained in Chapter 1, the UV-vis extinction from plasmonic particles tracks the electric field enhancement that is key in Raman measurements, and thus UV-vis spectroscopy is a useful supplemental characterization tool for the studies in this dissertation.

UV-vis extinction spectroscopy was conducted using a Thermo Evolution 300 spectrophotometer. For liquid samples, a dilute solution of the sample in water was placed in a cuvette for spectral measurement. In the case of solid samples, such as those used in Raman studies, the substrate for plasmonic particles was a glass slide which could be placed in the path of the UV-vis light source for spectral collection.

2.6.2 SEM and TEM characterization

Scanning electron microscopy (SEM) and transmission electron microscopy (TEM) are two common techniques for visualization of objects with sizes well below the diffraction limit of light. They both beam electrons toward a sample and measure the electrons after they are scattered by the sample (SEM) or transmitted through the sample (TEM) to a detector. By measuring the variation of electron response over an area, the microscopes can create an image of the sample. SEM can measure a wide variety of

samples as long as they are not damaged by high vacuum or the electron beam, while for TEM, which has a higher resolution, samples must be specially prepared to be ultra-thin and allow electron transmission.

TEM samples for images presented in this dissertation were prepared by depositing ~2 μL of the colloidal nanoparticle solution on a carbon film TEM grid (the amount deposited was chosen to mimic the density of particles used in optical and Raman studies). Aberration corrected TEM (JEOL 3100, accelerating voltage 300 kV) was used to characterize the Ag nanocubes prior to their placement on Raman-ready silicon chip samples.

The samples used for SEM images were simply the samples prepared for Raman spectroscopy measurements as described in *Section 2.4.1*. SEM images were gathered using an FEI Nova 200 nanolab SEM/FIB. Accelerating voltage for the measurements was between 5 and 30 kV depending on the sample in order to get optimal resolution for the images.

2.7 Theoretical techniques

To supplement further the experimental results of this dissertation and to better understand the physical underpinnings of them, a number of theoretical calculations were carried out. Finite-difference time-domain (FDTD) simulations were used to predict the optical response and near-field electric field enhancements at the wavelengths used in the Raman studies for the plasmonic Ag nanoparticles. The combination of the simulation results with the UV-vis spectra from the prepared plasmonic nanoparticle samples was used to support the Raman results and conclusions regarding plasmon-induced charge

transfer. Density functional theory (DFT) calculations were performed to learn about the interaction of the probe molecules with the plasmonic surface. The simulations served to show the nature of chemisorption between the probe molecules and the plasmonic nanoparticles. The methods by which all theoretical calculations for this dissertation were performed are given in the sub-sections below.

2.7.1 Finite-difference time-domain (FDTD) simulations

Finite-difference time-domain (FDTD) simulations were carried out using the Meep simulation package.[17] The simulations were performed in a three-dimensional grid measuring 294 nm x 294 nm x 294 nm. An additional 50 nm of perfectly matched layer was added to all sides of this grid. The space between grid points was 1 nm for all but one simulation in which the much more computationally expensive 0.5nm mesh was used to ensure that a shrinking mesh size did not change significantly the behavior of the field intensities within gaps between particles. The dielectric function for silver was obtained from data published by Rakic et al[18] Nanocube dimers were arranged in a number of orientations, including face-to-face, face-to-edge, edge-to-edge, and corner-to-corner; each dimer system was tested with inter-particle separations of both 1nm and 2nm. Additionally, Ag nanocube trimers were also simulated in edge-face-edge and edge-edge-edge orientations with 1nm separations. The source wavelengths studied matched those of the laser in the Raman setup, 532nm and 785nm. The energy from the source propagated perpendicular to the interparticle axis; the polarization of the source was alternately perpendicular and parallel to the interparticle axis in separate simulations. Field enhancement data was visualized on the x-y and x-z planes. Integrated field values

were calculated by finding the average value of the electric field data points located on the nanoparticle surfaces only.

2.7.2 Density functional theory (DFT) calculations

Density Functional Theory (DFT) calculations were performed using real space grid-based projector augmented wavefunction DFT implemented in the GPAW software package.[19] The exchange-correlation interaction was approximated using the revised Perdew-Burke-Ernzerhof (RPBE) functional.[20,21] The Ag[100] and Ag[211] surfaces were modeled using 3 x 3 slabs and 2 x 3 slabs, respectively. All systems used 4-layer slabs, with 10 Å of vacuum space. Pyridine molecules were adsorbed vertically over a top site [100] or above a step site [211] to match the predominant facets present in the synthesized Ag nanocubes. Multiple adsorption configurations were tested for the molecules on the Ag surfaces.

2.8 References

(1) Satterfield, C. N. *Heterogeneous Catalysis in Industrial Practice*; 2nd Ed.; McGraw Hill Book Co.: New York, 1991.

(2) Xia, Y.; Xiong, Y.; Lim, B.; Skrabalak, S. E. Shape-Controlled Synthesis of Metal Nanocrystals: Simple Chemistry Meets Complex Physics? *Angew. Chem. Int. Ed. Engl.* **2009**, *48*, 60–103.

(3) Im, S. H.; Lee, Y. T.; Wiley, B.; Xia, Y. Large-Scale Synthesis of Silver Nanocubes: The Role of HCl in Promoting Cube Perfection and Monodispersity. *Angew. Chem. Int. Ed. Engl.* **2005**, *44*, 2154–2157.

(4) Christopher, P.; Ingram, D. B.; Linic, S. Enhancing Photochemical Activity of Semiconductor Nanoparticles with Optically Active Ag Nanostructures: Photochemistry Mediated by Ag Surface Plasmons. *J. Phys. Chem. C* **2010**, *114*, 9173–9177.

(5) Schatz, G. C.; Young, M. A.; Van Duyne, R. P. *Surface-Enhanced Raman Scattering*; Kneipp, K.; Moskovits, M.; Kneipp, H., Eds.; Topics in Applied Physics; Springer Berlin Heidelberg, 2006; Vol. 103.

(6) Rycenga, M.; Cobley, C. M.; Zeng, J.; Li, W.; Moran, C. H.; Zhang, Q.; Qin, D.; Xia, Y. Controlling the Synthesis and Assembly of Silver Nanostructures for Plasmonic Applications. *Chem. Rev.* **2011**, *111*, 3669–3712.

(7) Sun, Y.; Mayers, B.; Herricks, T.; Xia, Y. Polyol Synthesis of Uniform Silver Nanowires: A Plausible Growth Mechanism and the Supporting Evidence. *Nano Lett.* **2003**, *3*, 955–960.

(8) Wiley, B.; Herricks, T.; Sun, Y.; Xia, Y. Polyol Synthesis of Silver Nanoparticles: Use of Chloride and Oxygen to Promote the Formation of Single-Crystal, Truncated Cubes and Tetrahedrons. *Nano Lett.* **2004**, *4*, 1733–1739.

(9) Ren, M.; Jin, Y.; Chen, W.; Huang, W. Rich Capping Ligand–Ag Colloid Interactions. *J. Phys. Chem. C* **2015**, acs.jpcc.5b09958.

(10) Ghaedi, M.; Heidarpour, S.; Nasiri Kokhdan, S.; Sahraie, R.; Daneshfar, A.; Brazesh, B. Comparison of Silver and Palladium Nanoparticles Loaded on Activated Carbon for Efficient Removal of Methylene Blue: Kinetic and Isotherm Study of Removal Process. *Powder Technol.* **2012**, *228*, 18–25.

(11) Kneipp, K.; Wang, Y.; Kneipp, H.; Itzkan, I.; Dasari, R.; Feld, M. Population Pumping of Excited Vibrational States by Spontaneous Surface-Enhanced Raman Scattering. *Phys. Rev. Lett.* **1996**, *76*, 2444–2447.

(12) Boerigter, C.; Campana, R.; Morabito, M.; Linic, S. Evidence and Implications of Direct Charge Excitation as the Dominant Mechanism in Plasmon-Mediated Photocatalysis. *Nat. Commun.* **2016**, *7*, 10545.

(13) Maher, R. C.; Galloway, C. M.; Le Ru, E. C.; Cohen, L. F.; Etchegoin, P. G. Vibrational Pumping in Surface Enhanced Raman Scattering (SERS). *Chem. Soc. Rev.* **2008**, *37*, 965–979.

(14) Browne, W. R.; McGarvey, J. J. The Raman Effect and Its Application to Electronic Spectroscopies in Metal-Centered Species: Techniques and Investigations in Ground and Excited States. *Coord. Chem. Rev.* **2007**, *251*, 454–473.

(15) Hugall, J. T.; Baumberg, J. J.; Mahajan, S. Disentangling the Peak and Background Signals in Surface-Enhanced Raman Scattering. *J. Phys. Chem. C* **2012**, *116*, 6184–6190.

(16) Hugall, J. T.; Baumberg, J. J. Demonstrating Photoluminescence from Au Is Electronic Inelastic Light Scattering of a Plasmonic Metal: The Origin of SERS Backgrounds. *Nano Lett.* **2015**, *15*, 2600–2604.

(17) Oskooi, A. F.; Roundy, D.; Ibanescu, M.; Bermel, P.; Joannopoulos, J. D.; Johnson, S. G. Meep: A Flexible Free-Software Package for Electromagnetic Simulations by the FDTD Method. *Comput. Phys. Commun.* **2010**, *181*, 687–702.

(18) Rakic, A. D.; Djurišic, A. B.; Elazar, J. M.; Majewski, M. L. Optical Properties of Metallic Films for Vertical-Cavity Optoelectronic Devices. *Appl. Opt.* **1998**, *37*, 5271.

(19) Enkovaara, J.; Rostgaard, C.; Mortensen, J. J.; Chen, J.; Dułak, M.; Ferrighi, L.; Gavnholt, J.; Glinsvad, C.; Haikola, V.; Hansen, H. A.; *et al.* Electronic Structure Calculations with GPAW: A Real-Space Implementation of the Projector Augmented-Wave Method. *J. Phys. Condens. Matter* **2010**, *22*, 253202.

(20) Hammer, B.; Hansen, L. B.; Nørskov, J. K. Improved Adsorption Energetics within Density-Functional Theory Using Revised Perdew-Burke-Ernzerhof Functionals. *Phys. Rev. B* **1999**, *59*, 7413–7421.

(21) Wellendorff, J.; Lundgaard, K. T.; Møgelhøj, A.; Petzold, V.; Landis, D. D.; Nørskov, J. K.; Bligaard, T.; Jacobsen, K. W. Density Functionals for Surface Science: Exchange-Correlation Model Development with Bayesian Error Estimation. *Phys. Rev. B* **2012**, *85*, 235149.

(22) Linic, S.; Christopher, P.; Ingram, D. B. Plasmonic-Metal Nanostructures for Efficient Conversion of Solar to Chemical Energy. *Nat. Mater.* **2011**, *10*, 911–921.

Chapter 3

Corrections to the Raman anti-Stokes Data to Accurately Reflect the Vibrational Population Distribution of the Sample Molecule

3.1 Summary

In this chapter, one of the pivotal processes for accurate analysis of anti-Stokes Raman data is laid out in detail. In full anti-Stokes and Stokes Raman spectral data the raw signal is not a direct representation of the vibrational population distribution within the sample molecules being measured. The two main physical underpinnings of this discrepancy are first introduced and fundamentally discussed. The method for correcting Raman data for these confounding factors, both individually and in a single control measurement, is then explained. Finally, the results of this correction factor measurement specifically for the Ag nanocube-methylene blue (Ag-MB) samples used in Chapters 4 and 5 of this dissertation are given, along with details on how they were used in further experiments.

3.2 Introduction

In full anti-Stokes and Stokes Raman spectral data the raw signal, that is what the charge coupled device (CCD) measures and translates to counts of signal within the software, is not a direct representation of the vibrational population distribution within the sample molecules being measured.[1] This is problematic in studies that use the quantitative anti-Stokes and Stokes Raman data to draw conclusions about the vibrational population distribution of a system. Chief among these studies are those that deal with charge transfer from plasmonic nanoparticles to attached adsorbate molecules, where one of the main characteristics of such a system is a non-thermalized population distribution of vibrational molecular modes.[2]

The vibrational population distribution of thermally equilibrated molecules follows a Boltzmann exponential decay. It has been established that in such a thermally equilibrated system (*i.e.*, one without charge transfer), the surface-enhanced Raman scattering (SERS) anti-Stokes to Stokes signal ratio should therefore follow the Boltzmann distribution that is dependent on the temperature of the system and the energy of the Raman shift. However, in the case of SERS studies (such as those featured in this dissertation) the *measured* anti-Stokes to Stokes ratio at a given frequency deviates from the Boltzmann distribution even for a thermally equilibrated system. These deviations are the result of two key factors that can be corrected for in order to discern the true vibrational population distribution from the SERS data.

3.3 Physical causes of anti-Stokes signal error

3.3.1 Charge-coupled device (CCD) error

The first factor contributing to error in the measured anti-Stokes/Stokes intensity ratio is attributed to the Raman signal detector (a charge-coupled device image sensor, or CCD) that detects Stokes and anti-Stokes Raman scattered photons for a given incident laser. The CCD (Horiba Synapse Model #354308, 400-1000 nm range) used in the studies of this dissertation is not equally sensitive to photons of all wavelengths, especially near the edge of its detection range. Because of this, when using the 785nm laser in the Raman experiments the CCD is more sensitive to the anti-Stokes scattered photons, which come off at shorter wavelengths nearer the center of the CCD range, than the Stokes scattered photons, which come off at longer wavelengths. For larger Raman shifts (larger ν_m), the difference between frequencies of anti-Stokes and Stokes scattered photons is larger resulting in a greater difference in CCD sensitivity.

3.3.2 Unequal SERS enhancements of Stokes and anti-Stokes photons

The second factor causing deviations in the measured anti-Stokes/Stokes intensity ratio from the actual vibrational mode distribution is unique to SERS measurements (*i.e.*, it doesn't play a role in non-surface enhanced Raman). It is due to the wavelength-dependent electromagnetic enhancements of Raman Stokes and anti-Stokes shifted photons on SERS substrates.[3] Without a charge transfer process, SERS enhancements in Raman scattering are caused by high electric fields present around plasmonic nanoparticles such as silver.[4] The intense electric field increases Raman scattering rates. This enhancement factor (Σ) can be approximated by:

$$\Sigma = (|\boldsymbol{E}(\nu_i)|^2 * |\boldsymbol{E}(\nu_i \pm \nu_m)|^2) \qquad (3\text{-}1)$$

where **E**(ν) is the local electromagnetic field enhancement at a photon frequency ν. ν_i and ($\nu_i \pm \nu_m$) are the frequencies of the incident (*i.e.*, laser) photon and scattered (*i.e.*, Raman shifted) photon, respectively.

Equation 3-1 shows that this electromagnetic enhancement for a particular Raman event is dependent on the local value of electric field intensity at the frequencies of both the incoming and the exiting (Raman-shifted) photons and this behavior has been shown experimentally.[5] FDTD simulations show that the local electric field intensities around a single particle or cluster of particles are highly wavelength-dependent.[6,7] The difference in wavelengths of Stokes and anti-Stokes scattered photons associated with the same vibrational mode ν_m can lead to unequal electromagnetic enhancements in Stokes and anti-Stokes intensities due to unequal electric field intensities at the frequencies of Stokes and anti-Stokes scattered photons.[3]

It is important to recognize that the electromagnetic SERS mechanism is dependent only upon the location of the adsorbate and not the chemical structure or nature of adsorption, and also it does not alter the actual vibrational mode population distribution, characteristics untrue of charge-transfer enhancement.[8] The extent of electromagnetic enhancement is effectively a function of the plasmonic SERS platform rather than the specific molecule being tested. The following sections outline how to take advantage of this fact to measure the extent to which unequal electromagnetic enhancements at different wavelengths of Raman shifted photons alter measured anti-Stokes/Stokes intensity ratios.

3.4 Experimental methods for determining the anti-Stokes correction factor

3.4.1 Non-SERS method for correcting CCD error

To quantify the difference in anti-Stokes and Stokes signal ratios purely due to the properties of the detector, a previously used procedure was followed.[9,10] In this calibration process, Raman experiments measuring anti-Stokes and Stokes scattering intensities from a molecule (in this case liquid toluene) that exhibits no charge excitation (due to a large HOMO-LUMO gap) and no surface Raman enhancements (liquid phase with no Ag) were performed at the same conditions as the SERS experiments of this dissertation. This data allowed for the measurement of the ratio of anti-Stokes to Stokes intensities for all the vibrational modes within toluene. These ratios are then compared to the Boltzmann distribution prediction for each mode to determine the necessary correction factor due to the CCD. From the discrete data, an equation is empirically derived such that the correction for any vibrational mode within the measurement range can be calculated.

3.4.2 Non-charge transfer SERS method for correcting unequal EM enhancement

Correcting for the unequal electromagnetic enhancement of anti-Stokes and Stokes photons emitted from the sample is accomplished by using a probe molecule (Rhodamine 6G, R6G) that has been shown previously to not undergo charge-transfer SERS at 785nm on Ag SERS platforms.[11] In these studies, it was shown that while the R6G exhibited higher anti-Stokes to Stokes ratios than the Boltzmann distribution would predict (even with detector correction as described in *Section 3.4.1*), the molecule did not exhibit the other key signatures of charge transfer in the SERS experiments.[10] Because, as mentioned earlier, the electromagnetic SERS enhancement mechanism is dependent on

the electromagnetic properties of the plasmonic nanoparticle substrate but not the nanoparticle-adsorbate interaction, putting R6G on the same Ag nanoparticle SERS platforms used for MB experiments provides a baseline anti-Stokes to Stokes ratio. This ratio, dependent on vibrational mode energy, represents the expected anti-Stokes/Stokes ratio for a thermally equilibrated molecule (*i.e.*, one whose vibrational mode energies obey the Boltzmann distribution) located specifically on the Ag nanoparticle SERS substrate used for later charge transfer experiments.

3.5 Determination of the correction factor from toluene and Ag-R6G samples

Data in Figure 3-1 show the full anti-Stokes and Stokes spectrum of liquid toluene measured using the 785 nm Raman laser. As expected, the Stokes signal is stronger than the anti-Stokes, with relative strength of anti-Stokes signal decreasing with increasing (negative) wavenumber as the Boltzmann distribution predicts. Each large Stokes peak is accompanied by a measureable anti-Stokes peak, the combination of which is used to calculate the experimental anti-Stokes to Stokes ratio.

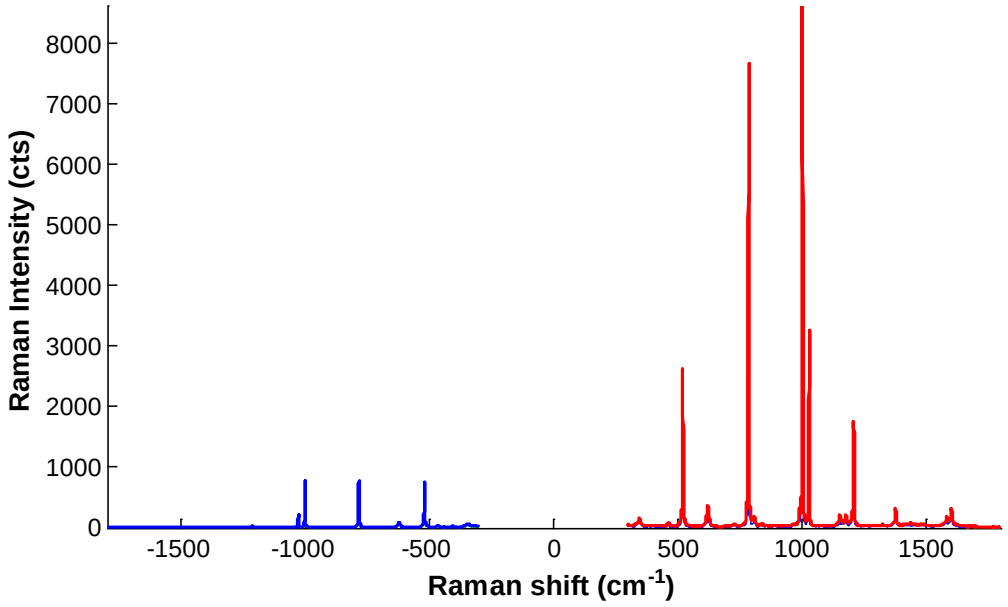

Figure 3-1: Full Raman spectrum of liquid toluene. The anti-Stokes and Stokes spectrum of liquid toluene measured with the 785 nm laser. Though the peaks are too small to see in the figure, measurable anti-Stokes signal exists out beyond -1200 cm^{-1}.

Data in Figure 3-2 show the comparison between measured anti-Stokes and Stokes ratios for vibrational modes in toluene and the expected ratios from a Boltzmann distribution. The measured anti-Stokes/Stokes ratio for toluene is consistently higher than the Boltzmann prediction for a given vibrational mode. While the toluene anti-Stokes to Stokes intensity ratio still follows an exponential decay with respect to the energy of vibrational modes, it is less rapid than the predicted Boltzmann decay. The reasons for the differences in the measured anti-Stokes to Stokes intensity ratios compared to the ratio predicted by Boltzmann distribution is the different sensitivity of CCD to photons of various energies (*i.e.*, Stokes and anti-Stokes photons) described in *Section 3.3.1*. This calibration procedure allows for the correction of CCD detection sensitivity on measurements through the use of a correction factor K_{CCD}, obtained by dividing the

measured toluene anti-Stokes/Stokes ratio at a given Raman shift by the predicted Boltzmann ratio.

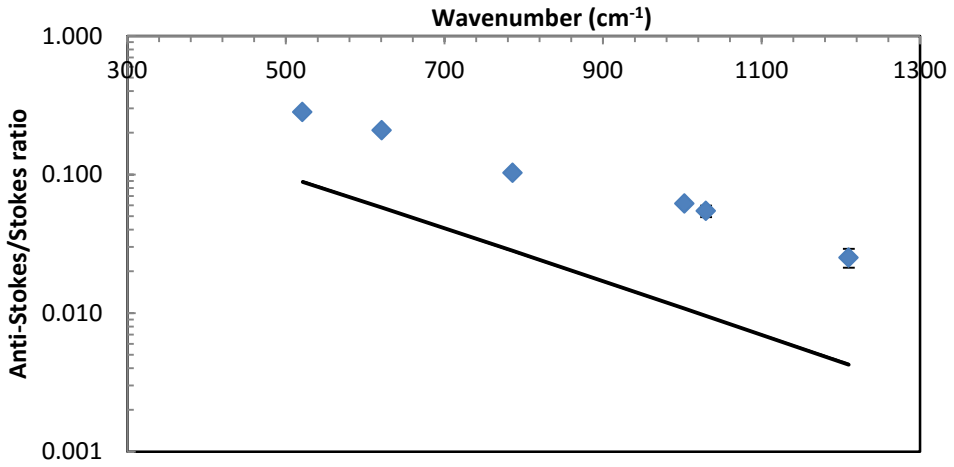

Figure 3-2: anti-Stokes/Stokes ratios of liquid toluene. Measured anti-Stokes to Stokes Raman intensity ratios for liquid toluene (blue diamonds) measured using the 785nm laser, showing deviation from the ratio predicted by the Boltzmann distribution (black line). Error bars represent the standard deviation of the ratios from all experimental collections.

Data in Figure 3-3 show the Raman spectrum for the Ag-R6G system taken with the 785nm laser. From the data, the height of individual peaks and thus the ratio of anti-Stokes/Stokes signal intensities for a given peak are measured.

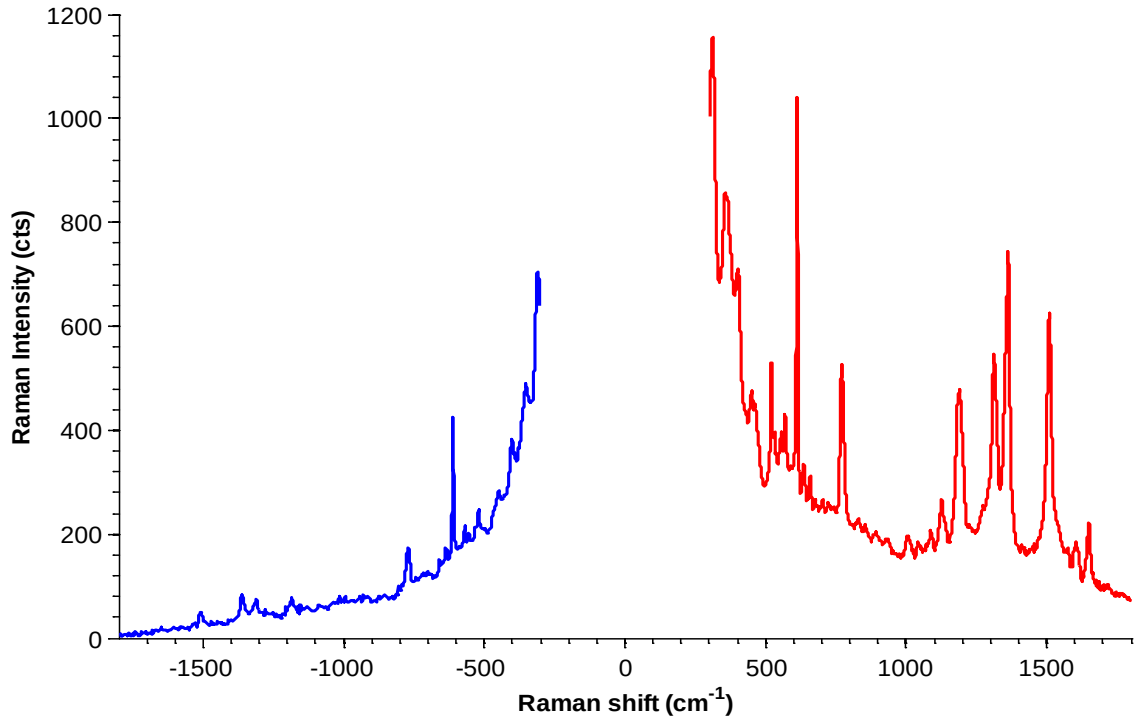

Figure 3-3: Raman spectrum of Rhodamine 6G on Ag nanocubes under the 785 nm laser. Anti-Stokes and Stokes spectrum of Rhodamine 6G on Ag nanocubes collected using the 785nm laser.

In this Ag-R6G system the observed variations in the anti-Stokes/Stokes ratios, as a function of wavenumber, from the Boltzmann distribution come from a combination of the CCD sensitivity (discussed previously) and wavelength dependent electromagnetic enhancement. Here the correction factor is defined, K_{total}, and it quantifies the deviation of the anti-Stokes to Stokes ratio from the Boltzmann distribution:[9]

$$K_{total}(\nu_m) = \frac{I_{aS}^{SERS}(\nu_m)/I_{St}^{SERS}(\nu_m)}{e^{-h\nu_m/k_BT}} \qquad (3\text{-}2)$$

where I_{aS} / I_{St} is the anti-Stokes to Stokes signal intensity ratio for a given Raman shift (ν_m) measured in a SERS experiment while the denominator is the expected ratio based on the Boltzmann distribution, calculated at the experimental temperature of 298K.

Data in Table 3-1 show the average values and standard deviations of K_{total} for specific Raman shifts in the Ag-R6G spectra collected with the 785nm laser. The values for K_{total} are further broken down into their components, K_{CCD} and K_{EM}, to show the relative contribution of each above-described factor. The combination of the CCD sensitivity and wavelength-dependent electromagnetic enhancement yields relatively high values of K, especially at higher wavenumbers. It should be noted that in other studies, additional molecules other than R6G which exhibit no resonant charge transfer were measured using this same procedure and calculated similar values for K_{EM} and K_{total}.[11] From this we can be certain that any dye molecule, including MB, placed on our SERS substrate will experience the same wavelength dependent electromagnetic SERS enhancement.

Raman Peak (cm^{-1})	K_{CCD}	K_{EM}	K_{total}	Std. Dev
612	3.2	1.2	3.8	0.4
772	3.7	1.8	6.5	1.4
1313	5.6	2.1	11.6	3.7
1361	5.7	2.7	15.3	1.9
1509	6.2	3.4	21.4	4.4

Table 3-1: Calculated correction factor (K) at prominent R6G Raman peaks. Values for the correction factor, K, at given Raman shifts corresponding to the prominent peaks in the Ag-R6G Raman spectrum. The K values are broken down into individual corrections for the CCD sensitivity (K_{CCD}) and wavelength dependent electromagnetic enhancement (K_{EM}), with $K_{total} = K_{CCD} * K_{EM}$.

Fitting the values of K_{total} *versus* Raman shift empirically fits an exponential decay and yields Equation 3-3:

$$K_{total}(\nu_m) = 1.49 * e^{0.0017*\nu_m} \quad (3\text{-}3)$$

where ν_m is the Raman shift in cm^{-1}. Any value for an anti-Stokes signal at a given Raman shift can now be "corrected" for the two factors discussed above to give a value for the anti-Stokes/Stokes ratio that accurately represents the vibrational population distribution. Dividing the measured anti-Stokes signal by $K_{total}(\nu_m)$ calculates a corrected anti-Stokes signal that can be used to accurately calculate both nanoparticle electron-phonon and molecular vibrational temperatures. All quantitative values gathered using the 785nm laser reported later in this dissertation were subjected to this numerical correction when appropriate.

While all correction factor calculations carried out thus far apply only to the 785 nm laser, it should be noted that a smaller correction factor also needs to be applied to data taken with the 532 nm laser. Calculating this correction factor was done using the same method described in detail above using the 532 nm laser instead of 785 nm. The data from Raman spectra of toluene show that the correction attributed to CCD is negligible near 532 nm. This is not surprising since 532 nm lies very near the center of the calibrated range of the CCD and thus the wavelengths surrounding it are not subject to measurable changes in sensitivity. There is however a contribution to the correction at 532 nm from the second factor, the wavelength-dependent electromagnetic enhancements of Raman Stokes and anti-Stokes shifted photons on SERS substrates.

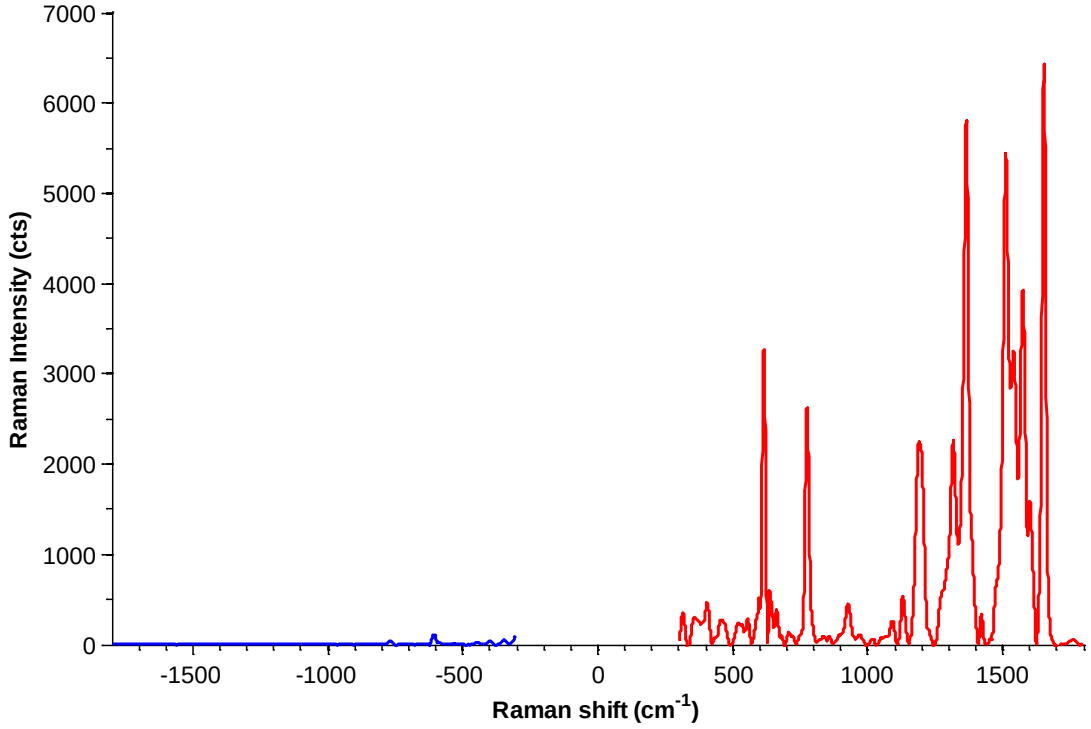

Figure 3-4: Raman spectrum of R6G on Ag nanocubes under the 532nm laser. Anti-Stokes and Stokes spectrum of Rhodamine 6G on Ag nanocubes collected using the 532nm laser.

Data in Figure 3-4 show the anti-Stokes and Stokes spectrum for the Ag-R6G system taken using the 532 nm laser. It is clearly seen that measurable anti-Stokes peaks only extend out to 800 cm^{-1}. Rather than attempt to fit empirically a correction factor as a function of wavenumber for the entire spectrum, values of K_{total} were instead calculated for peaks within this small range (400-800cm^{-1}) and found K_{total} to be approximately constant with a value of 0.68 ±0.03 for all peaks. In the case of 532 nm, opposite that of 785 nm, the anti-Stokes photons are less enhanced by the electromagnetic field than the Stokes photons and anti-Stokes values must be shifted upwards to reflect the true vibrational population of adsorbed molecules being measured. This correction value of

0.68 was applied to all anti-Stokes peak data gathered using the 532 nm laser and presented in this dissertation.

3.6 Conclusions and outlook

The major works presented in this dissertation rely on accurate quantitative analysis of anti-Stokes to Stokes Raman signal ratios, specifically as they relate to the vibrational mode population distribution in a sample of molecules. This chapter showed that using the anti-Stokes to Stokes ratio as a proxy for the vibrational mode population distribution within a sample of molecules is not as simple as finding the raw data ratio and comparing it to the Boltzmann distribution. Instead, a series of control measurements were performed to establish a baseline for systems in which there is no SERS and no charge transfer. This allowed for accurate measurement of the deviation of the anti-Stokes to Stokes ratio from the Boltzmann distribution as a result of two key factors: CCD error, and unequal SERS enhancements of Stokes and anti-Stokes photons. From these measurements, a correction factor was formulated that can be applied to all anti-Stokes measurements so that the anti-Stokes to Stokes ratio will accurately reflect the vibrational mode population distribution. For systems in which there is resonant charge transfer, the anti-Stokes/Stokes ratio is expected to be significantly higher than the Boltzmann distribution predicts, even after the application of the correction factor, due to significant changes in the vibrational mode population distribution as a result of the charge transfer.

3.7 References

(1) Boerigter, C.; Aslam, U.; Linic, S. Supplementary: Mechanism of Charge Transfer from Plasmonic Nanostructures to Chemically Attached Materials. *ACS Nano* **2016**, *10*, 6108–6115.

(2) Maher, R. C.; Galloway, C. M.; Le Ru, E. C.; Cohen, L. F.; Etchegoin, P. G. Vibrational Pumping in Surface Enhanced Raman Scattering (SERS). *Chem. Soc. Rev.* **2008**, *37*, 965–979.

(3) Itoh, T.; Yoshida, K.; Biju, V.; Kikkawa, Y.; Ishikawa, M.; Ozaki, Y. Second Enhancement in Surface-Enhanced Resonance Raman Scattering Revealed by an Analysis of Anti-Stokes and Stokes Raman Spectra. *Phys. Rev. B* **2007**, *76*, 85405.

(4) Schatz, G. C.; Young, M. A.; Van Duyne, R. P. *Surface-Enhanced Raman Scattering*; Kneipp, K.; Moskovits, M.; Kneipp, H., Eds.; Topics in Applied Physics; Springer Berlin Heidelberg, 2006; Vol. 103.

(5) Marimuthu, A.; Christopher, P.; Linic, S. Design of Plasmonic Platforms for Selective Molecular Sensing Based on Surface-Enhanced Raman Spectroscopy. *J. Phys. Chem. C* **2012**, *116*, 9824–9829.

(6) Hao, E.; Schatz, G. C. Electromagnetic Fields around Silver Nanoparticles and Dimers. *J. Chem. Phys.* **2004**, *120*, 357–366.

(7) Tao, A. R.; Ceperley, D. P.; Sinsermsuksakul, P.; Neureuther, A. R.; Yang, P. Self-Organized Silver Nanoparticles for Three-Dimensional Plasmonic Crystals. *Nano Lett.* **2008**, *8*, 4033–4038.

(8) Moskovits, M. Persistent Misconceptions Regarding SERS. *Phys. Chem. Chem. Phys.* **2013**, *15*, 5301–5311.

(9) Kneipp, K.; Wang, Y.; Kneipp, H.; Itzkan, I.; Dasari, R.; Feld, M. Population Pumping of Excited Vibrational States by Spontaneous Surface-Enhanced Raman Scattering. *Phys. Rev. Lett.* **1996**, *76*, 2444–2447.

(10) Haslett, T. L.; Tay, L.; Moskovits, M. Can Surface-Enhanced Raman Scattering Serve as a Channel for Strong Optical Pumping? *J. Chem. Phys.* **2000**, *113*, 1641.

(11) Boerigter, C.; Campana, R.; Morabito, M.; Linic, S. Evidence and Implications of Direct Charge Excitation as the Dominant Mechanism in Plasmon-Mediated Photocatalysis. *Nat. Commun.* **2016**, *7*, 10545.

Chapter 4

Evidence and Implications of Direct Charge Excitation as the Dominant Mechanism in Plasmon-mediated Photocatalysis

4.1 Summary

Plasmonic metal nanoparticles enhance chemical reactions on their surface when illuminated with light of particular frequencies. It has been shown these processes are driven by excitation of localized surface plasmon resonance (LSPR). The interaction of LSPR with adsorbate orbitals can lead to the injection of energized charge carriers into the adsorbate, which can result in chemical transformations. The mechanism of the charge injection process (and role of LSPR) is not well understood. In this chapter, we shed light on the specifics of this mechanism by coupling optical characterization methods, mainly wavelength-dependent Stokes and anti-Stokes SERS, with kinetic analysis of photocatalytic reactions in an Ag nanocube-methylene blue plasmonic system. We propose that localized LSPR-induced electric fields result in a direct charge transfer within the molecule-adsorbate system. These observations provide a foundation for the development of plasmonic catalysts which can selectively activate targeted chemical

bonds, since the mechanism allows for tuning plasmonic nanomaterials in such a way that illumination can selectively enhance desired chemical pathways.

4.2 Introduction

Numerous studies have shown that plasmonic metal nanoparticles can drive photochemical reactions directly on the surface of the nanoparticles when illuminated with relatively low intensity light of particular frequencies.[1–4] It has been proposed that these processes are driven by the excitation of localized surface plasmon resonance (LSPR) on the metal nanoparticles.[4,5] LSPR is the resonant collective oscillation of valence electrons, established when the frequency of an incident electromagnetic field matches the natural frequency of surface electrons oscillating against the restoring force of positive nuclei.[6] It has been proposed that the interaction of LSPR with energetically accessible adsorbate orbitals can yield a charge injection process, where the energized charge carriers (electrons or holes) transiently populate otherwise unpopulated electronic states (orbitals), centered on the adsorbate molecule.[7–9] In this process, the adsorbate (more specifically, the entire adsorbate-nanoparticle system) is moved to a different potential energy surface and forces are induced on atoms in the adsorbate. These forces lead to nuclear motion of atoms in the adsorbate, which can result in the activation of chemical bonds and chemical transformations.[10] This mechanism of charge-driven chemical transformations is known by its original name “desorption (reaction) induced by electronic transitions (DIET)”.

The mechanism of the charge injection process on excited plasmonic metal nanoparticles and the role of LSPR in the process are not well understood. The

illustration in Figure 4-1 outlines the two potential microscopic mechanisms by which charge injection can occur: indirect and direct. The indirect mechanism assumes that charge carriers are excited from occupied states to higher-energy unoccupied states within the metal nanoparticle yielding an excited electron distribution. Subsequently, charge carriers of appropriate energy from this distribution can scatter through the adsorbate states (orbitals) forming transiently charged adsorbates. The role of LSPR in this process is to increase the rates of charge excitation, and the energetic electron distribution associated with this mechanism is very similar to the one obtained if a high intensity laser was illuminated on an extended metal structure. On the other hand, the direct transfer mechanism assumes the direct LSPR-induced electron excitation from occupied to unoccupied orbitals of the molecule-nanoparticle complex (*i.e.*, the excitation process) is not mediated by the formation of an excited electron distribution within the metal nanoparticle. Instead, the decay of an oscillating surface plasmon results in the excitation of an electron directly into an unoccupied adsorbate orbital of matching energy. The direct and indirect charge excitation processes as well as nanoparticle heating due to photon absorption can all theoretically result in photo-chemistry, and it is not clear which of these processes is dominant.[11]

The identification of the dominant mechanism of charge excitation and the impact of LSPR is highly consequential in answering the question whether plasmonic nanostructures can be tuned in a way that under illumination they selectively enhance particular chemical pathways, while suppressing other chemical pathways. As illustrated in Figure 4-1b, if indirect charge transfer plays the dominant role then the steady state concentration of energetic electrons is the highest close to the Fermi level (*i.e.*, similar to

Fermi-Dirac electron distribution) and therefore the electron-driven chemical transformation would preferentially proceed through the adsorbate orbitals closest to the Fermi level. This mechanism does not offer much opportunity to tune the chemical pathways by tuning the plasmonic properties of nanostructures since LSPR would only enhance the rates of electron excitation without impacting the electron distribution. On the other hand, the direct mechanism assumes that the LSPR-mediated photon absorption occurs through the creation of electron-hole pairs of specific energy that are localized on the adsorbate as illustrated in Figure 4-1a. The direct mechanism offers an opportunity to affect chemical selectivity by creating plasmonic nanostructures with the LSPR characteristics that enhance the rates of targeted electronic transitions and therefore the rates of chemical transformations that proceed through only those specific transitions.

In this chapter, the underlying physical mechanisms involved in the LSPR-induced charge transfer and chemical transformations on optically excited plasmonic metal nanoparticles are illuminated. To accomplish this, we have coupled optical characterization methods, mainly wavelength-dependent Stokes and anti-Stokes surface enhanced Raman spectroscopy (SERS) of probe molecules chemisorbed on plasmonic Ag nanostructures, with the kinetic analysis of the rates of photo-catalytic reactions of these molecules in otherwise inert environment. We demonstrate that on optically excited plasmonic nanoparticles, the direct charge transfer mechanism plays an important role and that it results in accelerated rates of chemical decomposition (or desorption) of a

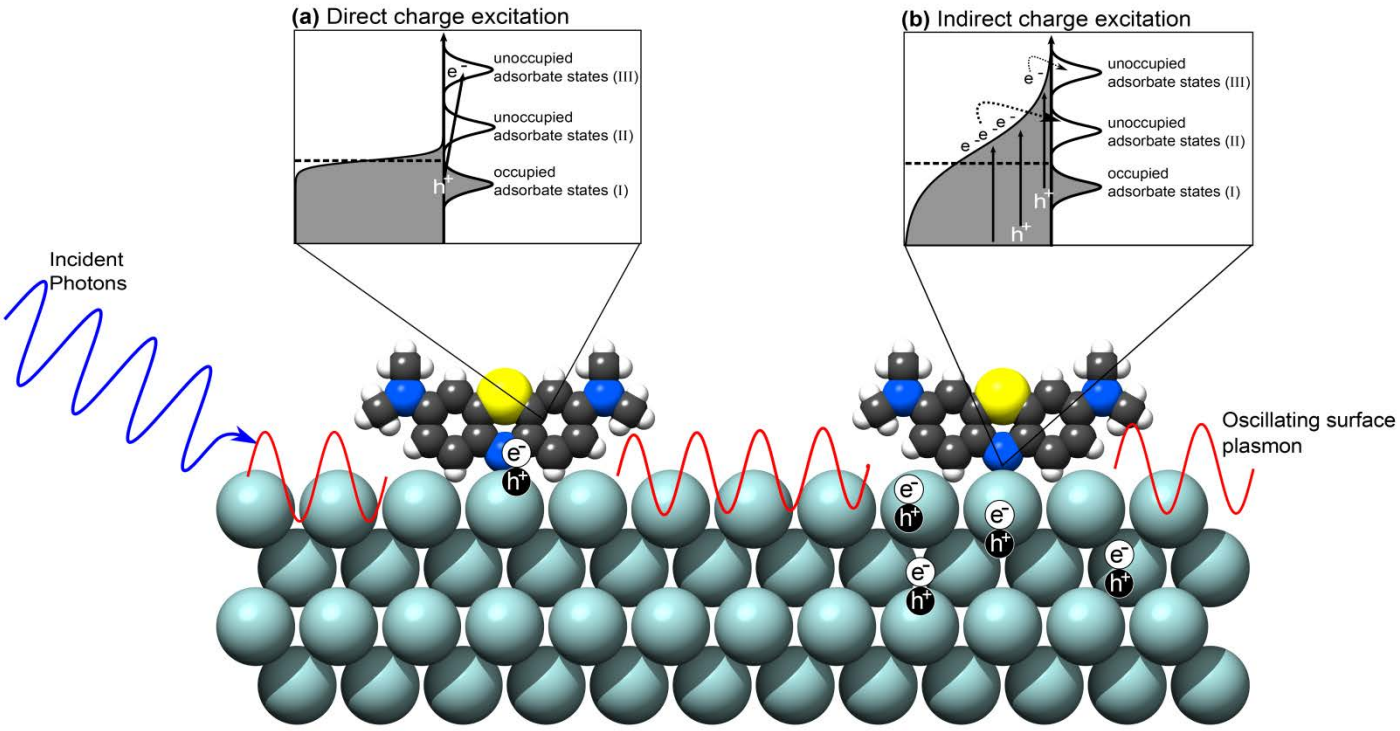

Figure 4-1: Illustration of LSPR-mediated charge excitation mechanisms. Incident photons excite oscillating surface plasmons on an adsorbate-covered Ag nanoparticle surface. These surface plasmon oscillations decay through the formation of energetic electron-hole pairs. In the direct process (inset (a)), the electron is excited directly into an unoccupied orbital of matching energy within the adsorbate. In the indirect process (inset (b)), the energetic electrons formed by decaying plasmons form a distribution within the metal nanoparticle. Electrons with proper energy can then scatter into available adsorbate orbitals. Because of the nature of the electron distribution formed in the indirect mechanism, more electrons will scatter into lower energy orbitals (II) and chemical transformation will preferentially proceed through that lower energy activated pathway. In the direct mechanism however, the electrons can potentially excite into higher energy orbitals (III) when that energy matches the incident photon energy. This opens the possibility for selective chemical pathway targeting that is impossible in the indirect mechanism.

probe molecule in an inert atmosphere. We propose that strong localized LSPR-induced electric fields result in photon absorption through the direct excitation of an electron from specific occupied to unoccupied orbitals of the molecule-nanoparticle complex (*i.e.*, at the surface of the nanoparticle). This can induce photo-chemical transformation of the chemisorbed molecules via a DIET mechanism described above.[7] We also discuss the potential impact of these findings and suggest ways to develop plasmonic catalysts that can potentially selectively activate targeted chemical bonds.

It is important to put our results in the context of numerous previous SERS studies of probe molecules on plasmonic nanoparticles. These previous studies have given us a wealth of information about various mechanisms and consequences of surface enhancement in Raman spectroscopy, even demonstrating that laser induced electron-driven reactions on plasmonic metals are possible.[9,12,13] The results presented herein build upon these findings by focusing on the missing link between LSPR and charge excitation. We distinguish between the above-discussed two LSPR-mediated mechanisms of charge excitation by analyzing the unique anti-Stokes spectral behavior that is interpreted in terms of LSPR-mediated vibro-electronic excitation.

4.3 Experimental and theoretical Methods

4.3.1 Ag particle synthesis, sample preparation, and SERS studies

The plasmonic nanoparticles in these Raman studies were silver nanocubes, synthesized via the modified polyol method.[14] All aspects of this synthesis are described in detail in Chapter 2, *Section 2.3.1*. Synthesized cube samples were characterized by STEM imaging and found to have an average size of 71 ± 9nm. Figure 4-2 shows an STEM image of a nanocube sample, giving evidence of their uniform size and shape.

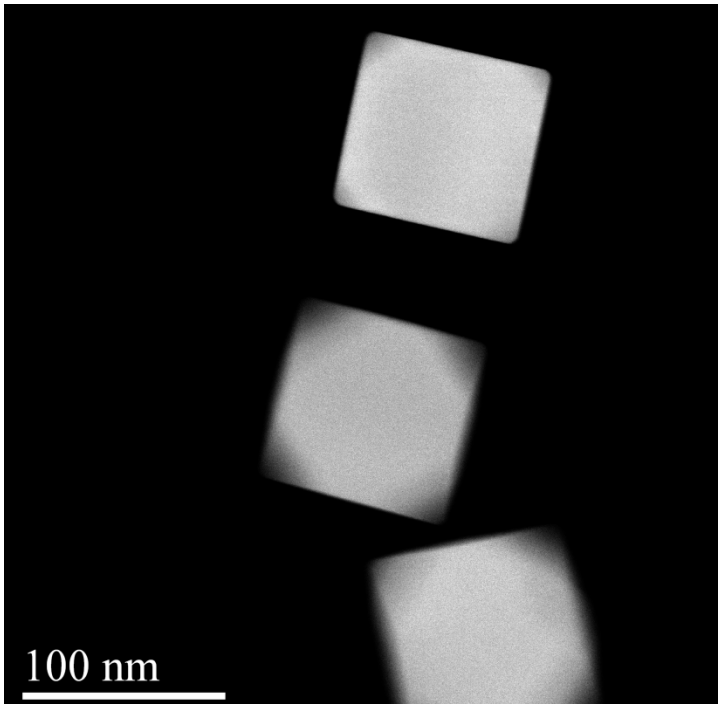

Figure 4-2: STEM image of Ag nanocubes. STEM image of Ag nanocubes demonstrating the cube shape and size uniformity among the synthesized sample. The Ag nanocubes measured 71 ± 9 nm in edge length.

Methylene blue (MB), Rhodamine 6G (R6G), and Acridine Orange (AO) were used as probe molecules in model systems. After synthesis, the cubes were washed 5x by centrifugation and re-dispersion in a combination of acetone and ethanol. After washing, the cubes were dispersed in ethanol and small amount of NaCl was added to aid

aggregation of Ag nanoparticles during the drying process. One of the dye molecules was added to the liquid solution at a concentration of 40μM and allowed to incubate for several hours to ensure full equilibrium adsorption of the dye onto the silver surface.[15] Adding the dyes while the particles are still in liquid solution allows the molecules to access all available adsorption sites on the Ag particles. Solid samples for spectroscopic studies were prepared by drop coating the solution onto a glass or silicon chip and allowing the ethanol solvent to evaporate, leaving behind a thin layer of silver-dye aggregates. UV-vis spectra were gathered using samples on glass slides and a Thermo Evolution 300 spectrometer. Stokes and anti-Stokes Raman spectra were gathered using a Horiba LabRAM HR system under excitation from either a 532nm diode-pumped solid state laser, or a 785nm diode laser. The acquisition time for the spectra was 2 seconds to negate heating effects due to prolonged laser exposure. In solid samples, the laser was focused on nanoparticle aggregates visible through a 50x microscope lens.

4.3.2 Wavelength-dependent photo-catalytic degradation of methylene blue

Photo-reaction studies were conducted in a temperature-controlled Harrick Praying Mantis reaction chamber designed for Raman spectroscopy. A sample of MB on silver on a silicon chip was placed inside the chamber, with the transparent reactor window allowing Raman spectra to continue to be collected. The temperature of the sample within the reactor could then be controlled, and pure nitrogen could be flowed through the reactor to provide an inert atmosphere. Samples in MB degradation studies were heated to 373K under N_2 atmosphere and subsequently exposed to one of two lasers (532nm or 785nm, at equal photon flux) or no light (control) for a measured period of time. Losses in Raman peak signal for prominent bands in MB were measured and

interpreted as decreases in surface coverage of MB due to chemical change (decomposition or desorption).

4.3.3 Finite-difference time-domain (FDTD) simulations

Finite-difference time-domain (FDTD) simulations were carried out using the Meep simulation package.[16] The simulations were performed in a three-dimensional grid measuring 294 nm x 294 nm x 294 nm. An additional 50 nm of perfectly matched layer was added to all sides of this grid. The space between grid points was 1 nm for all but one simulation in which the much more computationally expensive 0.5nm mesh was used to ensure that a shrinking mesh size did not change significantly the behavior of the field intensities within gaps between particles. The dielectric function for silver was obtained from data published by Rakic et al.[17] Nanocube dimers were arranged in a number of orientations, including face-to-face, face-to-edge, edge-to-edge, and corner-to-corner; each dimer system was tested with inter-particle separations of both 1nm and 2nm. Additionally, Ag nanocube trimers were also simulated in edge-face-edge and edge-edge-edge orientations with 1nm separations. The source wavelengths studied matched those of the laser in the Raman setup, 532nm and 785nm. The energy from the source propagated perpendicular to the interparticle axis; the polarization of the source was alternately perpendicular and parallel to the interparticle axis in separate simulations. Field enhancement data was visualized on the x-y and x-z planes. Integrated field values were calculated by finding the average value of the electric field data points located on the nanoparticle surfaces only.

4.3.4 Density functional theory (DFT) calculations

Density Functional Theory (DFT) calculations were performed using real space grid-based projector augmented wavefunction DFT implemented in the GPAW software package.[18] The exchange-correlation interaction was approximated using the revised Perdew-Burke-Ernzerhof (RPBE) functional.[19,20] The Ag[100] and Ag[211] surfaces were modeled using 3 x 3 slabs and 2 x 3 slabs, respectively. All systems used 4-layer slabs, with 10 Å of vacuum space. Pyridine molecules were adsorbed vertically over a top site [100] or above a step site [211] to match the predominant facets present in the synthesized Ag nanocubes. Multiple adsorption configurations were tested for the molecules on the Ag surfaces.

4.4 Results

4.4.1 Optical properties of the Ag nanocube SERS platform

The SERS platforms (*i.e.*, the model system) used in our studies contained small aggregate clusters of silver (Ag) nanocubes with the cube length of ~ 75 nm dispersed on a silicon substrate as shown in the optical micrograph in the inset of Figure 4-3. We performed SERS measurements of probe molecules using two different lasers with the wavelengths of 532 and 785 nm. The optical excitation of LSPR at these wavelengths results in high intensity electric fields at the surface of the Ag nanoparticles. Since these local fields facilitate the photo-physical and photo-chemical processes studied herein, we first employed classical FDTD electro-dynamics simulations to compute the local near field electric field intensities of Ag systems that modelled our SERS platform. These

simulations serve to provide part of the framework with which to interpret the key Raman results in this study.

In our FDTD studies we used model systems consisting of two and three Ag nanocubes positioned at different configurations at 1 and 2 nm separations from each other. Not surprisingly, the FDTD simulations show that the highest plasmonic electric field intensities are generated in the gaps between the nanoparticles (see Figure 4-3). We find that for both laser source wavelengths, the field intensity enhancements in the 1 nm gap between the two nanoparticles are similar to each other ($(|\mathbf{E}|/|\mathbf{E_0}|)^2 \sim 4 \times 10^4$). Furthermore, we have also integrated the field intensity enhancement across the entire surface of the two nanoparticle system to obtain the average surface field intensity enhancements (see Table 4-1). We find that the average field intensity enhancements are within an order of magnitude of each other for the 532 and 785 nm sources. Similar analysis for the Ag nanoparticles separated by 2 nm from each other as well as for the systems containing aggregates of three Ag nanoparticles, showed very similar results.

	Face-Edge Dimer		Edge-Edge Dimer	
Source	separation 1 nm	separation 2 nm	separation 1 nm	separation 2 nm
532 nm	153.92	600.78	172.43	787.61
785 nm	23.56	87.99	27.2	199.63
	Edge-Edge-Edge Trimer		Edge-Face-Edge Trimer	
Source	separation 1 nm		separation 1 nm	
532 nm	220.68		470.26	
785 nm	740.69		313.65	

Table 4-1: Average simulated field intensities around nanoparticle aggregates. Integrated average values of ($|E|^2/|E_0|^2$) for dimers and trimers of silver nanocubes (side length 75 nm) in various orientations, at inter-particle separations of 1 nm and 2 nm, under source wavelengths 532 nm and 785 nm. The values in this table are the average of the integrated field intensity at points located on the nanoparticle surfaces in each system. For each geometry and separation combination, the average enhancements under 532 nm and 785 nm were within an order of magnitude of each other.

It should be noted that the geometries simulated in the FDTD studies are idealized representations of our SERS platforms, which in practice contain aggregates of multiple nanoparticles with varying orientations and separation distances. The effect of particle orientations and separation distances on the optical properties of collections of plasmonic nanoparticles has been studied extensively previously. These studies showed that the resonant wavelength of the coupled dimer plasmon resonance peak is dependent on the particle separation, moving to longer wavelengths and higher maximum field intensities for smaller separations.[21,22] Therefore, due to the random nature of the Ag nanoparticle clustering in our system, we expect that there are different spots that support plasmon resonance peaks over a broad range of wavelengths. The data in Figure 4-3a, which show the UV-vis extinction spectrum of a sample of silver nanocube aggregates used in the SERS studies, show this precise signature with a very broad extinction peak ranging between 600-900nm and beyond. The slightly stronger and more confined extinction peak ranging from 450-550nm is the result of dipolar LSPR within single particles, while still higher energy peaks come from higher order multi-pole resonances within individual particles.[23,24] The wavelengths of the Raman lasers used in our studies are overlaid on the spectrum.

It is worth noting that in addition to the above described photo-physical properties, which can be captured by classical electrodynamics, there have been reports of quantum charge tunneling between optically excited plasmonic nanoparticles.[25,26] This charge tunneling process has been reported for the particle separations smaller than ~ 0.3 - 0.5 nm.[27–29] It is a consequence of very large electric fields confined in the nanogaps

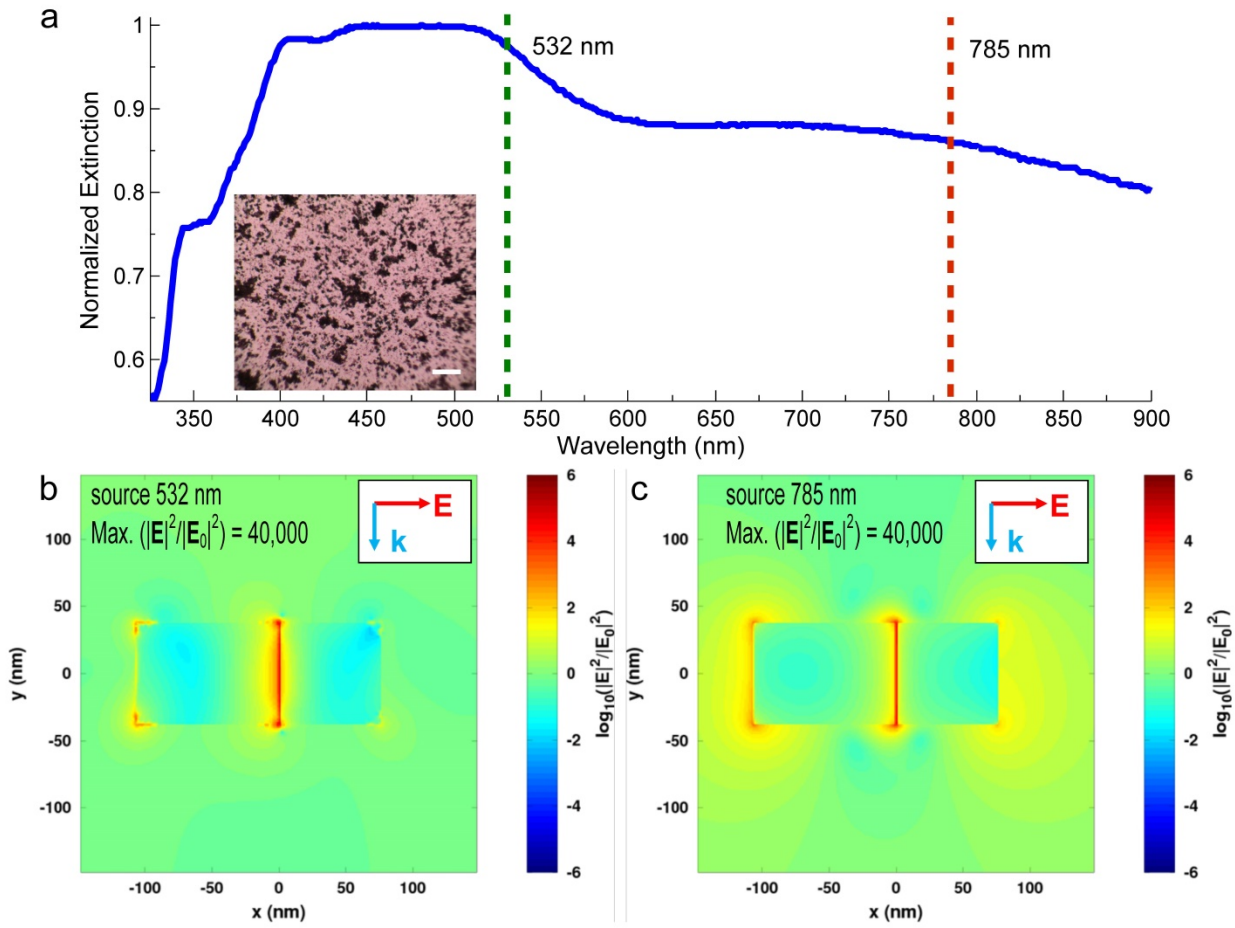

Figure 4-3: Optical characterization of Ag SERS platform. (a) UV-vis spectrum of silver nanocubes after deposition onto solid substrate. The two dashed lines show the wavelengths of the lasers used in this study and their overlap with the LSPR of the silver cubes (inset: optical micrograph of Ag-MB sample showing high levels of aggregation, the scale bar is 20μm). (b),(c) Simulated spatial distribution of electric field enhancement for a silver nanocube dimer (face-to-edge orientation) with separation distance of 1nm under (b) 532nm and (c) 785nm photon excitation.

which force the movement of charge between the particles. At these extremely small gap distances the tunneling process broadens and slightly blue-shifts the LSPR resonance peaks while decreasing the maximum field intensity from the classical prediction.

To summarize, our analysis of the photo-physical properties of the SERS platforms suggests that: (i) there are sites in our system that can support LSPR with significantly elevated electric field intensities at both Raman laser wavelengths, (ii) while we know the field intensities are significantly elevated, we cannot know the exact intensity at each site due to the disordered nature of Ag aggregates in our SERS platforms, and (iii) potential quantum tunneling could be taking place in aggregates with interparticle gaps of 0.5nm or less. With regard to the final two points, our analysis of Raman results and the conclusions drawn are not affected by the lack of exact knowledge of field intensities at every site in the system. By focusing our analysis on the ratios of anti-Stokes to Stokes signals in a given measurement and probing the dependence of only these ratios on the incident photon intensity, we find the exact value of the electric field intensity to be irrelevant so long as it is strong enough to support SERS.

4.4.2 SERS measurements for methylene blue on Ag

There have been a few studies of the chemisorption of methylene blue (MB) and similar molecules on Ag surfaces.[30–32] It has been suggested that MB chemisorbs through a covalent chemical bond between an Ag surface atom and the nitrogen atom in the aromatic ring of MB. We have also performed Density Functional Theory (DFT) quantum calculations of adsorbed thiazine on Ag model slabs. We use thiazine as a surrogate for MB since similar to MB, thiazine has an N- and S-containing aromatic ring and similar bonding conformations are proposed. Thiazine is smaller than MB and

therefore more easily handled computationally. Our DFT calculations, using the RPBE density functional, showed that the binding energy of thiazine to the Ag(100) surface facet is -0.29eV (exothermic) while on the under-coordinated Ag(211) surface the binding energy is -0.37eV. Since the RPBE functional in general underestimates the binding energy and neglects van der Waals forces, we suggest that in our systems MB chemisorbs on the surface sites of Ag nanocubes, essentially coating the nanoparticles.

There are two established potential mechanisms by which LSPR can enhance Raman scattering. One mechanism involves the LSPR-induced enhancement of the local electric field intensity at the adsorbate (electromagnetic mechanism) leading to the enhancement of the Raman signal. The electromagnetic enhancement factor (Σ) of Raman signal depends on electromagnetic field enhancement at the location occupied by a probe molecule. It can be closely approximated by:

$$\Sigma = (|\boldsymbol{E}(\nu_i)|^2 * |\boldsymbol{E}(\nu_i \pm \nu_m)|^2) \qquad (4\text{-}1)$$

where $\mathbf{E}(\nu)$ is the local electromagnetic field enhancement at a photon frequency ν. ν_i and $(\nu_i+\nu_m)$ are the frequencies of the incident (*i.e.,* laser) photon and scattered (*i.e.,* Raman shifted) photon respectively.[33,34] The other mechanism involves the LSPR-induced charge-excitation (or charge-exchange) mechanism.[34] Charge-excitation SERS occurs as a result of the LSPR-mediated charge excitation from filled to unfilled electronic states of the nanoparticle-adsorbate complex (one or both of these electronic states are localized on the adsorbate). The propensity to undergo charge excitation is, among other things, determined by the local electronic structure of the adsorbate-metal complex.[35]

Since we were interested in investigating the LSPR-induced charge excitation process and the chemical consequences of this process, we focused on identifying

systems where these two mechanisms can be separated from each other, centering our studies on the charge excitation mechanism and probing its effect on chemical transformations. Below, we demonstrate that MB on Ag exhibits a LSPR-mediated charge excitation only at specific excitation wavelengths and that this process increases the rates of chemical reactions (in this case the degradation or desorption of MB on the Ag surface). These observations allow us to conclude that in this case LSPR mediates the process of charge excitation into adsorbates via the above-discussed *direct* mechanism.

The process of charge-excitation within the metal-adsorbate complex has some key experimentally distinguishable SERS signatures. These signatures are a consequence of the fact that the charge excitation process results in an elevated population of excited vibrational modes compared to the equilibrated, thermalized system. Therefore, a key signature of the charge transfer process is an elevated anti-Stokes Raman intensities compared to those expected for a thermodynamically equilibrated system. We note that Stokes scattering signal in Raman spectroscopy is the measure of the rate of transitions of a molecule from the ground to the first excited vibrational states, while the anti-Stokes scattering signal measures the reverse process. The ratio of anti-Stokes to Stokes scattering rates (intensity signals) for a vibrational mode can be related to the population of vibrationally excited molecules.[36]

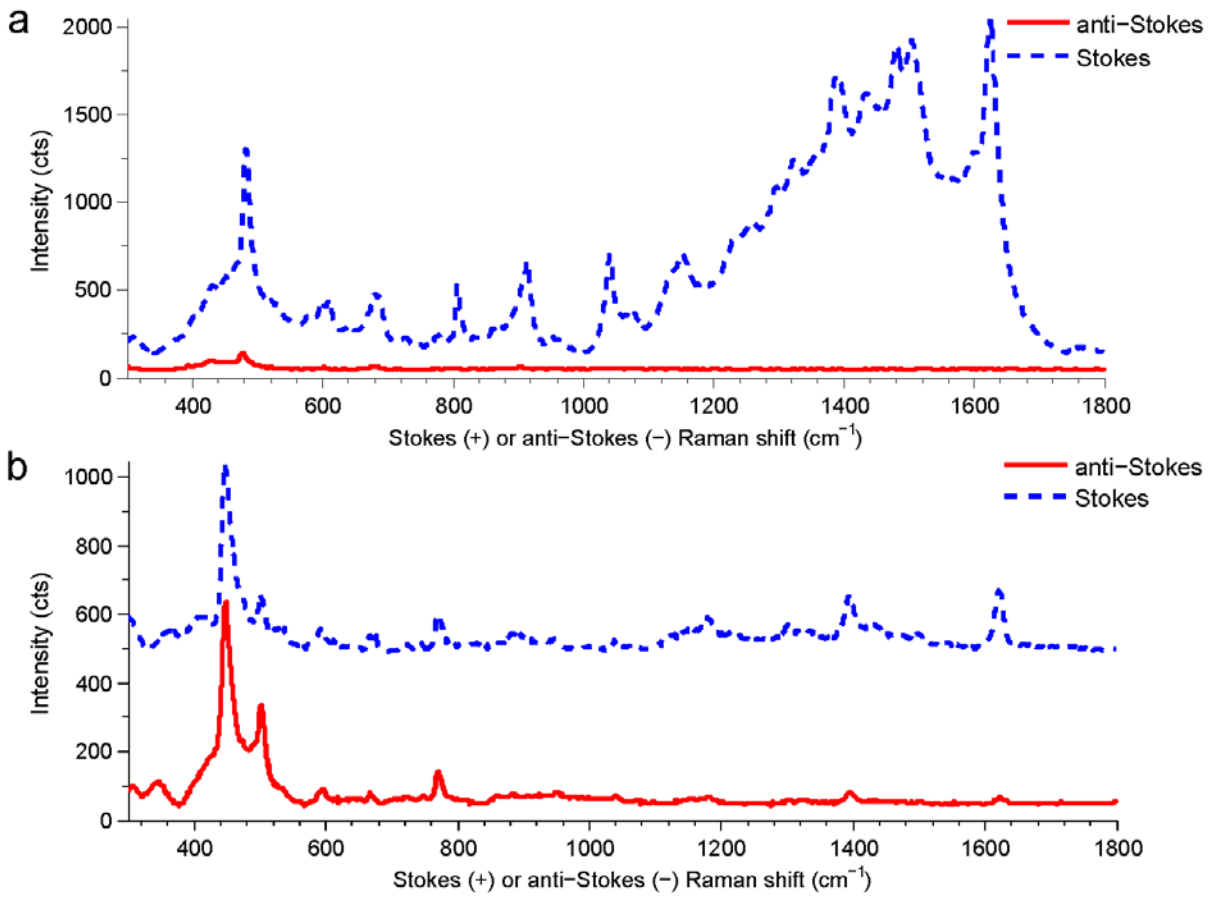

Figure 4-4: SERS spectra of silver nanocube-dye structures. (a), (b) Stokes and anti-Stokes spectra for silver nanocube-methylene blue (Ag-MB) structures gathered using a 532nm (a) or 785nm (b) laser. All experimental parameters other than the wavelength of incoming photons, including incident photon flux, acquisition time, and sample spot size were identical. It should be noted that Stokes shifts have positive wavenumbers (cm^{-1}) while anti-Stokes shifts are negative. They are plotted on the same positive axis here to allow for direct comparison.

Data in Figure 4-4 show Stokes and anti-Stokes SERS spectra for the Ag-MB complex at 532nm (3a) and 785nm (3b) excitation wavelengths. The spectra were collected using the same photon flux of 2.0 * 10^{20} $cm^{-2}s^{-1}$ for both lasers. Visual inspection of the data in Figure 4-4 shows that the ratio of anti-Stokes to Stokes signals at 785 nm is higher than when the 532nm laser source was used. To quantify these observations, the ratio of anti-Stokes/Stokes signal (ρ_{SERS}) for specific MB vibrational

modes (υ_m) of the Ag-MB complex under 785 nm and 532 nm excitations was computed and compared with the ratio for a similar energy mode in liquid toluene (ρ_{tol}). Using toluene as an external standard corrects for any wavelength-dependent biases due to the sensitivity of the CCD detector, as demonstrated previously.[37,38] Liquid toluene gives a basic non-SERS, non-resonant Raman spectrum at visible light excitation, and the anti-Stokes to Stokes intensity ratios in toluene are consistent with those predicted by Boltzmann thermal distribution.[37] The degree by which the SERS anti-Stokes signal exceeded the expectation of the Boltzmann distribution is described through the quantity (K), which was calculated using the following equation:

$$K(\nu_m) = \frac{\rho_{SERS}}{\rho_{tol}}(\nu_m) = \frac{I_{aS}^{SERS}(\nu_m)/I_S^{SERS}(\nu_m)}{I_{aS}^{tol}(\nu_m)/I_S^{tol}(\nu_m)} \qquad (4\text{-}2)$$

where I_{aS}^{SERS} and I_S^{SERS} are the measured anti-Stokes and Stokes intensities, respectively, for MB on Ag at a given vibrational mode energy (ν_m). I_{aS}^{tol} and I_S^{tol} are the anti-Stokes and Stokes intensities, for the similar vibrational mode in toluene.

532nm	
peak (cm^{-1})	K
482	0.63
807	0.60
914	1.24
1041	1.32

785nm	
peak (cm^{-1})	K
447	3.91
771	7.67
1394	27.75
1621	34.45

Table 4-2: K values in Ag-MB spectra. Calculated K values for selected peaks in the MB SERS spectrum excited by 532nm and 785nm lasers.

The data in Table 4-2 show the calculated K values for various modes of the Ag-MB complex at 532nm and 785nm excitation at the photon flux of 2.0 * 10^{20} $cm^{-2}s^{-1}$. The data show that the K values under 785nm excitation range between 4 and 34 for different

Ag-MB modes. On the other hand, the K values for the 532 nm excitation are close to 1. The elevated K values at 785 nm compared to 532 nm suggest that charge excitation might be taking place within the Ag-MB complex at 785 nm and that there is no charge excitation for 532 nm wavelength.

We must note however that the SERS enhancement of Stokes and anti-Stokes scattering, in addition to the vibrational populations, also depends on the field intensity at the frequency of scattered (*i.e.,* Raman shifted) photons as described in eq. (1). Different field intensities at the frequencies of Stokes and anti-Stokes scattered photons can contribute to the elevated K values even without charge transfer.[39,40] To rule out this possibility we have performed SERS studies using the same Ag nanocube SERS platform with other probe molecules (Rhodamine 6G and Acridine Orange) which under 785 nm radiation do not exhibit charge excitation.[38] These studies show that for these molecules the K values at 785 nm are significantly lower than the K values for MB, signaling that the elevated vibrational population observed for the Ag-MB complex at 785 nm is due to the charge excitation process.

Further confirmation of charge excitation taking place at 785 nm comes from observing that the ratio of anti-Stokes to Stokes signal shows a positive dependence on incident photon intensity. This is another key feature of the charge excitation process.[36,41] As discussed above, charge excitation can lead to a non-thermalized population of vibrationally excited molecules (*i.e.,* an elevated population of molecules in the first excited vibrational states, which are the initial states for $\upsilon = 1 \rightarrow 0$ transitions associated with anti-Stokes scattering). As the source intensity increases, probe molecules will have a larger fraction of modes that are excited to the first excited vibrational state and above,

thus increasing the anti-Stokes to Stokes signal ratio.[36,37] This phenomenon is known as optical pumping, and in this regime the theoretically derived ratio (ρ) of anti-Stokes to Stokes signals is governed by the equation:[36]

$$\rho_{SERS} = \frac{I_{aS}^{SERS}(\nu_m)}{I_S^{SERS}(\nu_m)} = \frac{\sigma_{aS}}{\sigma_S}\left[\frac{\tau\sigma_S I_L}{h\nu_L} + e^{-\frac{h\nu_m}{k_B T}}\right] \qquad (4\text{-}3)$$

where σ_{aS} and σ_S represent the cross-section for anti-Stokes and Stokes events respectively, τ the vibrational relaxation time constant for the molecule, I_L the incident light intensity, $h\nu_L$ and $h\nu_m$ the energy of the incident photon and vibrational mode respectively, at T the sample temperature.

The equation covers both the exponential dependence of the population of the excited vibrational states on temperature and the linear dependence on photon intensity (I_L). In the optical pumping regime (*i.e.*, when the linear term in Equation 4-3 is of the same order or greater than the exponential term) under constant sample temperature, ρ_{SERS} and thus K (as described above, the measure of the deviations in the anti-Stokes to Stokes ratios from the ratio predicted by the equilibrium Boltzmann distribution) will show a linear dependence on the photon intensity. The data in figure 4-5 show the K values plotted against incident photon intensity for some of the most prominent bands in the Ag-MB Raman spectrum under 785nm excitation. The intensity spans two orders of magnitude of photon flux, from $1.5*10^{19}$ to $2.0*10^{21}$ cm^{-2} s^{-1}. The data show a linearly increasing K for all modes as photon flux increases, providing compelling evidence that the samples are well within the optical pumping charge excitation regime. This is in contrast to the other measured probe molecules which showed no linear increase in K values with increasing intensity.

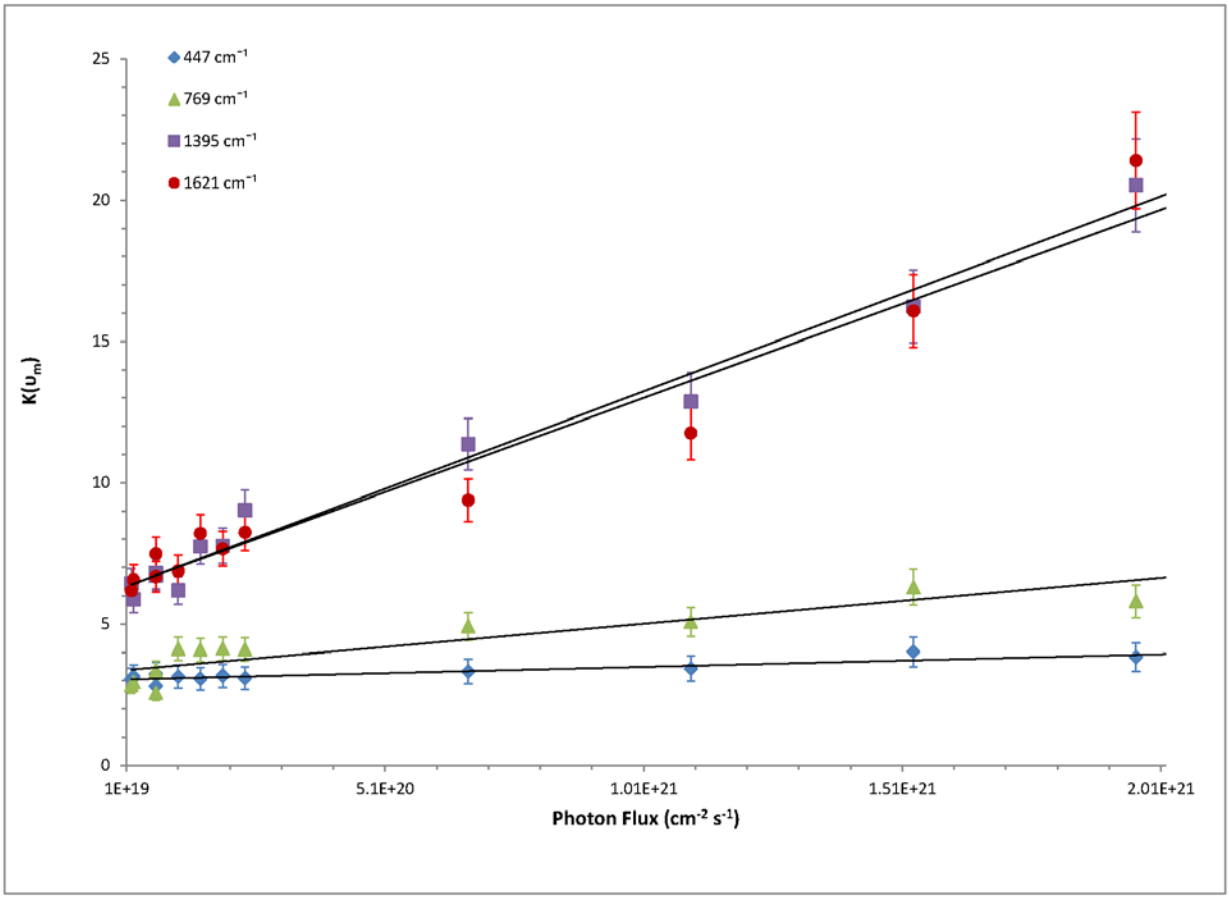

Figure 4-5: Excess anti-Stokes signal as a function of incident photon flux. Excess anti-Stokes signal ratio (K) dependence on the incident photon flux for multiple prominent bands in the methylene blue spectrum gathered using the 785nm excitation wavelength. The linear nature of the dependence is compelling evidence that optical pumping of the MB molecules is occurring. Error bars represent standard deviation of three separate experimentally gathered K values for a given band and photon flux.

4.5 Discussion

The above discussed data represent evidence that Ag-MB complexes experience charge excitation resonance under exposure to 785nm incident photons, while the charge excitation process does not take place with 532 nm laser under identical photon fluxes. It is important to reiterate that these results cannot be explained only by the different values of the field intensities at these two wavelengths. If this was the case, any molecule could exhibit elevated anti-Stokes signals under 785nm illumination. We have ruled out this possibility in the above-mentioned SERS studies of other probe molecules (Rhodamine 6G and Acridine Orange) which under 785 nm illumination do not exhibit charge excitation. Similarly, these studies of other probe molecules also rule out interparticle electron tunneling experienced at very small particle separations as the only requirement for the above mentioned charge transfer process, as if this were the case we would again expect no difference in the results when using other probe molecules.

The data presented above shed light on some microscopic features of the charge excitation process, depicted in Figure 4-1. We have postulated that the charge excitation can take place following an indirect route where excited charge carriers are first formed within the nanoparticle in a process that results in an excited electron distribution. Electrons from this distribution that gain sufficient energy can scatter through the adsorbate states forming transiently charged adsorbates. Conversely, in the direct excitation process, the presence of unoccupied adsorbate orbitals at a specific energy allows for a direct, resonant transition from occupied to unoccupied orbitals of the molecule-nanoparticle complex. We suggest that the occurrence of charge excitation only by photons of specific energy (785 nm) and not by those of higher energy (532 nm) under

identical incident photon intensities shows that the mechanism of charge excitation in this system is direct. If the mechanism were indirect, one could expect to see evidence of charge excitation at any wavelength with photon energies at least as high as the difference between the metal Fermi level and the LUMOs of the adsorbate. Under the assumption of the indirect mechanism, as photon energies increased (e.g. from 785nm to 532nm), the extent of charge excitation would be expected to rise, as the number of electrons within the metal that reached the requisite energy to scatter into the unfilled adsorbate states would increase. Because this does not occur and instead we observe charge excitation only under lower energy photon excitation, we suggest that the process of charge excitation is direct and it involves direct resonant single electron transitions from occupied to unoccupied states of the Ag-MB complex.

The evidence that points toward a direct mechanism of charge excitation also serves to rule out plasmon-induced heating of the nanoparticles as an explanation for the high anti-Stokes data. The K values for the SERS data collected under 532 nm excitation are close to 1, suggesting that there is no significant laser induced heating of the entire system at this excitation wavelength. Equilibrated heating of the system would increase the population of excited vibrational modes of the molecule and result in elevated anti-Stokes intensity and therefore elevated K values. Based on the fact that for identical photon fluxes, the energy dissipated into the system would be higher for the 532 nm laser compared to the 785 laser, we argue that equilibrated heating of the entire sample does not take place for the 785 nm laser either. This suggests that the process of charge excitation observed at 785 nm results in energy being selectively deposited into the adsorbed molecule, rather than into the entire system.

We can also speculate about the nature of the electronic states involved in the charge excitation process. The HOMO-LUMO energy gap in the free MB molecule is ~ 1.86 eV (665nm), which is above the energy of the photons from the 785 nm (1.6eV) laser. An examination of the absorption spectrum of aqueous MB shows no interaction with light near 785nm. This means that the electronic states involved in the charge excitation processes are associated with either strongly perturbed states localized on MB – these perturbations can be due to the chemisorption of MB in the Ag metal – or with hybridized Ag-MB electronic states.

It is also important to discuss how LSPR could affect this process of charge excitation. As discussed above, our data point us in the direction of the direct one-electron excitation by 785nm photons among the states within the Ag-MB complex. Clearly the existence of the electronic states that can be accessed by the 785 nm photon is a requirement for the observed charge excitation process. The SERS data suggest that there are high LSPR-mediated electron transition rates between these states. The high transition rates can only be observed under the following conditions: First, there is a large density of the electronic states corresponding to these transitions. Second, there is a high degree of overlap between the corresponding wave functions of the associated states (giving large oscillator strengths). Third, there must exist a high intensity electric field driving the excitation process (pushing electrons from the occupied to unoccupied states) at the location of the adsorbate. Whether the first and second requirements are fulfilled depends on the local electronic structure of the Ag-MB system, the properties of which are determined by the chemisorption of MB on Ag. We hypothesize that LSPR plays a role in the third requirement, *i.e.*, LSPR is providing high intensity fields, particularly in

the small inter-particle gaps, at frequencies that can support the high rates of the electronic transitions between the states centered on the adsorbate.

This hypothesis that the role of LSPR is somewhat decoupled from the role of the local electronic structure has far reaching consequences in the potential design of selective plasmonic catalytic systems. It suggests that by engineering plasmonic nanomaterials with plasmon resonances that match the charge excitation energies of adsorbates interacting with the plasmonic nanostructure, it is possible to engineer systems that can support higher rates of electronic excitations between electronic states of a particular energy (at particular wavelengths). A natural implication of this hypothesis is that plasmonic nanomaterials can be tuned in such a way that under illumination they will selectively enhance particular chemical pathways (those which are activated by the particular electronic transitions supported by plasmon-induced local fields) while suppressing other chemical pathways. One way to achieve this objective might be to combine plasmonic particles with more active metals in a single catalyst or have bimetallic nanoparticles which combine a plasmonic metal core and a more chemically reactive metal shell.[42,43] In these systems the interaction of the chemically reactive metal with adsorbates allows for tuning of the electronic structure of adsorbates on the nanoparticle (based on the selection of the metal), while the optical properties are governed by the plasmonic metal. By matching these electronic and optical properties it could be possible to induce preferential selective charge transfer to a particular orbital, essentially guiding photochemical transformation toward the more selective pathway.

A direct corollary of the hypothesis that nanomaterials with plasmon resonance wavelengths matching the charge excitation energies of surface adsorbates can accelerate

chemical reactions of the adsorbates at these wavelengths is that MB on Ag should be more reactive under 785nm illumination than under 532nm. To test the corollary we measured the rates of decomposition/desorption of MB on the surface of the Ag nanoparticles illuminated with $2.0*10^{20}$ $cm^{-2}s^{-1}$ photon flux of the 785nm and 532nm light sources, under inert N_2 atmosphere and at constant 100C reactor temperature. Data in Figure 4-6 show the differences in the extent of SERS signal degradation of the most prominent Raman mode in MB ($447cm^{-1}$) over a given period of laser exposure. The data

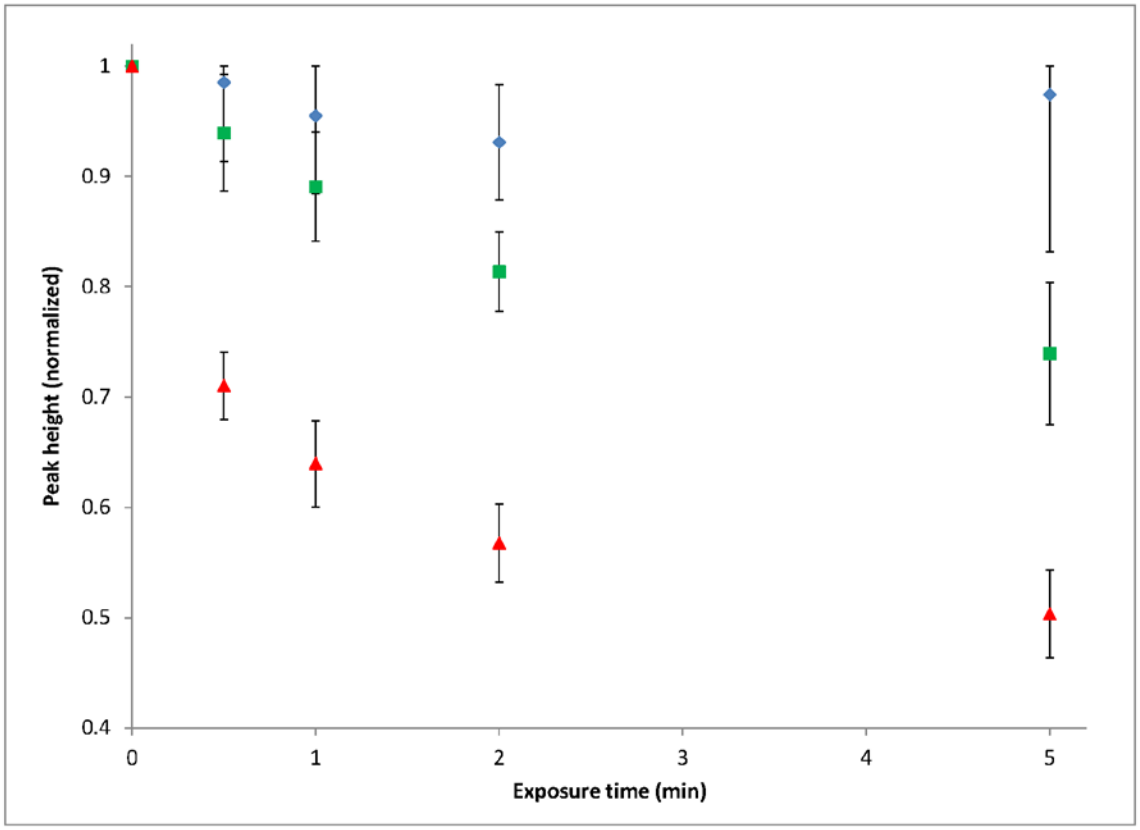

Figure 4-6: Methylene blue signal degradation by prolonged laser exposure. Normalized heights of the $447cm^{-1}$ Raman mode of Ag-MB gathered at 373K and in inert N_2 atmosphere after exposure to no laser (control, blue diamonds), 532nm laser (green squares), or 785nm laser (red triangles) for a given periods of time. The 785nm laser shows significant signal degradation enhancement compared to the 532nm and control samples.

show that under exposure to the 785nm laser, MB signal degradation occurs significantly faster than under exposure to the 532nm laser of identical intensity. The instantaneous rate (rate as time → 0) of MB decomposition/desorption under 785nm exposure was calculated to be *4.8x* higher than for MB under equal intensity 532nm exposure.

It is worth noting that the signal degradation enhancement under the 532nm laser was not zero. The high electromagnetic fields formed on the Ag surface under 532nm irradiation can cause instabilities in surface adsorbates and localized heating of the samples above the controlled reactor temperature can potentially occur during the prolonged laser exposure required in these studies.[44] Adsorbate instability due to high electromagnetic fields and heating cannot however explain the higher 785nm degradation rates compared to 532nm. The higher 785nm degradation rates suggest that the observed charge transfer, which we have shown leads to pumping of excited vibrational modes, yields more unstable and reactive adsorbate molecules.

4.6 Conclusions and outlook

In this chapter, we have coupled optical characterization methods with kinetic analysis of the rates of photo-catalytic reactions to study the interaction of a probe molecule with optically excited plasmonic Ag nanoparticles. Specifically, our measurements and analysis of wavelength-dependent anti-Stokes and Stokes Raman spectra and their connection to photocatalytic decomposition/desorption of MB on Ag provide unique insight into the specifics of the mechanism of plasmon-mediated photocatalysis. We demonstrated that in the systems where the LSPR-mediated charge transfer from nanoparticles to adsorbates takes place, this charge transfer process results

in elevated rates of chemical transformation. Furthermore, we showed that the mechanism of charge transfer involves the action of strong localized LSPR-induced electric field that results in an energy-specific direct electron excitation from occupied to unoccupied orbitals of the molecule-nanoparticle complex. Our findings suggest that the role of LSPR is somewhat decoupled from the role of the local electronic structure in plasmonic photocatalysis, and that by engineering plasmonic nanomaterials with resonant wavelengths matching the charge excitation energies of adsorbates interacting with the plasmonic nanostructure, it is possible to design systems that can support very high rates of electronic excitations between electronic states of a particular energy. These observations provide a foundation for the development of plasmonic catalysts that can selectively activate targeted chemical bonds since it is implied that plasmonic nanomaterials can be tuned in such a way that under illumination they selectively enhance particular chemical pathways.

4.7 References

(1) Zhou, X.; Liu, G.; Yu, J.; Fan, W. Surface Plasmon Resonance-Mediated Photocatalysis by Noble Metal-Based Composites under Visible Light. *J. Mater. Chem.* **2012**, *22*, 21337–21354.

(2) Marimuthu, A.; Zhang, J.; Linic, S. Tuning Selectivity in Propylene Epoxidation by Plasmon Mediated Photo-Switching of Cu Oxidation State. *Science* **2013**, *339*, 1590–1593.

(3) Linic, S.; Christopher, P.; Ingram, D. B. Plasmonic-Metal Nanostructures for Efficient Conversion of Solar to Chemical Energy. *Nat. Mater.* **2011**, *10*, 911–921.

(4) Mukherjee, S.; Libisch, F.; Large, N.; Neumann, O.; Brown, L. V; Cheng, J.; Lassiter, J. B.; Carter, E. A.; Nordlander, P.; Halas, N. J. Hot Electrons Do the Impossible: Plasmon-Induced Dissociation of H_2 on Au. *Nano Lett.* **2013**, *13*, 240–247.

(5) Christopher, P.; Xin, H.; Linic, S. Visible-Light-Enhanced Catalytic Oxidation Reactions on Plasmonic Silver Nanostructures. *Nat. Chem.* **2011**, *3*, 467–472.

(6) Scholl, J. A.; Koh, A. L.; Dionne, J. A. Quantum Plasmon Resonances of Individual Metallic Nanoparticles. *Nature* **2012**, *483*, 421–427.

(7) Christopher, P.; Xin, H.; Marimuthu, A.; Linic, S. Singular Characteristics and Unique Chemical Bond Activation Mechanisms of Photocatalytic Reactions on Plasmonic Nanostructures. *Nat. Mater.* **2012**, *11*, 1044–1050.

(8) Mukherjee, S.; Zhou, L.; Goodman, A. M.; Large, N.; Ayala-Orozco, C.; Zhang, Y.; Nordlander, P.; Halas, N. J. Hot-Electron-Induced Dissociation of H2 on Gold Nanoparticles Supported on SiO2. *J. Am. Chem. Soc.* **2014**, *136*, 64–67.

(9) Jeong, D. H.; Jang, N. H.; Suh, J. S.; Moskovits, M. Photodecomposition of Diazanaphthalenes Adsorbed on Silver Colloid Surfaces. *J. Phys. Chem. B* **2000**, *104*, 3594–3600.

(10) Gadzuk, J. W. Vibrational Excitation in Molecule–surface Collisions due to Temporary Negative Molecular Ion Formation. *J. Chem. Phys.* **1983**, *79*, 6341.

(11) Linic, S.; Aslam, U.; Boerigter, C.; Morabito, M. Photochemical Transformations on Plasmonic Metal Nanoparticles. *Nat. Mater.* **2015**, *14*, 567–576.

(12) Suh, J. S.; Jang, N. H.; Jeong, D. H.; Moskovits, M. Adsorbate Photochemistry on a Colloid Surface: Phthalazine on Silver. *J. Phys. Chem.* **1996**, *100*, 805–813.

(13) Suh, J. S.; Moskovits, M.; Shakhesemampour, J. Photochemical Decomposition at Colloid Surfaces. *J. Phys. Chem.* **1993**, *97*, 1678–1683.

(14) Im, S. H.; Lee, Y. T.; Wiley, B.; Xia, Y. Large-Scale Synthesis of Silver

Nanocubes: The Role of HCl in Promoting Cube Perfection and Monodispersity. *Angew. Chem. Int. Ed. Engl.* **2005**, *44*, 2154–2157.

(15) Ghaedi, M.; Heidarpour, S.; Nasiri Kokhdan, S.; Sahraie, R.; Daneshfar, A.; Brazesh, B. Comparison of Silver and Palladium Nanoparticles Loaded on Activated Carbon for Efficient Removal of Methylene Blue: Kinetic and Isotherm Study of Removal Process. *Powder Technol.* **2012**, *228*, 18–25.

(16) Oskooi, A. F.; Roundy, D.; Ibanescu, M.; Bermel, P.; Joannopoulos, J. D.; Johnson, S. G. Meep: A Flexible Free-Software Package for Electromagnetic Simulations by the FDTD Method. *Comput. Phys. Commun.* **2010**, *181*, 687–702.

(17) Rakic, A. D.; Djurišic, A. B.; Elazar, J. M.; Majewski, M. L. Optical Properties of Metallic Films for Vertical-Cavity Optoelectronic Devices. *Appl. Opt.* **1998**, *37*, 5271.

(18) Enkovaara, J.; Rostgaard, C.; Mortensen, J. J.; Chen, J.; Dułak, M.; Ferrighi, L.; Gavnholt, J.; Glinsvad, C.; Haikola, V.; Hansen, H. A.; *et al.* Electronic Structure Calculations with GPAW: A Real-Space Implementation of the Projector Augmented-Wave Method. *J. Phys. Condens. Matter* **2010**, *22*, 253202.

(19) Hammer, B.; Hansen, L. B.; Nørskov, J. K. Improved Adsorption Energetics within Density-Functional Theory Using Revised Perdew-Burke-Ernzerhof Functionals. *Phys. Rev. B* **1999**, *59*, 7413–7421.

(20) Wellendorff, J.; Lundgaard, K. T.; Møgelhøj, A.; Petzold, V.; Landis, D. D.; Nørskov, J. K.; Bligaard, T.; Jacobsen, K. W. Density Functionals for Surface Science: Exchange-Correlation Model Development with Bayesian Error Estimation. *Phys. Rev. B* **2012**, *85*, 235149.

(21) Hao, E.; Schatz, G. C. Electromagnetic Fields around Silver Nanoparticles and Dimers. *J. Chem. Phys.* **2004**, *120*, 357–366.

(22) Tao, A. R.; Ceperley, D. P.; Sinsermsuksakul, P.; Neureuther, A. R.; Yang, P. Self-Organized Silver Nanoparticles for Three-Dimensional Plasmonic Crystals. *Nano Lett.* **2008**, *8*, 4033–4038.

(23) Rycenga, M.; Cobley, C. M.; Zeng, J.; Li, W.; Moran, C. H.; Zhang, Q.; Qin, D.; Xia, Y. Controlling the Synthesis and Assembly of Silver Nanostructures for Plasmonic Applications. *Chem. Rev.* **2011**, *111*, 3669–3712.

(24) Sherry, L. J.; Chang, S.-H.; Schatz, G. C.; Van Duyne, R. P.; Wiley, B. J.; Xia, Y. Localized Surface Plasmon Resonance Spectroscopy of Single Silver Nanocubes. *Nano Lett.* **2005**, *5*, 2034–2038.

(25) Zuloaga, J.; Prodan, E.; Nordlander, P. Quantum Description of the Plasmon Resonances of a Nanoparticle Dimer. *Nano Lett.* **2009**, *9*, 887–891.

(26) Tan, S. F.; Wu, L.; Yang, J. K. W.; Bai, P.; Bosman, M.; Nijhuis, C. a. Quantum Plasmon Resonances Controlled by Molecular Tunnel Junctions. *Science.* **2014**,

343, 1496–1499.

(27) Esteban, R.; Borisov, A. G.; Nordlander, P.; Aizpurua, J. Bridging Quantum and Classical Plasmonics with a Quantum-Corrected Model. *Nat. Commun.* **2012**, *3*, 825.

(28) Savage, K. J.; Hawkeye, M. M.; Esteban, R.; Borisov, A. G.; Aizpurua, J.; Baumberg, J. J. Revealing the Quantum Regime in Tunnelling Plasmonics. *Nature* **2012**, *491*, 574–577.

(29) Mortensen, N. A.; Raza, S.; Wubs, M.; Søndergaard, T.; Bozhevolnyi, S. I. A Generalized Non-Local Optical Response Theory for Plasmonic Nanostructures. *Nat. Commun.* **2014**, *5*, 3809.

(30) Kaczor, A.; Malek, K.; Baranska, M. Pyridine on Colloidal Silver. Polarization of Surface Studied by Surface-Enhanced Raman Scattering and Density Functional Theory Methods. *J. Phys. Chem. C* **2010**, *114*, 3909–3917.

(31) Xiao, G.-N.; Man, S.-Q. Surface-Enhanced Raman Scattering of Methylene Blue Adsorbed on Cap-Shaped Silver Nanoparticles. *Chem. Phys. Lett.* **2007**, *447*, 305–309.

(32) Nicolai, S. H. A.; Rubim, J. C. Surface-Enhanced Resonance Raman (SERR) Spectra of Methylene Blue Adsorbed on a Silver Electrode. *Langmuir* **2003**, *19*, 4291–4294.

(33) García-Vidal, F.; Pendry, J. Collective Theory for Surface Enhanced Raman Scattering. *Phys. Rev. Lett.* **1996**, *77*, 1163–1166.

(34) Schatz, G. C.; Young, M. A.; Van Duyne, R. P. *Surface-Enhanced Raman Scattering*; Kneipp, K.; Moskovits, M.; Kneipp, H., Eds.; Topics in Applied Physics; Springer Berlin Heidelberg, 2006; Vol. 103.

(35) Kambhampati, P.; Child, C. M.; Foster, M. C.; Campion, A. On the Chemical Mechanism of Surface Enhanced Raman Scattering: Experiment and Theory. *J. Chem. Phys.* **1998**, *108*, 5013.

(36) Maher, R. C.; Galloway, C. M.; Le Ru, E. C.; Cohen, L. F.; Etchegoin, P. G. Vibrational Pumping in Surface Enhanced Raman Scattering (SERS). *Chem. Soc. Rev.* **2008**, *37*, 965–979.

(37) Kneipp, K.; Wang, Y.; Kneipp, H.; Itzkan, I.; Dasari, R.; Feld, M. Population Pumping of Excited Vibrational States by Spontaneous Surface-Enhanced Raman Scattering. *Phys. Rev. Lett.* **1996**, *76*, 2444–2447.

(38) Haslett, T. L.; Tay, L.; Moskovits, M. Can Surface-Enhanced Raman Scattering Serve as a Channel for Strong Optical Pumping? *J. Chem. Phys.* **2000**, *113*, 1641.

(39) Marimuthu, A.; Christopher, P.; Linic, S. Design of Plasmonic Platforms for Selective Molecular Sensing Based on Surface-Enhanced Raman Spectroscopy. *J.*

Phys. Chem. C **2012**, *116*, 9824–9829.

(40) Itoh, T.; Yoshida, K.; Biju, V.; Kikkawa, Y.; Ishikawa, M.; Ozaki, Y. Second Enhancement in Surface-Enhanced Resonance Raman Scattering Revealed by an Analysis of Anti-Stokes and Stokes Raman Spectra. *Phys. Rev. B* **2007**, *76*, 85405.

(41) Hogiu, S.; Werncke, W.; Pfeiffer, M.; Elsaesser, T. Mode Specific Vibrational Kinetics after Intramolecular Electron Transfer Studied by Picosecond Anti-Stokes Raman Spectroscopy. *Chem. Phys. Lett.* **1999**, *312*, 407–414.

(42) Joseph, V.; Engelbrekt, C.; Zhang, J.; Gernert, U.; Ulstrup, J.; Kneipp, J. Characterizing the Kinetics of Nanoparticle-Catalyzed Reactions by Surface-Enhanced Raman Scattering. *Angew. Chemie Int. Ed.* **2012**, *51*, 7592–7596.

(43) Antosiewicz, T. J.; Wadell, C.; Langhammer, C. Plasmon-Assisted Indirect Light Absorption Engineering in Small Transition Metal Catalyst Nanoparticles. *Adv. Opt. Mater.* **2015**, n/a-n/a.

(44) Adleman, J. R.; Boyd, D. A.; Goodwin, D. G.; Psaltis, D. Heterogenous Catalysis Mediated by Plasmon Heating. *Nano Lett.* **2009**, *9*, 4417–4423.

Chapter 5

Engineering the Efficient Flow of Charge and Energy from Plasmonic Nanostructures to Chemically Attached Materials

5.1 Summary

Plasmonic metal nanoparticles can efficiently convert the energy of visible photons into the energy of hot charge carriers within the nanoparticles. These energetic charge carriers can transfer to molecules or semiconductors, chemically attached to the nanoparticles, where they can induce photo-chemical transformations. Classical models of photo-induced charge excitation and transfer in metals suggest that the majority of the energetic charge carriers rapidly decay within the metal nanostructure before they are transferred into the neighboring molecule or semiconductor, and therefore the efficiency of charge transfer is low. Chapter 4 of this dissertation called into question this conventional picture, presenting experimental evidence that under specific conditions there can be direct, efficient charge transfer between metal and molecule. This chapter delves further into this finding, looking specifically into how this direct transfer

mechanism changes the flow of energy within the excited plasmonic system. Evidence is presented that when the nanoparticle-adsorbate system experiences high rates of direct, resonant flow of charge from the nanoparticle to the molecule, the conventional charge excitation and thermalization process that typically takes place in the nanoparticle is bypassed. This picture of charge transfer and energy flow suggests that the yield of extracted hot electrons (or holes) from plasmonic nanoparticles can be significantly higher than the yields expected based on conventional models. This chapter includes a conceptual physical framework that allows for explanation of the experimental observations. This analysis points in a direction toward molecular control of the charge transfer process using interface and local field engineering strategies.

5.2 Introduction

Plasmonic nanoparticles are potentially useful in a number of critical technologies, including solar-to-chemical[1–3] and solar-to-electrical[4–6] energy conversion, molecular characterization,[7–9] imaging,[10–12] lasing,[13,14]and cancer tissue targeting.[15–18] These applications take advantage of a resonant interaction of photons with the collective motion of free charge carriers in a metallic nanoparticle, referred to as localized surface plasmon resonance (LSPR). LSPR is characterized by an elevated optical extinction coefficient at the resonant frequencies and the confinement and concentration of electromagnetic energy (in the form of electric fields) at the nanoparticle surface. The energy is dissipated through the formation of energetic charge carriers within the nanoparticle (accompanied by heating of the nanoparticle) or scattering of photons into the far field.

While in some of these applications it is critical to design plasmonic nanostructures that minimize the internal losses (*i.e.*, the formation of energetic charge carriers) and maximize the plasmonic light confinement, other applications are based on taking advantage of the charge carrier formation and transfer processes. A question of critical importance for the applications that take advantage of energetic charge carriers, such as photovoltaic cells and photocatalytic systems, is related to the microscopic origin of the plasmon-induced hot carrier formation (hot being defined as having energy >> kT above the Fermi level) on optically excited plasmonic nanoparticles and transfer of charge carriers to the medium where they perform a function.[19,20] It should be noted this definition of charge extraction is not related to the photo-emission of charge into vacuum; rather, it refers to charge transfer from the nanoparticle to the chemically attached medium such as an adsorbed molecule or semiconductor.

Most of our current understanding of the process of charge excitation in plasmonic nanoparticles and its transfer to a chemically attached medium is based on the physical models developed for extended metal surfaces. In this picture, the process of electronic excitation (*i.e.*, the photon-induced formation of energetic charge carriers in a metal nanoparticle) takes place mainly in the metal and is not heavily influenced by the chemically attached medium. In this mechanism (see Figure 5-1a), a plasmon (*i.e.*, photon interacting with a plasmonic nanoparticle) relaxes within a few femtoseconds by forming energetic an electron-hole pair in the metal. These energetic charge carriers "cool off" by colliding with other electrons within a couple hundreds of femtoseconds yielding a Fermi-Dirac distribution, albeit at an elevated temperature. This charge distribution further relaxes by colliding with phonon modes within a few picoseconds,

resulting in heating of the nanoparticle. Finally, the excited phonons further equilibrate with the environment at a time scale of hundreds of ps.[21,22] In this conventional picture, hot charge carriers can potentially be extracted from these excited electron distributions *(i.e.*, before they are completely cooled) to a chemically attached medium (the adsorbed molecule or a semiconductor). The corollary of this conventional picture is that the yield of extracted hot charge carriers is low,[23] since a significant fraction of formed energetic charge carriers do not have sufficient energy to be transferred and most of the charge carrier energy is further lost through the interactions with electrons and phonons within the nanoparticle.

While the above discussed conventional charge excitation/transfer mechanism has, to a large extent, guided the field, there have also been multiple experimental observations reporting that the presence of a chemically attached medium (an adsorbate or a material with a different dielectric function) on a plasmonic nanoparticle can lead to faster relaxation of LSPR compared to the free plasmonic nanoparticles.[24,25] This surroundings–induced LSPR relaxation channel is generally referred to as chemical interface damping (CID). For example, it has been demonstrated recently that when a semiconductor is chemically bound to a plasmonic nanoparticle, plasmon relaxation can occur *via* the direct and efficient, simultaneous excitation and transfer of an electron or hole from the metal nanoparticle to the attached semiconductor (*i.e.,* this process of excitation is not mediated by the electronic excitations within the nanoparticle itself).[26]

Chapter 4 of this dissertation also showed that direct charge transfer from plasmonic Ag nanoparticles to strongly bound molecules can take place when the system

is illuminated with resonant light (depicted in Figure 5-1b).[27] It was demonstrated in a case study of methylene blue (MB) adsorbed on Ag nanocubes by analyzing wavelength

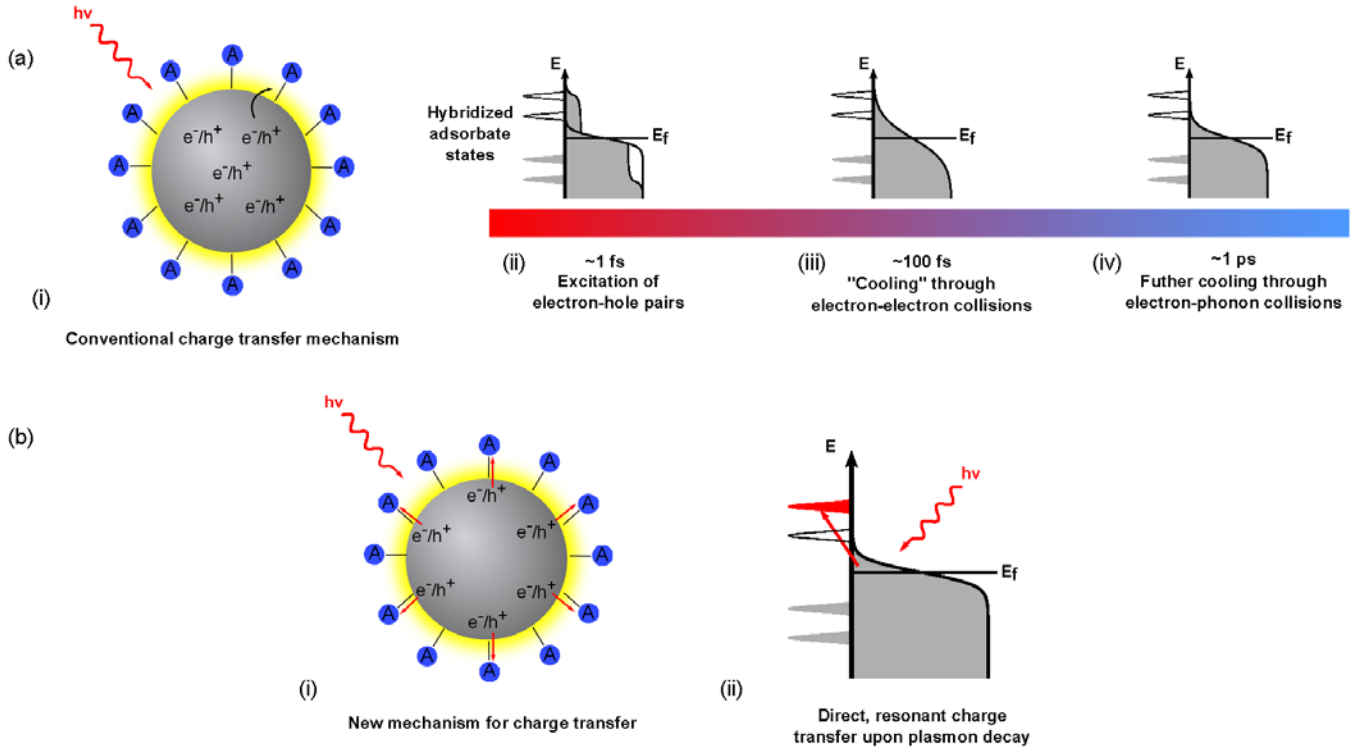

Figure 5-1: Modes of charge excitation and extraction in metals. (a) In the conventional picture of photomediated charge excitation in metals, (i) photon absorption generates hot electron−hole pairs within the metal. (ii) These electron−hole pairs initially form an athermal (*i.e.*, cannot be described using Fermi−Dirac statistics) hot electron distribution. (iii) This athermal distribution thermalizes/cools through electron−electron collisions taking place on the order of ∼100 fs. (iv) The hot thermalized distribution cools further via electron−phonon interactions on the order of ∼1 ps. When an adsorbate is present, electron transfer from the metal to the adsorbate can theoretically take place at any point during this thermalization process. However, the probability of this transfer is low because of the rapid cooling process and the low number of high-energy charge carriers. (b) (i) The alternative mechanism for charge transfer presented herein is realized when an adsorbate or semiconductor chemically interacts with a plasmonic metal nanoparticle. Plasmon excitation of the nanoparticle produces strong field intensities at the interface, facilitating the formation of electron−hole pair at the interface. (ii) Density of states diagram reveals the formation of an alternative channel for direct, resonant transfer of charge carriers to high-energy adsorbate states, which bypasses the thermalization of hot electrons in the metal depicted in part (a) of this figure.

and intensity-dependent anti-Stokes and Stokes surface-enhanced Raman scattering (SERS) intensities of adsorbed MB. This direct charge transfer has also been postulated to explain enhancements of Raman signal that could not be explained through traditional electromagnetic SERS theory.[28,29] These studies provide experimental evidence that ultrafast charge excitation/transfer at the interface of plasmonic nanoparticles and chemically attached mediums can take place, yet questions related to the exact microscopic origin of the charge transfer process and the driving forces that make this transfer possible persist.

In this chapter, we attempt to further clarify the microscopic mechanism of the excitation and flow of energetic charge in plasmonic nanoparticle-adsorbate systems. We do so using anti-Stokes and Stokes SERS methods similar to Chapter 4. This time however, we use the data to simultaneously measure the vibrational temperature of the plasmonic metal nanoparticle and the attached adsorbates. We demonstrate that in the case of MB molecules chemisorbed on Ag, the high rates of direct flow of charge from the nanoparticle to the molecule, observed at resonant frequencies, result in the lack of thermal equilibrium between the adsorbate and nanoparticle *i.e.*, the molecule is heated to a much greater extent than the nanoparticle. We also develop and discuss a conceptual physical model that allows us to explain our experimental observations and more generally shed light on the direct charge transfer mechanism of LSPR relaxation. This analysis points us in a direction of molecular control of the charge excitation and transfer process using interface and local field engineering strategies. This picture of charge transfer suggests that the yield of extracted hot electrons (or holes) on plasmonic

nanoparticles can be significantly higher than the yields expected based on the conventional models.

5.3 Experimental methods

5.3.1 Nanoparticle synthesis and Raman sample preparation

The plasmonic nanoparticles were silver nanocubes, synthesized using the modified polyol method.[30] . All aspects of this synthesis are described in detail in Chapter 2, *Section 2.3.1*. After synthesis, the cubes were washed 5x by centrifugation and re-dispersion in a combination of acetone and ethanol. After washing, the cubes were dispersed in 5 mL of ethanol. After synthesis and washing, both the colloidal suspension and the aggregates on a solid substrate were characterized by UV-vis spectrophotometry (Thermo Evolution 300). Samples for extinction measurements of dry Ag aggregates on solid support were prepared by drop coating ~200 μL of the colloidal solution onto a 1 in^2 glass slide and allowing the solvent to evaporate. Transmission electron microscopy (TEM) samples were prepared by depositing ~2 μL of the colloidal nanoparticle solution on a carbon film TEM grid (the amount deposited was chosen to mimic the density of particles used in optical and Raman studies). Aberration corrected TEM (JEOL 3100, accelerating voltage 300 kV) was used to characterize the Ag nanocubes, which were found to have an average edge length of 71 ± 9 nm.

Methylene blue (MB) and Rhodamine 6G (R6G), were used as probe molecules in the Raman experiments. One of the dye molecules was added to a colloidal solution of Ag nanocubes at a concentration of 40μM and allowed to incubate for several hours to ensure full equilibrium adsorption of the dye onto the silver surface.[31] Adding the dyes while the particles are still in liquid solution allows the molecules to access all available

adsorption sites on the Ag particles. Solid samples for Raman studies were prepared by drop coating ~ 30 μL of the Ag-dye solution onto a 1 cm^2 silicon chip and allowing the ethanol solvent to evaporate, leaving behind a thin layer of silver-dye aggregates. The as-prepared samples were, in addition to use to in Raman studies, also characterized by TEM as described in Chapter 2, *Section 2.6.2*.

Figure 5-1 shows TEM images of Ag nanoparticles both before and after MB was added to the colloidal nanoparticle solutions. The micrograph for MB-free Ag nanocubes shows many individual nanocubes dispersed over the TEM sample grid. A few Ag nanowires and spherical particles are also formed during the synthesis. When MB is adsorbed on the surface of the nanoparticles, nearly all of the nanocubes aggregate into relatively large clusters. These aggregates are characterized by large numbers of plasmonic hot spots.

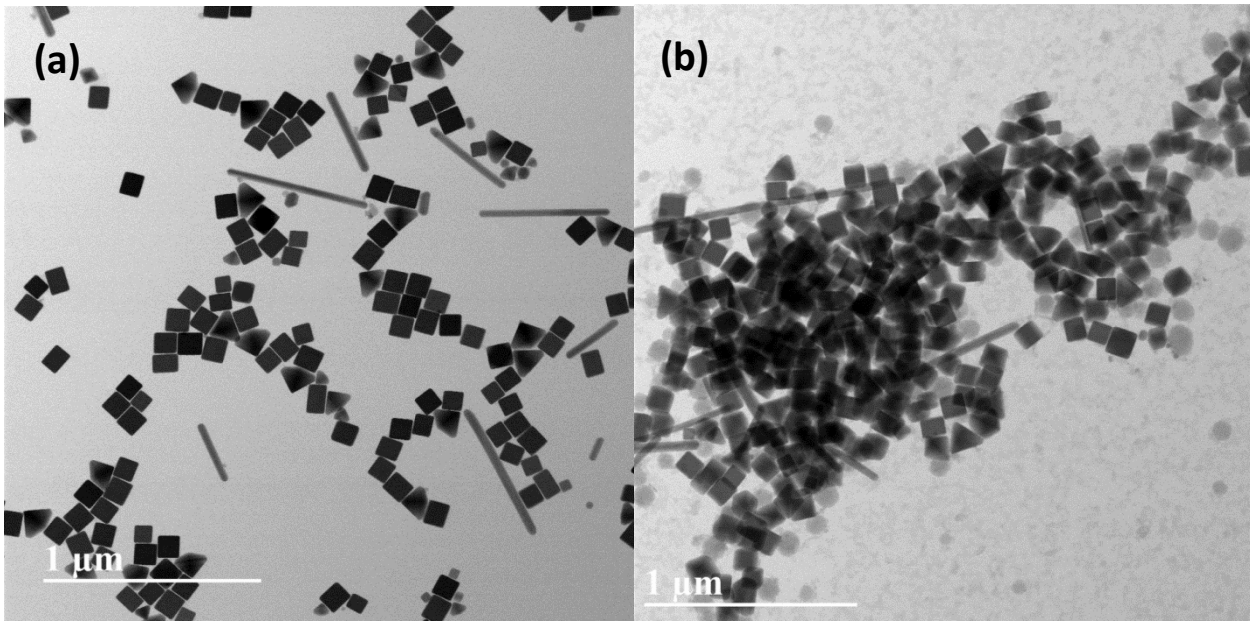

Figure 5-2: TEM images of Ag cube samples. (a) TEM image of synthesized, washed Ag nanocubes with no added methylene blue. (b) TEM image of synthesized, washed Ag nanocubes with methylene blue added. Notice that while addition of MB does not change the morphology of individual cubes, which have ~71nm edge length, it does cause significant aggregation.

5.3.2 Temperature controlled Raman studies

Raman studies were conducted in a temperature-controlled Harrick Praying Mantis reaction chamber designed for Raman spectroscopy. A sample of Ag-dye aggregates on a silicon chip was placed inside the chamber, with the transparent reactor window allowing Raman spectra to be collected. The set temperature of the sample within the reactor could then be controlled, and pure nitrogen could be flowed through the reactor to provide an inert atmosphere and allowing for convective sample cooling, limiting oxidation of the Ag surface and photo-degradation of the dye. Stokes and anti-Stokes Raman spectra were gathered using a Horiba LabRAM HR system under excitation from either a 532 nm diode-pumped solid state laser, or a 785 nm diode laser. The laser was focused on nanoparticle aggregates visible through a 10x confocal microscope lens. Full spectra were gathered at 15 K temperature intervals from 298 K to 373 K, with time given in between each measurement for the sample temperature to equilibrate.

5.3.3 Calculation of adsorbate vibrational mode temperatures

While the K value for a given vibrational mode in a sample can tell us the deviation from the expected value of an anti-Stokes peak, it is often useful to perform a different quantitative calculation to compare the extent of vibrational excitation in a molecule compared to its surroundings. For this purpose, we can calculate, using the same anti-Stokes to Stokes peak ratios in a given spectrum, the *temperature* of the vibrational mode.[32] This temperature is then compared to the actual temperature of the surrounding environment or other temperature values calculated using the Raman data.

The vibrational temperature of a specific mode can be calculated based on the anti-Stokes to Stokes ratio for that mode, similar to K, because it is based on the same Boltzmann distribution. In this case, the distribution equation is rearranged as shown in Equation 5-2 to calculate temperature as a function of anti-Stokes to Stokes ratio:

$$T_{vibr} = -\frac{E_{vibr}}{k_B * \ln(I_{aS}/I_{St})} \quad (5\text{-}1)$$

where T_{vibr} is the calculated temperature of the mode, E_{vibr} is the energy of the mode, and I_{aS} and I_{St} the anti-Stokes and Stokes intensities (properly calibrated as described in Chapter 3) of that vibrational mode, respectively.

5.3.4 Calculation of Ag nanoparticle electronic temperatures

In addition to the behavior of the probe molecule in instances of Raman scattering, in SERS, where the probe is anchored to a plasmonic metal surface, the Raman spectrum can be used to study the response of the plasmonic substrate to laser illumination. Hugall and Baumberg showed recently that the background SERS signal, present in all SERS measurement and independent of the probe molecule attached, provides important information about the temperature of the plasmonic substrate.[33] This is because the electrons within the plasmonic particle can participate in Raman scattering on their own.

The local nanoparticle temperature can be measured based on the intensity of the SERS anti-Stokes background signal.[34] The central concept is that the anti-Stokes background intensity measures the rate of emission anti-Stokes shifted photons in response to the photon-induced relaxation of electrons within the metal nanoparticle from

the occupied electronic states just above the Fermi level to the unoccupied states just below the Fermi level. The electrons follow a Fermi-Dirac distribution within the nanoparticle based on their temperature. The local equilibrated electronic temperature of the metal can be derived from a rearrangement of this distribution through the relationship in Equation 5-2:

$$I_{aS,\,background} = I_{aS,0}\left[e^{E_{Raman}/k_{B*T}} + 1\right]^{-1} \qquad (5\text{-}2)$$

where $I_{aS,background}$ is the intensity of the anti-Stokes SERS background at a given energy of Raman shift, E_{Raman}, and $I_{aS,0}$ is the intensity of the anti-Stokes SERS at $E_{Raman} = 0$. Equation 5-2 can easily be rearranged to a linear form:

$$\ln\left(\frac{I_{aS,0}}{I_{aS}} - 1\right) = \frac{1}{k_B T} * E_{Raman} \qquad (5\text{-}3)$$

We calculate the theoretical $I_{aS,0}$ by looking at the anti-Stokes background signal at high Raman shifts, where:

$$e^{E_{Raman}/k_B T} \gg 1 \qquad (5\text{-}4)$$

and therefore:

$$I_{aS,0}\left[e^{E_{Raman}/k_B T} + 1\right]^{-1} \sim I_{aS,0} * e^{-E_{Raman}/k_B T}$$

$$I_{aS} = I_{aS,0} * e^{-E_{Raman}/k_B T}$$

$$\ln(I_{aS}) = \ln(I_{aS,0}) - \frac{E_{Raman}}{k_B T} \qquad (5\text{-}5)$$

Here, the intercept of the best fit line when plotting $\ln(I_{aS})$ *versus* E_{Raman} is equal to $\ln(I_{aS,0})$. Once this is calculated, we can more accurately determine the local metal temperature by now including lower energy Raman shifts and plotting $\ln(I_{aS,0}/I_{aS} - 1)$ *versus* E_{Raman} as Equation 5-3 would suggest. The slope of the best fit line will be equal to $1/k_BT$. In this way, the *electronic temperature* of the plasmonic SERS substrate can be calculated and compared to both the actual ambient temperature and the probe molecule vibrational mode temperatures.

5.4 Experimental results

5.4.1 Simultaneous nanoparticle and molecule temperature measurement using SERS

To perform the studies of charge flow in the systems, we used Stokes and anti-Stokes surface-enhanced Raman spectroscopy (SERS), employing laser sources with photon wavelengths of 532 and 785 nm. We used clusters of plasmonic silver nanocubes with ~ 70 nm edge length supported on a silicon chip. A probe molecule, methylene blue (MB), was chemisorbed on the nanoparticles as described in *Section 5.3.1*. Figure 5-2 shows TEM images of our model systems. The Ag clusters were characterized by large numbers of hot spots, the regions between two closely spaced plasmonic Ag nanoparticles. FDTD simulations for similar samples in Chapter 4 showed that the maximum electric fields in the hot spots for both 532 nm and 785 nm incident wavelengths were between 10^4 and 10^5 times higher than the source photon field intensities. Furthermore, calculations show that the average field enhancements over the entire surface of nanoparticle aggregates are approximately equal within an order of magnitude for both incident wavelengths.[27]

The highest photon flux produced by the continuous wave lasers used in the experiments was $2.0*10^{20}$ photons cm^{-2} s^{-1}. For the cross-sectional area occupied by one Ag nanocube of ~70nm edge length, this is equivalent to ~ $1.0*10^{10}$ photons per second. Previous studies have shown that for clusters of plasmonic Ag nanoparticles, the optical cross-section is ~ 10 – 50 times larger than the geometric cross-section.[35] Therefore, the average rate of photons interacting with a single nanoparticle is ~$1.0*10^{11}$ to $5*10^{11}$ s^{-1}, and it is proportionally larger for clusters of nanoparticles. This is the upper limit on the average rate of charge carrier formation in a nanoparticle. In practical terms, this means that we are operating at the ps time scale (*i.e.*, the time between formation of charge carriers), and our Raman experiments are probing the behavior of the steady state system where energetic charge carriers have equilibrated with the phonon modes of the metal nanoparticles. We note however that the phonon modes of nanoparticles and adsorbates have not equilibrated with the environment (*i.e.*, they may be at higher temperatures than the environment). As described further below, and depicted in Figure 5-3, by measuring Stokes and anti-Stokes SERS intensities we can concurrently measure the equilibrium (phonon) temperature of the metal nanoparticles and the vibrational temperatures of molecules adsorbed on these nanoparticles. These measurements allow us to follow the flow of excited charge carriers in the system as this charge flow directly impacts these temperatures.

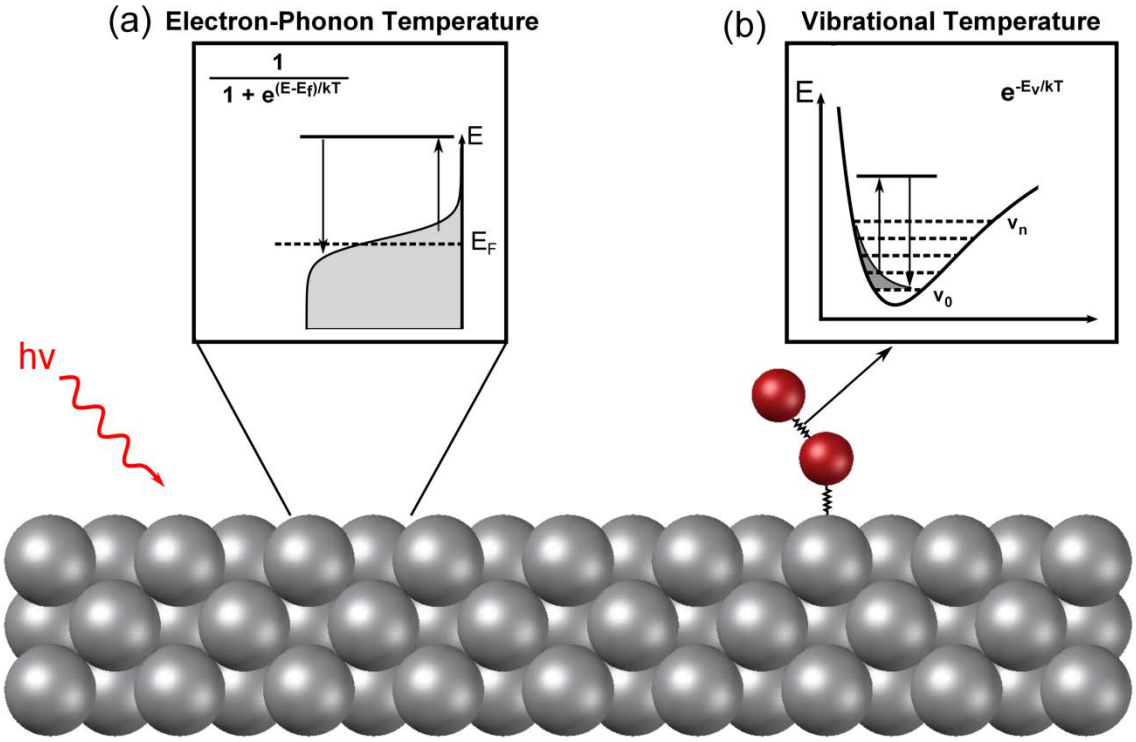

Figure 5-3: Measuring localized phonon temperatures of metal nanoparticles and the vibrational adsorbate temperature. (a) Raman excitation within the metal nanoparticle can excite electrons from states above the Fermi level, which can decay to states below the Fermi level. This inelastic excitation/relaxation process produces an anti-Stokes shifted photon that contributes to the background intensity in anti-Stokes Raman spectroscopy. The anti-Stokes background intensity can then be related to the electronic temperature through the Fermi−Dirac distribution function. (b) The ratio of anti-Stokes to Stokes Raman intensities of a particular vibrational mode of an adsorbed molecule depends on the relative population of the molecules in the vibrationally excited and ground state (represented by the shaded gray area). These mode-specific anti-Stokes and Stokes intensities give us the information about vibrational temperature of the mode through a Boltzmann distribution function.

As the laser source photons are absorbed by a nanoparticle, energetic charge carriers are formed. These charge carriers thermalize with the nanoparticle phonon modes. This process can lead to local heating of the nanoparticles. The local nanoparticle temperature can be measured based on the intensity of the SERS anti-Stokes background signal (subject to corrections for detector sensitivity and unequal electromagnetic enhancements described in Chapter 3)[34]. The central concept here, illustrated in Figure 5-

3a, is that the anti-Stokes background intensity measures the rate of emission of anti-Stokes shifted photons in response to the photon-induced relaxation of electrons within the metal nanoparticle from the occupied electronic states just above the Fermi level to the unoccupied states just below the Fermi level.[34] The Fermi-Dirac distribution function is used to calculate the equilibrated (electron-phonon) temperature of nanoparticles, as shown in *Section 5.3.4*.

Data in the inset of Figure 5-4a show the anti-Stokes spectra of Ag nanoparticles measured under continuous wave (CW) illumination by the 532 nm laser as a function of externally controlled reactor (nanoparticles) temperatures. The reactor temperature was controlled using an external heat source and measured using a thermocouple located directly underneath the sample chip within the reactor vessel. The measured background anti-Stokes intensities were fit to the Fermi-Dirac electron distribution function (as described in *Section 5.3.4*) to quantify the local nanoparticle temperature. Data in Figure 5-4a show that the calculated local nanoparticle temperature scales linearly with the reactor temperature for both lasers measured at equal laser intensities (equal by measure of photon flux). The data show the local nanoparticle temperature under laser illumination is slightly higher than the reactor temperature for both lasers. The slightly higher values of the nanoparticle temperature are the result of light-induced local nanoparticle heating.[36] Higher nanoparticle temperatures under 532 nm illumination compared to 785 nm are likely the result of the higher energy of 532 nm photons.

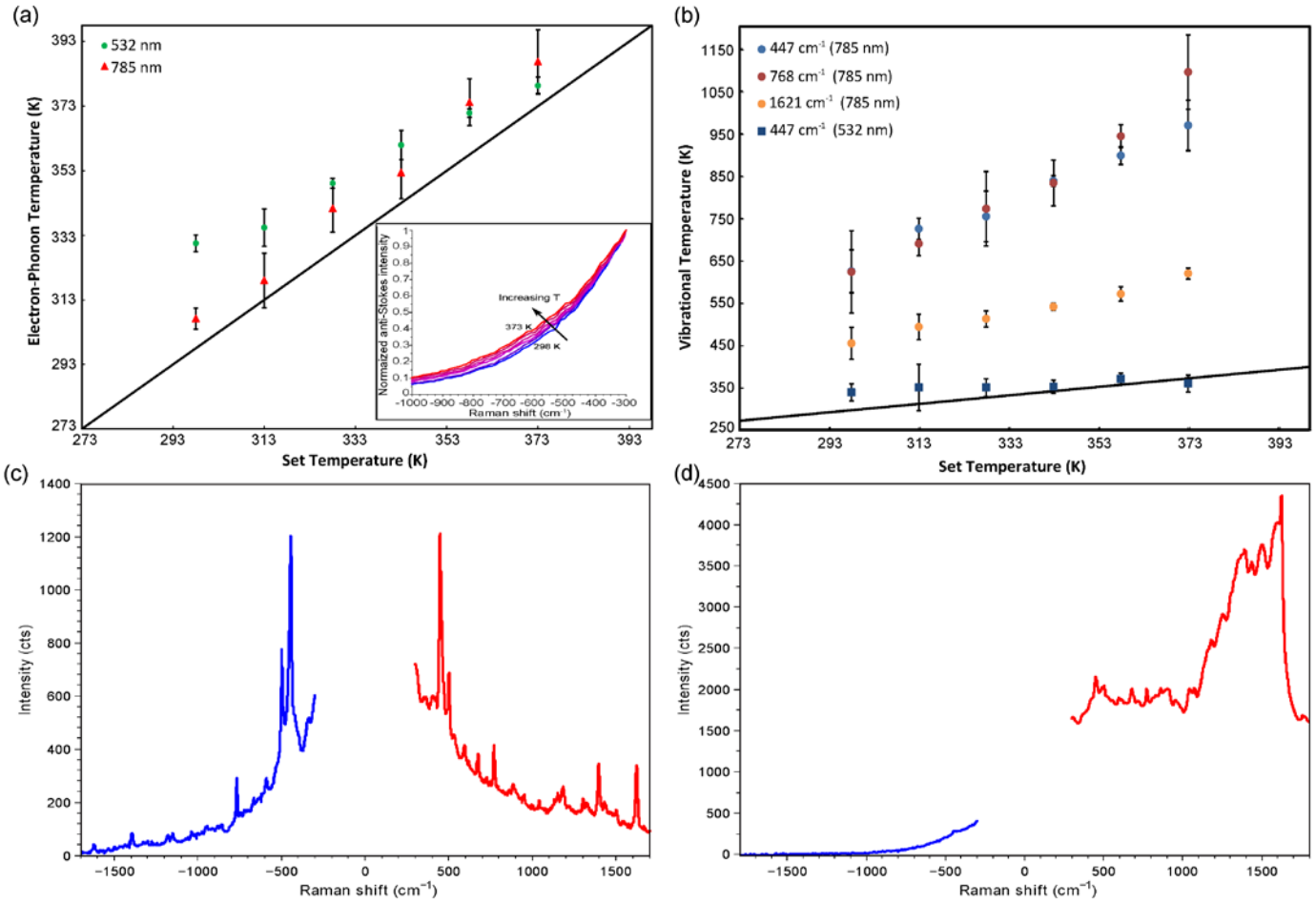

Figure 5-4: Measured nanoparticle and MB adsorbate temperatures and SERS spectra. (a) Temperature of Ag nanoparticles under illumination by the 532 nm laser (green circles) and 785 nm laser (red triangles). Error bars represent the standard deviation of all trial runs. The black solid line is used to guide the viewer, and it represents the measured nanoparticle temperature equal to set temperature. Inset: Anti-Stokes spectra, gathered using the 532 nm laser, of Ag nanocubes (no adsorbate) showing noticeable change in the exponential decay of the SERS background signal as the sample temperature is increased through external heating. (b) Temperatures of the most prominent vibrational modes of MB adsorbed on Ag, calculated using Equation 5-1. Under 532 nm illumination, the vibrational temperature is nearly equal to the set temperature (represented by the black line). We note that under 532 nm illumination due to a very weak anti-Stokes signal, we could with confidence measure only the temperature of the 447 cm^{-1} mode. Under 785 nm illumination, the vibrational temperatures for all modes are significantly increased above the metal nanoparticle temperature, indicating a resonant, selective energy transfer into the MB adsorbate. (c,d) Raw data showing anti-Stokes (blue, representing blue-shifted photons) and Stokes (red, representing red-shifted photons) spectra for silver− methylene blue samples collected using a (c) 785 nm laser and (d) 532 nm laser, showing the exceptionally high anti-Stokes signal under 785 nm due to resonant charge transfer.

In addition to measuring the local nanoparticle temperature by focusing on anti-Stokes background intensities, the analysis of SERS Stokes and anti-Stokes intensities of various vibrational modes of the molecules adsorbed on the surface gives us a measure of the molecular vibrational temperature.[32] In a thermalized vibrational energy distribution, the ratio of the population of excited to ground state vibrational modes, and thus the anti-Stokes to Stokes intensity ratio in Raman measurements, obeys a Boltzmann distribution (see Figure 5-3b). Using the SERS data, the effective temperature of a specific vibrational mode can be calculated as described in *Section 5.3.3.*

Data in Figure 5-4c and 5-4d show anti-Stokes and Stokes SERS spectra for MB adsorbed on the surface of Ag nanoparticles obtained using the 532 and 785 nm laser sources. Both laser sources were set to deliver a photon flux of $2.0*10^{20}$ photons cm^{-2} s^{-1} to the sample. We used Equation 5-1 to calculate the vibrational temperature of the various modes of the MB molecule based on these Raman spectra. Data in Figure 5-4b show the calculated vibrational temperature as a function of the reactor temperature for both lasers. The data show that the temperature of MB vibrational modes is significantly elevated for 785 nm laser compared to local nanoparticle temperature. This strongly elevated MB vibrational temperature under the 785 nm laser is a signature of charge transfer from Ag to MB at this frequency. The vibrational heating of the adsorbed molecule due to vibronic coupling is a side effect of the charge transfer to the molecule.[27] Data in Figures 5-4a and 5-4b also show that for the 532 nm laser, the local nanoparticle temperature and the MB vibrational temperatures are very similar, which suggests a thermally equilibrated system and the lack of charge transfer in the case of the 532 nm laser.

5.5 Charge excitation and transfer in plasmonic nanoparticle-adsorbate systems

As discussed above, the SERS experiments showed that the process of charge exchange between the nanoparticle and adsorbate took place at when excited by 785 nm photons and not 532 nm photons, and that it led to the selective heating of the molecule. Since the lowest energy of photons absorbed by free MB is ~ 665 nm[37] (higher energy than the 785 nm photons), it appears that the observed charge transfer must occur between the metal and molecule (rather than between states wholly within the MB). This charge transfer process most likely involves hybridized electronic states formed in the process of MB chemisorption on the Ag nanoparticles. We attempt to explain these experimental observations in terms of classical theories of photon absorption (*i.e.*, plasmon relaxation) in metals. As discussed, due to a large number of electronic states in the metal, classical models assume that photons are absorbed by forming electron-hole pairs in the metal. This electron-hole pair formation process has been previously described and it proceeds *via*:[38]

(i) Direct photon absorption (plasmon relaxation) by electron excitation from d states below the Fermi level vertically up to s states above the Fermi level, often referred to as interband transitions. In this process electron momentum is conserved. The probability for these transitions is $\gamma_{direct} \sim 10^{15}$ s^{-1} (this is the inverse of the plasmon relaxation time).[39] We note that in Ag, the direct d to s excitations take place at a minimum of ~ 3.6 eV,[40] well above the energy of photons used in these studies, so these direct, vertical absorption processes within Ag cannot be activated in our measurements.

(ii) Indirect phonon-assisted intraband transitions from s states below to s states above the Fermi level. In this process another body, a phonon, is required to conserve the momentum. The probability for this excitation mechanism is $\gamma_{ph} \sim 10^{13} - 10^{14}$ s^{-1}.[41]

(iii) Indirect geometry-assisted intraband transitions from s states below to s states above the Fermi level. This process is known as Landau damping. Here, momentum is conserved by the electron collision with the confined surface modes.[42] The probability for this excitation is dependent on the size of the particle, and it can be described using $\gamma_{geo} \sim v_f/R$, where v_f is the Fermi velocity and R is the radius of the nanoparticle. For silver nanoparticles the probability of these transition is $\sim 10^{14}$ s^{-1} for nanoparticles with diameter of ~ 10 nm, and $\sim 10^{13}$ s^{-1} for nanoparticles with diameter of ~ 100 nm.[38]

(iv) An Umklapp process, characterized by the momentum conserving formation of multiple e-h pairs from a single photon. The probability for this process is $\gamma_{UM} \sim 10^{15}(E_{ph}/E_{Fermi})^2$ s^{-1}, where E_{ph} and E_{Fermi} are the photon and Fermi energy, respectively. For visible photons impinging on an Ag substrate, the probability for this process is $\sim 10^{13} – 10^{14}$ s^{-1}, and this process becomes more relevant at higher photon energy.[43]

This conventional analysis suggests that there are approximately equal probabilities for the three intraband s to s transitions (ii – iv above) for Ag nanoparticles between 10 and 100 nm. The net effect is that due to the broad and featureless s band in Ag, the probability distribution for the initial charge excitation within the Ag nanoparticles for both lasers is essentially a flat function spreading from ($E_{fermi} – E_{ph}$) to

($E_{fermi} + E_{ph}$), yielding the electron energy distribution depicted Figure 5-1a. This is consistent with recently reported first principles calculations, accounting for all the (i) through (iv) transitions in metal nanoparticles.[44] As described in the Figure, this initial electron distribution function changes as electrons and holes cool off, taking the shape of a Fermi-Dirac distribution. If we assume that energetic charge carriers are transferred to the MB molecule from this electron distribution, then due to the similar charge excitation probability distributions at a given intensity, we would expect that both lasers would induce similar rates of charge transfer into adsorbed MB. In fact, we would expect slightly higher rates of charge transfer for the 532 nm laser since more energy is collected by the nanoparticle at this wavelength. This is due to the higher energy of a 532 nm photon as well as the higher extinction coefficient for the Ag SERS substrate at this wavelength compared to 785 nm.[27] This classical model of charge excitation and transfer cannot explain our experimental observations which, as described above, showed that the charge transfer from the Ag metal to the MB adsorbate, accompanied by non-thermalized vibrational heating of the molecule, took place with the 785 nm and not with the 532 nm laser.

To explain our experimental results, it is imperative to move away from this classical picture where the process of photon adsorption is described by only considering the excitations in the metal nanoparticles, and ask a question about the role of adsorbates in changing the process of charge excitation and transfer. When an adsorbate chemisorbs on a metal surface, new hybridized metal-adsorbate states (bands) are formed. These are essentially bonding and anti-bonding orbitals shared by the metal surface atoms and adsorbate. Some of these orbitals are more centered on the metal while others are more

centered on the adsorbate. In the ground state, some of these orbitals (bands) are populated with electrons and some are not. The existence of these states gives rise to the possibility of the direct, vertical, momentum-conserving photon absorption process (similar to the above described interband transitions) where an electron from the populated hybridized state (centered on the metal) is moved vertically up to the unpopulated state (centered on the molecule). This process effectively yields a direct photon-induced charge transfer from the metal to the adsorbate at the adsorbate-metal interface. Since the probability for these interfacial charge transitions is proportional to the coverage of the adsorbates (more specifically the ratio of the hybridized adsorbate-metal states to metal bulk states), on large non-plasmonic nanoparticles and on extended metal surfaces (which have a low fraction of adsorbate states compared to metal bulk states) these transitions are infrequent. Most of the energy is dissipated through the metal states as described above in mechanisms (i) – (iv).

On the other hand, we argue that when plasmonic nanoparticles are involved, this direct charge transfer process involving localized metal-adsorbate orbitals can be the fastest and most probable mechanism for the dissipation of electromagnetic energy. Our results indicate that this is the case for the Ag-MB system at 785 nm excitation. This phenomenon can be explained by two critical factors acting in concert. The first factor is the above-mentioned presence of newly formed electronic states at a particular energy that allow for the ultrafast, direct, momentum-conserved charge transfer process. The second factor is the presence of the elevated LSPR-induced electric field intensity at the given energy, which stimulates these surface charge transfer processes (we note that the rate of optical charge excitation at any point will be proportional to the field intensity,

$|E|^2$).[45] As we described above, the intensity of the electric field in some hot spots between two nanoparticles can be amplified by ~ 10^5 times compared to the incoming photon field. This high field intensity can compensate for the relatively small density of surface electronic states involved in the charge transfer process. We note that the ratio of bulk states to surface states in a 100 nm metal nanoparticle is ~ 50, with the ratio decreasing as nanoparticles get smaller.[46] This essentially means that the LSPR effect can move the optical charge excitation process almost completely to the hot spots.

The proposed model is supported by two recent reports; one showed that very small non-plasmonic Pt nanoparticles (less than 4 nm diameter) exhibited high rates of charge transfer to adsorbed molecules,[47] and another showed that Au nanorods surrounded with CdSe nanoparticles exhibited a high degree of charge transfer to CdSe.[26] Our analysis can describe both observations. In the first case, as described by the authors, the charge transfer was driven by a large number of surface-adsorbate states compared to metal bulk states, which gives rise to rapid direct charge transfer at the surface (even without high field intensity). In the second case, the charge transfer process was most likely driven by the LSPR-induced strong electric field enhancements at the interface of the metal nanoparticle and semiconductor.

5.6 Conclusions and Outlook

In the introduction it was suggested that various technologies can benefit from high rates of hot carrier transfer from illuminated plasmonic metal nanoparticles to a chemically interacting medium (an adsorbate or a semiconductor) and that served as motivation for the discussion. The data suggests that the high rates of hot carrier transfer

can be stimulated by engineering interfaces that are characterized by the existence of donor and acceptor electronic states of a particular energy and high electric fields that can support the transitions at this particular energy. Normally in these systems, the injected charges are “transient” since they remain in the hybrid states for only a few femtoseconds before relaxing back into the metal, following one of the many available dissipative pathways.[48] While this transient charge transfer is sufficient to drive chemical transformations on adsorbates (*via* the above-described vibronic coupling),[49–51] it might not be sufficient for some other applications such as photo-chemistry on attached semiconductors or charge harvesting for solar applications. Improving these systems will require designing interfaces that optimize the harvesting of these energetic carriers once they are formed outside the nanoparticle and prevent them from simply relaxing back into the metal. One way to potentially achieve this is to manipulate the local electrostatic fields, making them work to extract these hot carriers away from the metal and into the desired material once they are formed.

5.7 References

(1) Linic, S.; Christopher, P.; Ingram, D. B. Plasmonic-Metal Nanostructures for Efficient Conversion of Solar to Chemical Energy. *Nat. Mater.* **2011**, *10*, 911–921.

(2) Zhou, X.; Liu, G.; Yu, J.; Fan, W. Surface Plasmon Resonance-Mediated Photocatalysis by Noble Metal-Based Composites under Visible Light. *J. Mater. Chem.* **2012**, *22*, 21337–21354.

(3) Hou, W.; Cronin, S. B. A Review of Surface Plasmon Resonance-Enhanced Photocatalysis. *Adv. Funct. Mater.* **2013**, *23*, 1612–1619.

(4) Atwater, H. A.; Polman, A. Plasmonics for Improved Photovoltaic Devices. *Nat. Mater.* **2010**, *9*, 205–213.

(5) Tian, Y.; Tatsuma, T. Mechanisms and Applications of Plasmon-Induced Charge Separation at TiO2 Films Loaded with Gold Nanoparticles. *J. Am. Chem. Soc.* **2005**, *127*, 7632–7637.

(6) Li, Y.; Yan, X.; Wu, Y.; Zhang, X.; Ren, X. Plasmon-Enhanced Light Absorption in GaAs Nanowire Array Solar Cells. *Nanoscale Res. Lett.* **2015**, *10*, 436.

(7) Moskovits, M. Surface-Enhanced Spectroscopy. *Rev. Mod. Phys.* **1985**, *57*, 783–826.

(8) Moskovits, M. Surface-Enhanced Raman Spectroscopy: A Brief Retrospective. *J. Raman Spectrosc.* **2005**, *36*, 485–496.

(9) Marimuthu, A.; Christopher, P.; Linic, S. Design of Plasmonic Platforms for Selective Molecular Sensing Based on Surface-Enhanced Raman Spectroscopy. *J. Phys. Chem. C* **2012**, *116*, 9824–9829.

(10) Jain, P. K.; Huang, X.; El-Sayed, I. H.; El-Sayed, M. A. Noble Metals on the Nanoscale: Optical and Photothermal Properties and Some Applications in Imaging, Sensing, Biology, and Medicine. *Acc. Chem. Res.* **2008**, *41*, 1578–1586.

(11) Lee, K.-S.; El-Sayed, M. A. Gold and Silver Nanoparticles in Sensing and Imaging: Sensitivity of Plasmon Response to Size, Shape, and Metal Composition. *J. Phys. Chem. B* **2006**, *110*, 19220–19225.

(12) Loo, C.; Lin, A.; Hirsch, L.; Lee, M. H.; Barton, J.; Halas, N.; West, J.; Drezek, R. Nanoshell-Enabled Photonics-Based Imaging and Therapy of Cancer. *Technol. Cancer Res. Treat.* **2004**, *3*, 33–40.

(13) Zhou, W.; Dridi, M.; Suh, J. Y.; Kim, C. H.; Co, D. T.; Wasielewski, M. R.; Schatz, G. C.; Odom, T. W. Lasing Action in Strongly Coupled Plasmonic Nanocavity Arrays. *Nat. Nanotechnol.* **2013**, *8*, 506–511.

(14) Lu, Y.-J.; Kim, J.; Chen, H.-Y.; Wu, C.; Dabidian, N.; Sanders, C. E.; Wang, C.-Y.; Lu, M.-Y.; Li, B.-H.; Qiu, X.; *et al.* Plasmonic Nanolaser Using Epitaxially Grown Silver Film. *Science* **2012**, *337*, 450–453.

(15) Huang, X.; El-Sayed, I. H.; Qian, W.; El-Sayed, M. A. Cancer Cell Imaging and Photothermal Therapy in the Near-Infrared Region by Using Gold Nanorods. *J. Am. Chem. Soc.* **2006**, *128*, 2115–2120.

(16) El-Sayed, I. H.; Huang, X.; El-Sayed, M. A. Selective Laser Photo-Thermal Therapy of Epithelial Carcinoma Using Anti-EGFR Antibody Conjugated Gold Nanoparticles. *Cancer Lett.* **2006**, *239*, 129–135.

(17) Hirsch, L. R.; Stafford, R. J.; Bankson, J. a; Sershen, S. R.; Rivera, B.; Price, R. E.; Hazle, J. D.; Halas, N. J.; West, J. L. Nanoshell-Mediated near-Infrared Thermal Therapy of Tumors under Magnetic Resonance Guidance. *Proc. Natl. Acad. Sci. U. S. A.* **2003**, *100*, 13549–13554.

(18) Carpin, L. B.; Bickford, L. R.; Agollah, G.; Yu, T.-K.; Schiff, R.; Li, Y.; Drezek, R. a. Immunoconjugated Gold Nanoshell-Mediated Photothermal Ablation of Trastuzumab-Resistant Breast Cancer Cells. *Breast Cancer Res. Treat.* **2011**, *125*, 27–34.

(19) Linic, S.; Aslam, U.; Boerigter, C.; Morabito, M. Photochemical Transformations on Plasmonic Metal Nanoparticles. *Nat. Mater.* **2015**, *14*, 567–576.

(20) Govorov, A. O.; Zhang, H.; Gun'ko, Y. K. Theory of Photoinjection of Hot Plasmonic Carriers from Metal Nanostructures into Semiconductors and Surface Molecules. *J. Phys. Chem. C* **2013**, *117*, 16616–16631.

(21) Voisin, C.; Del Fatti, N.; Christofilos, D.; Vallée, F. Ultrafast Electron Dynamics and Optical Nonlinearities in Metal Nanoparticles. *J. Phys. Chem. B* **2001**, *105*, 2264–2280.

(22) Bonn, M.; Funk, S.; Hess, C.; Denzler, D. N.; Stampfl, C.; Scheffler, M.; Wolf, M.; Ertl, G. Phonon- Versus Electron-Mediated Desorption and Oxidation of CO on Ru(0001). *Science.* **1999**, *285*, 1042–1045.

(23) Zhang, Y.; Yam, C.; Schatz, G. C. Fundamental Limitations to Plasmonic Hot-Carrier Solar Cells. *J. Phys. Chem. Lett.* **2016**, 1852–1858.

(24) Bosbach, J.; Hendrich, C.; Stietz, F.; Vartanyan, T.; Träger, F. Ultrafast Dephasing of Surface Plasmon Excitation in Silver Nanoparticles: Influence of Particle Size, Shape, and Chemical Surrounding. *Phys. Rev. Lett.* **2002**, *89*, 257404.

(25) Hubenthal, F.; Träger, F. Chemical Damping of the Localized Surface Plasmon Polariton Resonance: Infuence of Different Chemical Environments. In; Geohegan, D. B.; Dubowski, J. J.; Träger, F., Eds.; International Society for Optics and Photonics, 2011; p. 79220D.

(26) Wu, K.; Chen, J.; McBride, J. R.; Lian, T. Efficient Hot-Electron Transfer by a Plasmon-Induced Interfacial Charge-Transfer Transition. *Science.* **2015**, *349*, 632–635.

(27) Boerigter, C.; Campana, R.; Morabito, M.; Linic, S. Evidence and Implications of Direct Charge Excitation as the Dominant Mechanism in Plasmon-Mediated Photocatalysis. *Nat. Commun.* **2016**, *7*, 10545.

(28) Kambhampati, P.; Child, C. M.; Foster, M. C.; Campion, A. On the Chemical Mechanism of Surface Enhanced Raman Scattering: Experiment and Theory. *J. Chem. Phys.* **1998**, *108*, 5013.

(29) Osawa, M.; Matsuda, N.; Yoshii, K.; Uchida, I. Charge Transfer Resonance Raman Process in Surface-Enhanced Raman Scattering from P-Aminothiophenol Adsorbed on Silver: Herzberg-Teller Contribution. *J. Phys. Chem.* **1994**, *98*, 12702–12707.

(30) Im, S. H.; Lee, Y. T.; Wiley, B.; Xia, Y. Large-Scale Synthesis of Silver Nanocubes: The Role of HCl in Promoting Cube Perfection and Monodispersity. *Angew. Chem. Int. Ed. Engl.* **2005**, *44*, 2154–2157.

(31) Ghaedi, M.; Heidarpour, S.; Nasiri Kokhdan, S.; Sahraie, R.; Daneshfar, A.; Brazesh, B. Comparison of Silver and Palladium Nanoparticles Loaded on Activated Carbon for Efficient Removal of Methylene Blue: Kinetic and Isotherm Study of Removal Process. *Powder Technol.* **2012**, *228*, 18–25.

(32) Browne, W. R.; McGarvey, J. J. The Raman Effect and Its Application to Electronic Spectroscopies in Metal-Centered Species: Techniques and Investigations in Ground and Excited States. *Coord. Chem. Rev.* **2007**, *251*, 454–473.

(33) Hugall, J. T.; Baumberg, J. J.; Mahajan, S. Disentangling the Peak and Background Signals in Surface-Enhanced Raman Scattering. *J. Phys. Chem. C* **2012**, *116*, 6184–6190.

(34) Hugall, J. T.; Baumberg, J. J. Demonstrating Photoluminescence from Au Is Electronic Inelastic Light Scattering of a Plasmonic Metal: The Origin of SERS Backgrounds. *Nano Lett.* **2015**, *15*, 2600–2604.

(35) Langhammer, C.; Kasemo, B.; Zorić, I. Absorption and Scattering of Light by Pt, Pd, Ag, and Au Nanodisks: Absolute Cross Sections and Branching Ratios. *J. Chem. Phys.* **2007**, *126*, 194702.

(36) Chen, X.; Chen, Y.; Yan, M.; Qiu, M. Nanosecond Photothermal Effects in Plasmonic Nanostructures. *ACS Nano* **2012**, *6*, 2550–2557.

(37) Nicolai, S. H. A.; Rubim, J. C. Surface-Enhanced Resonance Raman (SERR) Spectra of Methylene Blue Adsorbed on a Silver Electrode. *Langmuir* **2003**, *19*, 4291–4294.

(38) Khurgin, J. B. How to Deal with the Loss in Plasmonics and Metamaterials. *Nat. Nanotechnol.* **2015**, *10*, 2–6.

(39) Khurgin, J. B.; Sun, G. Scaling of Losses with Size and Wavelength in Nanoplasmonics and Metamaterials. *Appl. Phys. Lett.* **2011**, *99*, 211106.

(40) Sundararaman, R.; Narang, P.; Jermyn, A. S.; Goddard III, W. A.; Atwater, H. A. Theoretical Predictions for Hot-Carrier Generation from Surface Plasmon Decay. *Nat. Commun.* **2014**, *5*, 5788.

(41) Hartland, G. V. Optical Studies of Dynamics in Noble Metal Nanostructures. *Chem. Rev.* **2011**, *111*, 3858–3887.

(42) Trolle, M. L.; Pedersen, T. G. Indirect Optical Absorption in Silicon via Thin-Film Surface Plasmon. *J. Appl. Phys.* **2012**, *112*, 043103.

(43) Abeles, F. *Optical Properties of Solids*; North-Holland Pub. Co.: Amsterdam, 1972.

(44) Brown, A. M.; Sundararaman, R.; Narang, P.; Goddard, W. A.; Atwater, H. A. Nonradiative Plasmon Decay and Hot Carrier Dynamics: Effects of Phonons, Surfaces, and Geometry. *ACS Nano* **2016**, *10*, 957–966.

(45) Warren, S. C.; Thimsen, E. Plasmonic Solar Water Splitting. *Energy Environ. Sci.* **2012**, *5*, 5133–5146.

(46) Schodek, D. L.; Ferreira, P.; Ashby, M. F. *Nanomaterials, Nanotechnologies and Design: An Introduction for Engineers and Architects*; 1st ed.; Butterworth-

Heinemann: Burlington, MA, 2009.

(47) Kale, M. J.; Avanesian, T.; Xin, H.; Yan, J.; Christopher, P. Controlling Catalytic Selectivity on Metal Nanoparticles by Direct Photoexcitation of Adsorbate-Metal Bonds. *Nano Lett.* **2014**, *14*, 5405–5412.

(48) Palmer, R. E.; Rous, P. J. Resonances in Electron Scattering by Molecules on Surfaces. *Rev. Mod. Phys.* **1992**, *64*, 383–440.

(49) Christopher, P.; Xin, H.; Linic, S. Visible-Light-Enhanced Catalytic Oxidation Reactions on Plasmonic Silver Nanostructures. *Nat. Chem.* **2011**, *3*, 467–472.

(50) Mukherjee, S.; Libisch, F.; Large, N.; Neumann, O.; Brown, L. V; Cheng, J.; Lassiter, J. B.; Carter, E. A.; Nordlander, P.; Halas, N. J. Hot Electrons Do the Impossible: Plasmon-Induced Dissociation of H_2 on Au. *Nano Lett.* **2013**, *13*, 240–247.

(51) Kale, M. J.; Avanesian, T.; Christopher, P. Direct Photocatalysis by Plasmonic Nanostructures. *ACS Catal.* **2014**, *4*, 116–128.

Chapter 6

Conclusions and Future Outlook

6.1 Summary

This dissertation set out to use a combination of novel and established experimental techniques, theoretical simulations, and quantitative analysis to shed light on the fundamentals of LSPR-induced charge transfer in plasmonic nanoparticle-adsorbate systems. Chief among the experimental tools used was Raman spectroscopy, which was shown to be able to probe the vibrational mode energy distribution of a collection of molecules on the surface of plasmonic Ag nanoparticles. In probing the energy landscape of these plasmonic systems, the anti-Stokes portion of the Raman spectrum, which is typically very weak and often ignored, proved to be crucial data in the quantitative analysis. Deviations in the (corrected) anti-Stokes to Stokes signal ratio from the predicted Boltzmann distribution in a Ag-MB plasmonic system specially designed for SERS measurements led to the discovery that under resonant conditions, it is possible to induce high rates of efficient, direct charge transfer from plasmonic nanoparticle to

adsorbate. In this chapter, the conclusions from the studies of this dissertation are summarized and the next steps for future researchers are outlined.

6.2 Conclusions

This dissertation set out to take advantage of the capabilities of surface enhanced Raman spectroscopy (SERS) to probe the vibrational energy landscape in plasmonic nanoparticle-adsorbate systems. The experiments carried out used these capabilities to develop a fundamental understanding of the mechanisms of photo-induced charge transfer in these systems. While SERS experiments formed the backbone of the studies of this dissertation, a number of other important experimental characterization techniques and theoretical simulations supplemented the results to provide a complete picture of the microscopic mechanisms of charge transfer. The major conclusions from the studies of this dissertation are discussed individually and collectively in the following subsections.

6.2.1 Corrections to anti-Stokes raw data to accurately reflect vibrational populations

Before Raman spectroscopy studies delved into the mechanisms of charge transfer, the issue of ensuring the quantitative comparison of the anti-Stokes and Stokes peak data accurately represented the vibrational population distribution within the systems measured needed to be addressed. Chapter 3 began with a look into the two causes of deviations of the measured anti-Stokes signal strength from the actual vibrational population distribution: instrumental CCD error and unequal electromagnetic SERS enhancements of Stokes and anti-Stokes photons. Using a non-SERS system (liquid toluene) and a Ag-probe molecule (R6G) system known to NOT undergo charge transfer,[1,2] a baseline anti-Stokes to Stokes ratio was established to correct for these

causes of deviation. The correction factor calculated in this chapter was used for the studies on charge transfer systems in the following chapters.

6.2.2 Evidence of direct charge transfer as the dominant mechanism

The introductory chapter of this dissertation alluded to two potential charge transfer pathways in plasmonic nanoparticle-adsorbate systems: indirect and direct. Using a Ag nanocube-MB system designed for SERS measurements, it was shown that under resonant conditions (*i.e.,* the correct wavelength of light to excite charge transfer transitions) direct charge transfer took place. Under 785 nm Raman laser illumination, the Ag-MB system showed a highly elevated anti-Stokes Raman signal compared to the Stokes signal, and this deviation was shown to be laser intensity dependent. At laser wavelengths of higher energy, the same result was not observed. Additional optical characterization of the plasmonic systems and finite-difference time-domain (FDTD) simulations of the electric field enhancements around Ag nanoparticle aggregates confirmed the only possible cause of the anti-Stokes results was an elevated population of vibrationally excited modes in MB.

The wavelength dependent nature of the occurrence of charge transfer (it only occurred at the lower energy Raman laser used) led to the conclusion that the charge transfer occurring in such cases was of the direct mechanism. In an indirect mechanism, higher energy photons (shorter wavelengths) would cause charge transfer to a greater extent. Because the 532 nm laser showed no signatures of charge transfer, it was concluded that the dominant mechanism under 785 nm illumination was direct.

6.2.3 Engineering the efficient flow of energy via direct charge transfer

With direct charge transfer established as the dominant mechanism under resonant condition in a plasmonic nanoparticle-adsorbate system, this dissertation next looked at the flow or charge and energy all the way from the photon to the adsorbate (*i.e.*, out of the plasmonic particle). To do so, methods for simultaneously measuring nanoparticle and adsorbate temperatures using Raman spectroscopy were adapted from previously published studies.[3,4] The same Ag-MB system, under the same conditions, in which direct charge transfer was observed showed that as a result of direct transfer, the energy of the photon was, upon plasmon relaxation, selectively deposited in the adsorbate and not the nanoparticle. The evidence to support this assertion was that the measured adsorbate temperatures under 785 nm illumination were hundreds of degrees above the ambient atmospheric temperature, while the nanoparticle exhibited no such heating. The important conclusion was that direct charge transfer bypasses many of the inefficient energy dissipation pathways within a plasmonic nanoparticle, instead efficiently transporting energetic charge out of the particle in attached media.

6.3 Future outlook

This dissertation showed conclusive evidence of direct charge transfer as the dominant mechanism for LSPR-enhanced photocatalytic and charge transfer processes in plasmonic systems. It further showed how direct charge transfer efficiently funneled energetic charge carriers out of plasmonic nanoparticles into attached materials, where they could potentially be used in a number of ways. While the fundamental understanding of charge transfer mechanisms in plasmonic systems is invaluable, the specific systems

studied in this dissertation have very limited use in the fields of photocatalysis, photo-electrochemistry, or photovoltaics.

Moving forward and building off of the findings presented herein will require the design of plasmonic systems that allow for the use of energetic charge carriers transferred out of a nanoparticle for more than just adsorbate heating. While it was mentioned that a large number of studies have already demonstrated photocatalytic reaction enhancements due to what is now known to be direct charge transfer,[5] the findings of this dissertation allow for the rational and predictive design of reaction systems, through plasmonic particle tuning, and illumination-photon frequency selection. The biggest potential breakthrough will be the tuning of a reaction system for direct charge transfer to alter significantly the selectivity toward desired products. A recent study on non-plasmonic Pt nanoparticles exhibited analogous results as it showed photo-induced charge transfer to bound CO altered the selectivity to CO oxidation over H_2 oxidation when both reactants were fed with oxygen.[6]

In plasmonic systems, much attention has recently been paid to the combination of Ag and Au nanoparticles with para-aminothiophenol (PATP) as a reactive adsorbate.[7–9] This particular molecule can undergo charge transfer, as evidenced by Raman studies. The charge transfer, rather than heat the adsorbate as this dissertation showed in Ag-MB, causes the coupling of adjacently adsorbed PATP molecules to form dimercaptoazobenzene (DMAB), as shown in Figure 6-1. This system provides an excellent example of using direct charge transfer to drive a photochemical transformation on a plasmonic surface. While the specific reaction, PATP coupling, is again limited in its potential applications, similar molecules or chemistries can be modeled and studied to

expand the number of chemical reactions that can take advantage of direct charge transfer.

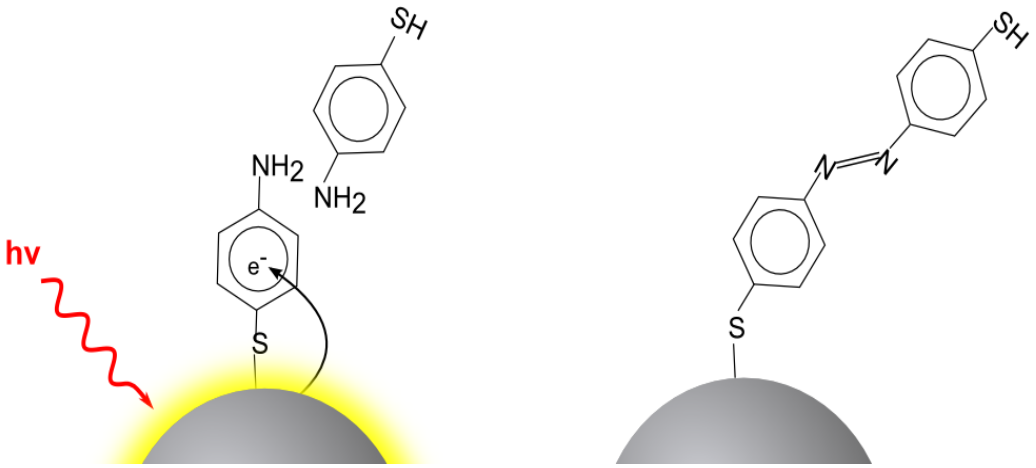

Figure 6-1: PATP coupling reaction scheme. When adsorbed to a Ag or Au nanoparticle, adjacent PATP molecules can be coupled as a result of charge transfer. The photon excited the plasmon within the particle, which causes an energetic electron injection into the molecule, providing the energy necessary to oxidize the amino group and couple two molecules.

Beyond the field of photocatalysis, the potential of harnessing LSPR-induced direct charge transfer hinges on the design of a system that couples plasmonic nanoparticles with a semiconductor acceptor of charge. In this way plasmonic particles could be used to increase efficiencies of photo-electrochemical cells such as water splitters or photovoltaic solar cells. The work in this direction will need to focus first on designing a plasmonic particle-semiconductor system that undergoes direct charge transfer at visible wavelengths. The system will also need to allow for efficient transport of energetic charge carriers away from the nanoparticle-semiconductor interface, so relaxation of the charge carriers back into the nanoparticles is prevented. While there have been some initial studies that demonstrate small enhancements in solar cell

efficiency after addition of plasmonic nanoparticles, there is still much work to be done and improvement to be made.[10–12] Engineering plasmonic nanoparticle-semiconductor interfaces for efficient charge transfer should be a very important focus of future work as the potential for solar energy conversion it presents is both vast and promising.

6.4 References

(1) Kneipp, K.; Wang, Y.; Kneipp, H.; Itzkan, I.; Dasari, R.; Feld, M. Population Pumping of Excited Vibrational States by Spontaneous Surface-Enhanced Raman Scattering. *Phys. Rev. Lett.* **1996**, *76*, 2444–2447.

(2) Haslett, T. L.; Tay, L.; Moskovits, M. Can Surface-Enhanced Raman Scattering Serve as a Channel for Strong Optical Pumping? *J. Chem. Phys.* **2000**, *113*, 1641.

(3) Hugall, J. T.; Baumberg, J. J. Demonstrating Photoluminescence from Au Is Electronic Inelastic Light Scattering of a Plasmonic Metal: The Origin of SERS Backgrounds. *Nano Lett.* **2015**, *15*, 2600–2604.

(4) Kneipp, K.; Kneipp, H.; Manoharan, R.; Itzkan, I.; Dasari, R. R.; Feld, M. S. Near-Infrared Surface-Enhanced Raman Scattering Can Detect Single Molecules and Observe “hot” Vibrational Transitions. *J. Raman Spectrosc.* **1998**, *29*, 743–747.

(5) Zhou, X.; Liu, G.; Yu, J.; Fan, W. Surface Plasmon Resonance-Mediated Photocatalysis by Noble Metal-Based Composites under Visible Light. *J. Mater. Chem.* **2012**, *22*, 21337–21354.

(6) Kale, M. J.; Avanesian, T.; Xin, H.; Yan, J.; Christopher, P. Controlling Catalytic Selectivity on Metal Nanoparticles by Direct Photoexcitation of Adsorbate-Metal Bonds. *Nano Lett.* **2014**, *14*, 5405–5412.

(7) Sun, M.; Xu, H. A Novel Application of Plasmonics: Plasmon-Driven Surface-Catalyzed Reactions. *Small* **2012**, *8*, 2777–2786.

(8) Huang, Y.-F.; Zhu, H.-P.; Liu, G.-K.; Wu, D.-Y.; Ren, B.; Tian, Z.-Q. When the Signal Is Not from the Original Molecule to Be Detected: Chemical Transformation of Para-Aminothiophenol on Ag during the SERS Measurement. *J. Am. Chem. Soc.* **2010**, *132*, 9244–9246.

(9) Joseph, V.; Engelbrekt, C.; Zhang, J.; Gernert, U.; Ulstrup, J.; Kneipp, J.

Characterizing the Kinetics of Nanoparticle-Catalyzed Reactions by Surface-Enhanced Raman Scattering. *Angew. Chem. Int. Ed. Engl.* **2012**, *51*, 7592–7596.

(10) Zhang, Y.; Yam, C.; Schatz, G. C. Fundamental Limitations to Plasmonic Hot-Carrier Solar Cells. *J. Phys. Chem. Lett.* **2016**, 1852–1858.

(11) Wang, Z.; Cao, D.; Wen, L.; Xu, R.; Obergfell, M.; Mi, Y.; Zhan, Z.; Nasori, N.; Demsar, J.; Lei, Y. Manipulation of Charge Transfer and Transport in Plasmonic-Ferroelectric Hybrids for Photoelectrochemical Applications. *Nat. Commun.* **2016**, *7*, 10348.

(12) Dodekatos, G.; Schünemann, S.; Tüysüz, H. Surface Plasmon-Assisted Solar Energy Conversion. In; Springer International Publishing, 2015; pp. 215–252.